



HAL
open science

Experimental systems developed to study water confined inside individual single-walled carbon nanotubes

Said Pashayev

► **To cite this version:**

Said Pashayev. Experimental systems developed to study water confined inside individual single-walled carbon nanotubes. Cristallography. Université de Montpellier; Academy of sciences of the Azerbaijan SSR, 2023. English. NNT : 2023UMONS027 . tel-04506491

HAL Id: tel-04506491

<https://theses.hal.science/tel-04506491>

Submitted on 15 Mar 2024

HAL is a multi-disciplinary open access archive for the deposit and dissemination of scientific research documents, whether they are published or not. The documents may come from teaching and research institutions in France or abroad, or from public or private research centers.

L'archive ouverte pluridisciplinaire **HAL**, est destinée au dépôt et à la diffusion de documents scientifiques de niveau recherche, publiés ou non, émanant des établissements d'enseignement et de recherche français ou étrangers, des laboratoires publics ou privés.

THÈSE POUR OBTENIR LE GRADE DE DOCTEUR DE L'UNIVERSITÉ DE MONTPELLIER

En Physique

École doctorale: Information, Structures et Systèmes (I2S)

Unité de recherche: Laboratoire Charles Coulomb (L2C)

Experimental systems developed to study water confined inside
individual single-walled carbon nanotubes

Présentée par Said PASHAYEV
le 4 Octobre 2023

Devant le jury composé de

Mme Pascale Launois, Directrice de Recherche, Laboratoire de Physique des Solides, CNRS-Université Paris-Saclay
M. Alessandro Siria, Directeur de Recherche, Laboratoire de Physique Statique de l'Ecole Normale Supérieure de Paris
Mme Sylvie Contreras, Chargée de Recherche-HDR, Laboratoire Charles Coulomb, CNRS-Université de Montpellier
M. Benoit Charlot, Directeur de Recherche, Institut d'Electronique et des Systèmes, Université de Montpellier
M. Rasim Jabbarov, Professeur, Institut de Physique, Académie Nationale des Sciences d'Azerbaïdjan
M. Zakir Jahangirli, Professeur, Institut de Physique, Académie Nationale des Sciences d'Azerbaïdjan

Rapporteuse
Rapporteur
Examinatrice
Président du jury
Co-directeur
Examineur

Invités

M. Francois Henn, Professeur, Laboratoire Charles Coulomb, CNRS-Université de Montpellier
M. Adrien Noury, Chargé de Recherche, Laboratoire Charles Coulomb, CNRS-Université de Montpellier

Co-directeur
Encadrant



UNIVERSITÉ
DE MONTPELLIER

Contents

Contents	i
List of Figures	v
List of Tables	vii
List of Abbreviations	viii
Acknowledgment	x
1 Introduction	1
I State of the Art	5
2 Water confinement at the nanoscale	7
2.1 Introduction	7
2.1.1 Description of water	7
2.1.1.1 Hydrogen bond network	8
2.1.1.2 Dipole moment	9
2.1.1.3 Water anomalous behavior	9
2.1.2 Uniqueness of water	9
2.2 Effect of confinement at the nanoscale	10
2.2.1 From continuum to non-continuum description	10
2.2.2 Boundary conditions and slip length	11
2.2.2.1 Boundary conditions	11
2.2.2.2 Slip length	11
2.2.3 Dielectric constant	12
2.2.4 Energy and entropy issues	12
2.3 A few examples of water confinement at the nanoscale	13
2.3.1 Natural systems	13
2.3.1.1 Aquaporins (AQPs)	14
2.3.1.2 Clay minerals	15
2.3.1.3 Active charcoal	15
2.3.2 Artificial/synthetic systems	16

2.3.2.1	Zeolites	16
2.3.2.2	Metal organic frameworks	16
2.3.2.3	Boron nitride and Carbon nanotubes (NT)	16
2.4	Water confined in carbon nanotubes (CNT)	18
2.4.1	Theoretical studies	18
2.4.1.1	Structure of confined water	18
2.4.1.2	Phase diagram of confined water in CNTs	19
2.4.1.3	Dynamics and Molecular transport	20
2.4.2	Experimental works	21
2.4.2.1	Structure	21
2.4.2.2	Phase diagram	21
2.4.2.3	Mass transport in CNT membranes	22
2.4.2.4	Mass transport in individual NTs	22
2.5	Conclusion	23
3	Manufacturing of a sealed Micro/ Nanofluidic device	25
3.1	Direct wafer bonding	25
3.1.1	Fusion bonding	26
3.1.2	Anodic bonding	26
3.2	Indirect wafer bonding	28
3.2.1	Polydimethylsiloxane (PDMS)	28
3.2.1.1	Processing of PDMS	29
3.2.1.2	Pressure tightness, long-term stability of PDMS	30
3.2.1.3	Drawbacks of PDMS	31
3.2.2	SU-8	33
3.2.2.1	SU-8 for microfluidic devices	34
3.2.2.2	Properties of SU-8 devices	35
3.2.2.3	Limitation of SU-8	36
3.2.3	Other adhesives: PS, PC, PMMA, and NOA	36
3.2.4	Device testing methods	38
3.2.4.1	Tensile strength	39
3.2.4.2	Burst pressure	39
3.2.4.3	Liquid leakage	40
3.2.4.4	Gas leakage	40
3.3	Conclusion	41
4	CNT, CNTFET, and interaction with water	43
4.1	CNT synthesis and giving features	43
4.1.1	CNT structure	43
4.1.2	Synthesis, impurity, and purification of CNTs	45
4.1.3	CNTs properties	48
4.1.3.1	Mechanical and Thermal properties	48
4.1.3.2	Electrical and optical properties	48
4.2	Manufacturing of a CNTFET	50
4.2.1	CNTFET fundamentals	50
4.2.1.1	Principle of FETs structure	50
4.2.1.2	Electrical response of the CNTFET	50
4.2.1.3	Charge traps, Silanol groups, and Schottky barrier	55
4.3	State of the Art about CNTFET behavior in interaction with water	57

4.3.1	Possible mechanisms behind water effect on the CNTFET	57
4.3.2	The effect of liquid or vapor water at the external surface of CNT . . .	58
4.3.3	The effect of confined water	60
4.4	Conclusion	60
II Experimental work		61
5	SU-8 based high liquid water pressure tight, vacuum compatible, long-term stable sealing technology	63
5.1	Device fabrication/ assembling	64
5.1.1	Cleanroom fabrication	64
5.1.2	Device assembling	66
5.2	Liquid water pressure tightness test	67
5.2.1	Measurement set-up	67
5.2.2	Burst pressure tightness & dependence on device thickness	69
5.3	SU-8 porosity test using conductivity measurement	69
5.3.1	Measurement set-up	69
5.3.2	Conductivity: salt concentration & thickness dependence	70
5.3.3	Comparison with PDMS	72
5.3.4	Ageing: time evolution of the conductivity	72
5.4	Vacuum test	73
5.4.1	Measurement set-up	73
5.4.2	Measurement of the leak rate	73
5.5	Conclusion	74
6	Electronic response of CNTFET upon water adsorption	75
6.1	CNTFET device fabrication and characterization methodology	75
6.1.1	CVD: CNT growth (focus on individual SWCNT)	75
6.1.1.1	Optical mark etching	75
6.1.1.2	Catalyst deposition	76
6.1.1.3	CVD growth	77
6.1.2	SEM: selecting CNT	78
6.1.2.1	Raman: Diameter distribution of CNTs in the catalyst pattern	78
6.1.3	Clean room fabrication	79
6.1.3.1	Metal contacts deposition and lift-off	79
6.1.3.2	AFM: estimation of the nanotube diameter	80
6.1.4	Measurement set-ups	80
6.1.4.1	Electrical measurement set-ups of CNTFET performance	80
6.1.5	About the two type of measurements	81
6.1.5.1	CNT resistance in air & length dependence	83
6.1.6	CNT opening and individual SWCNT characterization	85
6.1.6.1	Distinguishing individual SWCNT from MWCNT and bundles	85
6.1.6.2	Current annealing	86
6.1.6.3	Effect of experimental electrical parameters on the transfer curve	86
6.2	Impact of liquid drop on CNTFET electronic response	89
6.2.1	Case of "pure" water	89
6.2.2	Case of other liquids: effect of the dielectric constant or charge traps	90
6.3	Impact of water partial pressure and current annealing	91

6.3.1	Case of close and open SWCNT in air	92
6.3.2	After evaporation of a liquid water drop	94
6.3.3	Comparision of different CNT metallicities	94
6.3.4	Case of Bundle or MWCNT	95
6.4	Desorption of water under vacuum	96
6.4.1	The effect of pressure	96
6.5	Conclusion	98
7	Prospectives and General conclusion	101
A	CNTFET device fabrication protocols	105
A.1	CNTFET sample fabrication	105
B	Small diameter CNTs synthesis via CVD	109
B.1	Sample fabrication	109
B.2	Characterization of as-grown nanotubes	111
B.3	Results	114
B.3.1	The impact of different catalysts compositions	114
B.3.2	The impact of iron concentration on CNT synthesis	115
B.3.3	The impact of ruthenium concentration on CNT synthesis	116
B.3.4	The impact of the concentration ratio of Fe to Ru on the CNT synthesis	117
B.3.5	Flow NF or HF	117
B.3.6	The impact of moisture volume concentration in the furnace on the CNTs synthesis	118
B.4	Conclusion	118
	Bibliography	120
	Résumé	142
	Summary	143

List of Figures

2.1	Tetrahedral arrangement of water molecule	8
2.2	Length scales for nanofluidics	10
2.3	Different slip lengths	12
2.4	AQPs structure and selective water flow	14
2.5	Slip length of water confined in an individual CNT and BNNT	17
2.6	Structure of water confined inside CNT	19
2.7	Phase diagram of water confined in SWCNTs	19
3.1	Schematic of the fusion bonding	26
3.2	Schematic of the anodic bonding	27
3.3	Molecular structure of PDMS	29
3.4	Drawbacks of PDMS	31
3.5	Molecular structure of SU-8	33
4.1	Different types of CNTs based on their chirality	44
4.2	CNT indices on hexagonal graphene lattice	44
4.3	CNT synthesis methods	46
4.4	Band structure of the CNT	49
4.5	Schematic of FET	50
4.6	CNTFET designs	52
4.7	Drain current versus gate voltage of SWCNT	53
4.8	Gate hysteresis in sc-SWCNT	53
4.9	Type of charge traps	55
4.10	Hystheretic surface charging involving silanol groups	56
4.11	CNTFET sensing mechanisms	57
5.1	Schematic presentation of the SU-8 photolithography process	64
5.2	Photoresist homogeneity	65
5.3	SU-8 assembling tools	66
5.4	SU-8 bonding observation	67
5.5	SU-8 assembling challenges	67
5.6	Liquid water pressure leak-tightness measurement setup	68
5.7	Optical observation SU-8 wall liquid water pressure leak tightness	68
5.8	Liquid water burst pressure leak tightness	69
5.9	Schematic of the two reservoirs sample	70

5.10	Ionic conductivity measurement of SU-8 wall	71
5.11	Schematic of the vacuum setup for SU-8 porosity measurement	73
6.1	Scheme of CNTFET fabrication	76
6.2	Microscopy observation of optical marks and catalyst patterns	77
6.3	SEM observation of as-grown CNTs	78
6.4	Diameter distribution of the CNTs in the catalyst pattern measured with Raman spectroscopy	79
6.5	SEM observation of sample after lift-off process	79
6.6	CNT diameter estimation with AFM	80
6.7	Measurement set-up	81
6.8	Schematic of the different measurement types	81
6.9	Gate leak baseline for different set-ups	82
6.10	Water electrolysis voltage	82
6.11	I_{SD} & V_{SD} curves for 5 μm CNT sections on the same CNT	83
6.12	CNT electrical performance channel length dependence	84
6.13	First assumption to calculate CNT resistance	84
6.14	Second assumption to calculate CNT resistance	85
6.15	Selecting CNT from breakdown current	86
6.16	The impact of first current annealing on CNT conductance curve	87
6.17	The effect of electrical experimental parameters	88
6.18	Conductance curves of different type of CNTs	88
6.19	Liquid water impact on the conductance curve of the CNTFET	89
6.20	The impact of liquids with different dielectric constants	90
6.21	Main metrics in conductance curve of the CNT in water & CNT interaction	91
6.22	Comparison of air partial pressure effect on the close and open individual SWCNT	93
6.23	After water drop evaporated	94
6.24	Impact of the CNT metallicity on the evolution of V_g^+ as a function of the hydrated state	95
6.25	Comparison of bundle or MWCNT as close and open cases	96
6.26	Water desorption as a function of the level of vacuum	97
6.27	The schematic of measuring water desorption	97
6.28	Scheme of different types of water forming	99
6.29	The schematic of water adsorption/desorption process	100
B.1	SEM image of the CNTs grown on the substrate	111
B.2	Diameter approximation of CNT grown from catalyst pattern	112
B.3	Kataura plot	112
B.4	Raman spectra of CNTs	114
B.5	The diameter distribution of the CNTs	115
B.6	The effect of iron concentration on the CNT synthesis	116
B.7	The impact of the Ru on the diameter distribution of the CNTs	116
B.8	The impact of Fe to Ru concentration ratio on the CNT synthesis	117

List of Tables

3.1	PDMS permeability	32
4.1	Parameters of carbon nanotubes	44
4.2	CNTs synthesis methods and their efficiency	47
5.1	Comparison of ionic conductivity of SU-8 and PDMS	72
B.1	Raman spectroscopy parameters for each laser type	113
B.2	The list of samples used for CVD optimization to get small diameter CNTs . .	119

List of Abbreviations

AFM	Atomic Force Microscopy
AQPs	Aquaporins
BNNT	Boron Nitride Nanotube
CNT	Carbon Nanotube
CNTFET	Carbon Nanotube Field Effect Transistor
CTE	Coefficient Thermal Expansion
CVD	Chemical Vapor Deposition
DCNA	Double Cross-Linked Adhesives
DI	Deionized
DMA	Dynamic Mechanical Analysis
DMPMS	Dimethyl-Methylphenylmethoxy Siloxane
DOS	Density of State
DWCNT	Double Walled Carbon Nanotube
FET	Field Effect Transistor
GBL	Gamma-Butyrolactone
GS-MS	Gas Chromatography-Mass Spectrometer
HB	Hydrogen Bond
ICP	Inductive Coupled Plasma
IPA	Isopropanol
IR	Infrared
JFET	Junction Field Effect Transistor
MEMS	Micro-Electromechanical Systems
MOF	Metal Organic Framework
MOSFET	Metal Oxide Semiconductor Field Effect Transistor
MPS	Mercaptopropyl Silane
MS	Mass Spectrometry
MSD	Molecular Dynamic Simulation
m-SWCNT	Metallic Single-Walled Carbon Nanotube
MWCNT	Multi Walled Carbon Nanotube
NEMS	Nano-Electromechanical Systems
NMR	Nuclear Magnetic Resonance

NOA Norland Optical Adhesive
PC Polycarbonate
PDMS Polydimethylsiloxane
PEN Polyethylene Naphtalate
PET Polyethylene Terephthalate
PGMEA Propylene Glycol Methyl Ether Acetate
PI Polyimide
PMMA Poly(Methyl Methacrylate)
PS Polystyrene
PSA Pressure Sensitive Adhesive
RBM Radial Breathing Mode
SB Schottky Barrier
SB-CNTFET Schottky Barrier Carbon Nanotube Field Effect Transistor
sc-SWCNT Semiconducting Single-Walled Carbon Nanotube
SEM Scanning Electron Microscopy
SWBNNT Single-Walled Boron Nitride Nanotube
SWCNT Single-Walled Carbon Nanotube
TPE Thermoplastic Elastomers
UHV Ultra-High Vacuum
UV Ultraviolet
VHS Van Hove Singularity

Acknowledgment

I would like to express my deepest gratitude to the remarkable individuals who have made this thesis possible. Their constant support, guidance, and encouragement have been instrumental in shaping this academic journey.

First and foremost, I want to express my appreciation to my esteemed thesis co-supervisors. Francois Henn, despite his incredibly busy schedule, consistently found time to discuss the research results and determine the next steps. Rasim Jabbarov's unstoppable motivation and inspiration have been the driving force behind this endeavor. Words cannot express my gratitude to my thesis encadrant, Adrien Noury, for his patience, insightful scientific discussions, and generous sharing of knowledge and practical expertise. I am profoundly grateful to them for their encouragement, insights, patience, and unwavering commitment to academic excellence. Their outstanding mentorship provided the strong foundation upon which this research stands.

I am also extremely grateful to the thesis reviewers, Alessandro Siria and Pascale Launois, for their meticulous review of the manuscript and the invaluable comments and suggestions they provided. Their expert insights, constructive criticisms, and valuable recommendations have significantly enhanced the quality of this thesis.

I extend my gratitude to the esteemed jury members of the defense. Benoit Charlot, Sylvie Contreras, and Zakir Jahangirli for their rigorous examination and constructive insights were pivotal in completing this endeavor.

My research was conducted in the Laboratory Charles Coulomb within the NMAT team. I wish to express my gratitude to all laboratory and team members who contributed to this work either directly or indirectly. Special thanks go to Vincent Jourdain and Said Tahir, who were always supportive and willing to discuss. I want to express my appreciation to those I had the privilege to work with during this journey, including Romain Lhermerout, David Maurin, Remi Jelinek, Eric Anglaret, Eric Alibert, Renaud Metz, Nicolas Izard, Laurent Alvarez, Christophe Blanc, Raymond Aznar, Lucyna Firlej, Jerome Barbat, Guillaume Prevot, Jean Christophe Art, and many others. Sincere thanks also go to my fellow PhDs and post-docs in the team, such as Nam, Gustavo, Clarisse, Rudy, Eira, Vladimir, Clement, Saddam, Abdullah, Imane, Domitille, and Valerii.

The time I spent in the clean room was productive and enlightening thanks to the dedication and expertise of engineers Frederic Pichot, Christophe Roblin, Jean-Marie Peiris, and Renaud Felix, who patiently trained me in various device fabrication and characterization tools. Their meticulousness and collaborative spirit ensured that every experiment was conducted with precision.

I would like to extend my sincere gratitude to the friends I have met throughout this journey. Their encouragement and friendship make this academic endeavor personally enjoyable. To friends from my homeland, their presence has been a comforting reminder of home, and our shared moments have brought solace in the middle of academic challenges. To friends from all over the world, their diverse perspectives have broadened my horizons, and our cultural

exchanges have been an inspiration. While I will not identify them all individually, their influence and friendship have left an indelible mark on this chapter of my life.

Lastly, to my family, words cannot express the depth of my gratitude. Their unwavering faith in my capabilities and their endless love and support have been the pillars that sustained me throughout this rigorous academic journey.

In conclusion, I recognize that this doctorate is not uniquely the product of my efforts but an indication of the collective support, belief, and hard work of all those mentioned and many more.

Although water is the most widely distributed liquid on earth, and the most directly involved in a wide range of phenomena, whether natural (e.g. biological, geological, climatological) or artificial (e.g. hydropower, turbines, synthesis of chemicals and materials, hygiene, etc.), contemporary science has yet to explain all its physicochemical characteristics. It has to be said that it has unique properties: the density of its solid forms is lower than that of its liquid state, it has numerous crystallized and amorphous solid phases, it has a very high dielectric constant, it can solvate large quantities of salts and liquids, including those that are not very polar, and it is highly absorbent in several frequency ranges (mainly microwaves, infrared (IR), and ultraviolet (UV)). Water is therefore still the subject of deep fundamental studies. As Philipp Ball wrote in 2000 in the introduction to his book "H₂O: a biography of Water" (ed. Weidenfeld & Nicolson): *"the extent to which water remains a scientific mystery is extraordinary, despite its prevalence and central importance on Earth. Whether one considers its role in biology, its place in the physical world (where it refuses to obey the usual rules of liquids), or its deceptively simple structure, there is still no complete answer to the question: what is water?"*. And since then, much has been discovered about water. These include the announcement in 2016 of the existence of a second liquid phase[1] and in 2017 of a second critical point in its supercooled state[2].

To all the remaining "mysteries" of bulk water, we must add all those that will be discovered when water is no longer studied and used as a material made up of billions of molecules occupying a three-dimensional volume as little as a few nanolitres, but when it is confined in spaces where at least one dimension is about one nanometer. Numerous studies have already been carried out under such conditions, and it has soon become apparent that water confined on the nanoscopic scale could exhibit properties that do not correspond to those explicable by the equations of continuum physics[3].

This calls for new representations in which it becomes necessary to consider physics at molecular scales, i.e. the physics of matter made up of discrete entities, where interactions with the wall of the "nano-container" and its geometry turn out to be factors that predom-

inantly influence physicochemical properties. As an example, it is well known that, under atmospheric pressure, the solid-solid or solid-liquid transitions of water confined in nanometric porosities can be higher or lower than that of bulk water[4, 5, 6].

Understanding these new properties is essential not only for reasons of fundamental physics, but also for practical reasons: in many natural or artificial systems, water is confined in nanometric spaces, and its characteristics and properties are therefore modified, particularly those relating to the spatial organization and dynamics of its molecules. These two particular issues play a major role in water's ability to flow, transporting with it or not the molecules or ions it has solvated.

We are referring here to a relatively recent field of fundamental research known as nanofluidics [7], whose applications include the study of the transport of water and aqueous electrolytes through i) biological transmembrane channels such as aquaporins or ion channels (to understand the origin of cellular dysfunction and then propose therapeutic solutions)[8], ii) artificial nanoporous membranes developed for nanofiltration (to desalinate seawater or produce so-called blue energy)[9, 10] or iii) natural or non-natural nanoporous materials such as clays, zeolites or silicas (to absorb and retain radioactive waste, for instance).

It is, therefore, straightforward to understand why, for both fundamental and applied issues, water nanofluidic is a subject of great interest. Today, constant progress being made in the fields of nanotechnology and experimental nanoscience, alongside those in theoretical studies based on new analytical models or numerical calculations, is opening up more and more opportunities to investigate water at the nanoscale and hence to deepen our knowledge, to discover new physicochemical properties as well as to broaden or improve the practical usages/applications. It has to be said, however, that the experimental difficulties encountered when trying to study the behavior of single nanometric objects mean that more theoretical than experimental work has been so far reported in the literature. A vast field of experimental studies, therefore, remains largely to be explored and are requested to support or not the outcomes of theoretical work. Permanent cyclic feedback between experimental and theoretical data is more than necessary.

The project of my Ph.D. is fully in line with the research focus on water nanofluidics and aims to address a number of experimental challenges, in particular, that of i) isolating and manipulating a single "nano-container" in which water can be confined, ii) controlling the environment in which it is located, and finally, iii) developing reliable physical measurements to characterize both the behavior of the confined water molecules and on the other hand the impact of the confined water molecules on the physicochemical properties of the "nano-container". Once these terms are established, we still need to define the object of study, i.e. the porous nanostructure capable of confining water, and to build the experimental models we intend to use to achieve our stated objectives, i.e. to understand the organization of water molecules and their dynamics once they are confined in the nano-container. However, it must be kept in mind that at the scale of a single porous nanoscopic object, it is difficult to obtain direct information on how the matter confined within it behaves. In other words, it is hard to see exactly what is going on inside. One of the ways to date is to study the effects induced by the presence of the confined matter on the nanoobject's properties.

In order to access the required information with the minimum of hindrance and difficulty, the nanostructure we wish to study must above all be the one whose geometrical characteristics are well-defined and quite simple, and whose physicochemical properties are as well-known as possible. Also, it must be the one we could most easily dispose of and manipulate. The team in which this thesis was carried out has recognized expertise in the synthesis of single-walled carbon nanotubes (SWCNT) isolated on Si or SiO₂ substrate by means of Chemical Vapor Deposition (CVD). It has also developed several protocols for transferring this type of nanotube into μ -devices, which can be considered as Lab-on-Chip. Furthermore, it has already optimized several optical, electrical, and mechanical measurement platforms adapted to CNT characterization. For all these reasons, and many others linked to their unique properties, SWCNTs naturally appeared to be the nanostructure of choice for our study.

In order to meet our objectives, we thus decided to:

- i) develop a protocol specifically designed to impose a controlled environment of liquid water or partial water pressure on a sealed μ -device that could be used in different types of measurement platforms/Lab-on-Chip and,
- ii) use electrical measurements to study the behavior of a field-effect μ -transistor (FET), whose channel is an open or closed SWCNT, subjected to several possible environments: ambient air, different vacuum levels at ambient or elevated temperatures, different partial pressures of water and liquid water.

The manuscript is divided into two main parts as follows. The first part concerns the state of the art. It is made of three chapters that deal with "Water confinement at the nanoscale", "Manufacturing of a sealed Micro/ Nanofluidic device", and "CNT, CNTFET, and its interaction with water", respectively.

The second part reports the most representative results obtained in our studies. First, in chapter 5, we present the performance of the μ -devices designed and built to validate a protocol for manufacturing sealed μ -nanofluidic devices with which experiments can be carried out under a controlled atmosphere. Then in chapter 6, we account for the data obtained on our CNTFET subjected to various environments or thermal treatments. Enormous diversity can be observed for as-grown CNTs such as the number of walls, bundles, and metallicity, thus we showed that it is essential to identify CNT properly in order to interpret data.

This manuscript ends with a general conclusion and a presentation of the prospects opened up by our work. To keep the text as easily readable as possible, we have chosen to describe in detail the methods used throughout our research in the appendixes at the end of the document. This includes "CNTFET device fabrication protocols" and "Small diameter CNTs synthesis via CVD".

Part I

State of the Art

Water confinement at the nanoscale

The term “nanoscale confinement” describes the confinement of substances, such as gases, liquids, or solids in a space with at least one dimension on the order of nanometer. Confinement at this scale may result in special physicochemical properties different from those of bulk matter .

Water is the main solvent of living organisms and also the main solvent in geology and materials science. When water is confined in the nanoscale it displays non-continuum behavior, leading to changes in both its structural and transport characteristics. The latter refers to the field of "nanofluidics" which has recently gained popularity, because of its application in numerous areas, covering biology, physics, chemistry, and electronics. In this chapter, properties of the bulk and nanoscale confined water are presented, as well as nanoscale confinement systems, and the literature review related to studies about static and dynamic properties of confined water in Carbon nanotubes (CNTs).

2.1 Introduction

Water presents a number of so-called anomalous properties. These anomalous properties are mainly due to the peculiar arrangement of the water molecules, owing to the presence of hydrogen bonds and a large dipole moment in and between molecules.

2.1.1 Description of water

Water is the most abundant substance on Earth. It covers 75% of the Earth’s surface and 65% of our body is made up of water. Therefore, the presence of water is closely entangled with the presence of life. Bulk water exists in all three physical states, such as solid (ice), liquid (water), and gas (vapor). It also exists under the supercritical "state" for $T > 374\text{ °C}$ and $P > 22\text{ MPa}$ that is only possible on Earth under particular geological conditions (nb: When confined at the nanoscale, it could also exist under other T and P conditions).

97% of the surface water is saline, while only 3% is fresh water. Over two-thirds of the

freshwater exists in the form of glaciers or ice caps. However, most of the rest of freshwater which is unfrozen is located in groundwater, above ground, or in the air .

A water molecule consists of two hydrogen atoms attached to a single oxygen atom by any-covalent bonds. It is a polar molecule (meaning that there is an uneven distribution of electron density) because the oxygen atom has a higher electronegativity than a hydrogen atom. Consequently, the oxygen atom is partially negatively charged, while hydrogen atoms are slightly positive (Figure 2.1). To form the water molecule, an electron of the hydrogen atom and electrons from oxygen atoms pair up into four orbitals (2σ O — H bonds with 2 free pairs). In the gas phase the O — H length of 0.96 \AA , and the H — O — H angle is 104.5° [11]. These parameters could be modified under confinement.

2.1.1.1 Hydrogen bond network

Intermolecular hydrogen bonds (HB) are formed between the positively charged hydrogen atoms of one water molecule with the negatively charged oxygen atoms of nearby water molecules. HB governs the structural and physical characteristics of the condensed phases of water. When compared to other liquids, water has several peculiar features[12] for which the hydrogen bond is mostly responsible as we will explain later on in the dedicated section. When the three O — H \cdots O are 109.47° and the distance to the oxygen atom of the nearby water molecule is 0.282 nm , the HB energy is the strongest (Figure 2.1). Each water molecule in condensed phases has the ability to create four HB with nearby water molecules. These four HB ideally organize themselves in tetrahedral around each water molecule (Figure 2.1). If well organized over a long distance, this tetrahedral "brick" can form many different crystalline structures. Solid state water can also be amorphous[12].

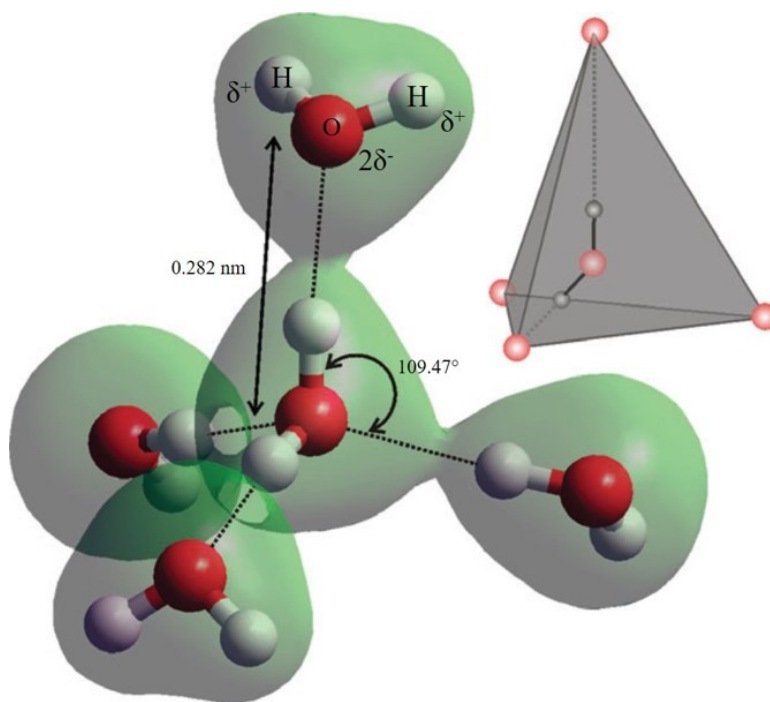


Figure 2.1: Water molecule with the schematic distribution of electrons and hydrogen bonding in the condensed phase of the water (From [13])

2.1.1.2 Dipole moment

Due to the important difference in electronegativity between O and H water molecule's dipole moment (μ) is particularly high. The dipole moment is calculated as $\mu = qr$, here q is the difference of charge, and r is the distance between the atoms. The units of the dipole moment are usually given in Debye ($D = 3.336 \times 10^{-30}$ Cm). Water's electrical dipole moment transitions from gaseous to the liquid state were examined[14]. It was observed experimentally that the dipole moment of the condensed phase is greater than the isolated water molecule due to environmental polarization and the effect of re-orientation[15]. The dipole moment for an isolated water molecule is 1.855 D, whereas it increases to 2.4 D - 2.6 D for the condensed phase, according to both practical[15] and theoretical[14] observation. Several peculiar characteristics of water, like its capacity to form hydrogen bonds and its high dielectric constant, are due to its large dipole moment. It is a crucial characteristic that affects a variety of physical and chemical properties, such as its density, melting and boiling points, the capacity to solubilize even weakly polar molecules, and its reactivity with other molecules.

2.1.1.3 Water anomalous behavior

Water possesses a number of anomalous characteristics that make it unique compared to other liquids. These anomalous qualities are mainly due to HB. For instance, ice floats because hydrogen bonds keep water molecules further apart in a solid than in a liquid, where there are statistically fewer hydrogen bonds between each molecule. The unique physical characteristics of water, such as its high heat of vaporization, high specific heat capacity, and almost universal solvent qualities, are also a result of HB and polarity. As water has a high specific heat capacity, it can absorb and retain a lot of heat. Its high heat of vaporization means that converting liquid water into water vapor requires a significant amount of energy ($\Delta_{vap}h^0 \sim 44 \text{ kJmol}^{-1}$). Due to its high surface tension, it can stick together in drops and form a meniscus inside a small tube. The ability of water to pass through small channels by capillarity depends on this feature. Due to its high dielectric constant and small molecular size, water is a very efficient solvent, especially for polar and ionic compounds. One of the other anomalous properties of water is that despite its low molecular weight water has a high boiling temperature. This high melting and boiling temperature are caused by the fact that breaking of HB network requires a significant amount of energy. That is directly related to the value of the $\Delta_{vap}h^0$. A further distinctive characteristic of water brought about by hydrogen bonds is its non-miscibility with carbon and hydrogen apolar compounds. This feature plays a crucial role in the structure of living cell membranes.

2.1.2 Uniqueness of water

The ubiquitous characteristics of bulk and confined water have numerous applications in a wide range of fields. When confined in nanocavities, i.e. pores, tubes, slits, water can exhibit physical properties significantly different than those of bulk water and thus be of great interest.

Whether confined at the nanoscale or not, water is used in desalination processes using reverse osmosis, electrodialysis, and capacitive deionization principles[16]. It can also be

used for energy storage applications in batteries and supercapacitors[9, 10] as well as to encapsulate drugs in nano vectors such as carbon- or silica-based nanostructures[17, 18].

2.2 Effect of confinement at the nanoscale

The presence of water molecules inside a nano-volume cavity is referred to as the nanoscale confinement of water. Because of the interactions between water molecules and the surface of its "nano-container" can exhibit distinct properties and behavior when compared to bulk water. Water molecules in nanoporous materials can, for example, experience a change in the number of HB networks and structures resulting in an altered diffusion coefficient and in the vanishing of its dielectric constant, diffusion coefficient, and its ability to solvate ion. These properties can make nanoscale water confinement useful for a variety of applications such as water purification, desalination, and energy conversion. Controlling the interactions between water molecules and the confining materials (hydrophilic or hydrophobic) is one of the challenges to controlling the properties of water confined at the nanoscale.

2.2.1 From continuum to non-continuum description

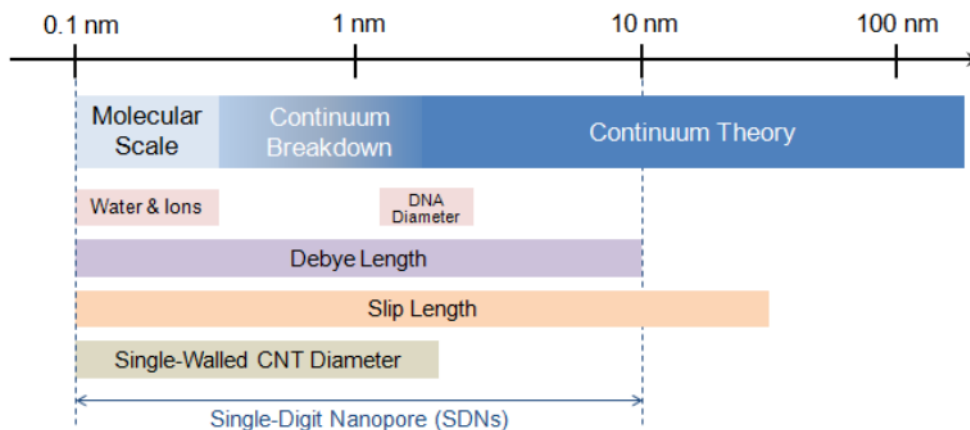


Figure 2.2: Length scales for nanofluidics (From [19])

It is basically considered that, in cavities whose dimensions exceed 1 nm, water can be treated as a continuum medium, whose properties such as density, viscosity, and pressure[20] can be understood based on "macroscopic" physics. This approach is often utilized in fluid mechanics and engineering to simulate the behavior of water in large systems. However, at smaller length scales the continuum assumption breaks down, and water has to be described by non-continuous methods[19, 7, 3] (Figure 2.2). In such cavity dimensions which are comparable to that of the molecules, the flow velocity of water does not obey the Navier-Stokes or Hagen-Poiseuille equation, since these equations do not explicitly involve the interaction with the cavity surface and the corresponding slip condition. For instance, one of the reasons that explain the conventional hydrodynamics breaks down in the smallest carbon nanotube (CNT) pores, i.e. with diameters less than about 1 nm in diameter, is that these pore sizes constrain the water molecules into a single file, drastically changing the HB pattern compared to the structure of bulk water[21]. The non-continuous description of water

is important for understanding the behavior of water in environments such as nano-porous materials and transmembrane ionic channels of biological cells.

2.2.2 Boundary conditions and slip length

2.2.2.1 Boundary conditions

Boundary conditions for the confinement of water refer to the conditions that must be met at the interface between the confined water and the cavity surface. These conditions can be different for various types of surface and also depends on the specific geometry of the cavity. For instance, “No Slip Boundary Condition” assumes that the velocity of the water at the interface of the solid wall is zero[22]. On the contrary, the “Perfect Slip Boundary Condition” assumes that the velocity of water at the surface is equal to the velocity of the water molecules far from the wall, i.e. the water molecules move without friction[23]. “Hydrophobic Boundary Condition” accounts for the effect of repelling, which tends to arrange water molecules near the surface. This can lead to a decrease in the water density near the surface and also affect its transport properties[24]. “Hydrophilic Boundary Condition” considers the effect of hydrophilic surfaces, which tends to attract water molecules at the surface and to structure HB network. This can lead to an increase in the near-surface water density and affect its transport properties[24].

Sender et al. studied the properties of water on hydrophobic and hydrophilic surfaces, focusing on the slip behavior of the molecules in the vicinity of surfaces. The authors used molecular dynamics simulations to study the behavior of water molecules in contact with two different materials: a hydrophobic graphite surface and a hydrophilic silica surface. It was observed that the water molecules on the hydrophilic surface form an ordered layer with reduced mobility and increased density compared to bulk water. The ordered layer is separated from the bulk water by an interfacial region where water molecules exhibit slip behavior, meaning that they have a reduced viscosity and can move more easily than in the bulk water[24]. It was also noted that the slip behavior near the hydrophobic surface results in reduced friction and improved fluid flow, which could have significant implications for micro- and nanofluidic applications. In conclusion, a better description of the boundary conditions yields a more accurate prediction of the behavior of confined water.

2.2.2.2 Slip length

Nanoscale confined fluid transport is characterized by a slip length. This length accounts for the behavior of the liquid near the surface. It can be represented as the depth penetrating (Figure 2.3b) the solid surface of the channel at which the velocity of the fluid is zero. The slip length is calculated as $b = \mu / \lambda$, here, λ is the friction coefficient, μ is the fluid viscosity. Compared to the no-slip boundary condition where the velocity of the fluid at the surface is zero with respect to the surface, the slip length reflects that the velocity at the surface is non-zero (Figure 2.3). An infinite slip length corresponds to the case of the frictionless surface where b is much larger than the dimension of the channel. This case corresponds to perfect slip limit conditions.

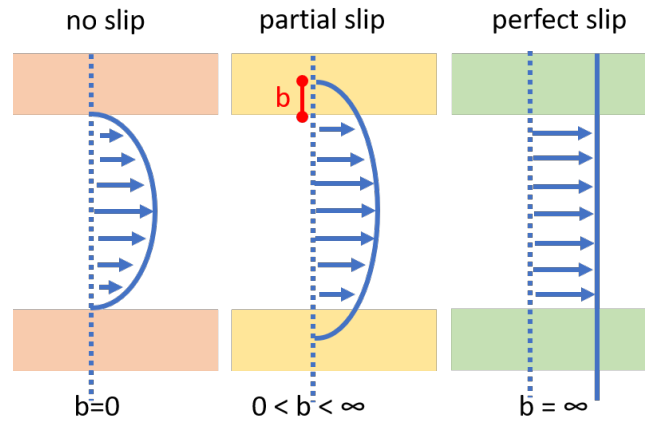


Figure 2.3: Different slip conditions with their corresponding slip lengths (From [19])

2.2.3 Dielectric constant

The dielectric constant also called the relative permittivity of the material, is defined as the product between the permittivity of the medium and the permittivity of the vacuum (i.e. the ability of a material to store electrostatic energy). For liquid bulk water, the dielectric constant is high, i.e. 78 at room temperature, and is correlated to the number of hydrogen bonds[25]. Although water is a polar molecule with a rather well-fixed dipole moment, its network of hydrogen bonds tends to counterbalance the intra-molecular dipole. As a consequence, the water dielectric constant depends on the number of HB per water molecule and the structure of the network.

Therefore, the dielectric constant of confined water was predicted to be lower than that of bulk water since the rotational freedom of the water dipole is expected to decrease near surfaces. The dielectric constant of water confined between flat hydrophobic walls with various distances up to 1 nm has been studied experimentally. The confinement of water exhibits a layered structure near surfaces and formed an ordered phase under ambient conditions. Such order is expected to show low polarizability due to the surface-induced alignment of water molecular dipoles, which are then difficult to realign by applying an electric field[26, 27]. The out-of-plane dielectric constant of this water was then calculated to be only 2.

Subsequently, Olivier et al. studied the water confined between graphene layers to explain the decrease in the dielectric constant of water using molecular dynamic simulation (MSD). They showed that the reduction in permittivity is not due to the interfacial alignment of water molecules, but rather to a long-range anisotropic dipole correlation combined with an excluded volume effect from low-dielectric confinement materials[28].

2.2.4 Energy and entropy issues

Due to the effect of confinement, the enthalpy (average number of HB), entropy (ordering of HB) and consequently free energy of the confined water may be different from those of bulk water. When water is confined to a small volume, such as a nanopore, the water molecule interacts with one another differently than in bulk water. These interactions alter the enthalpy, entropy, and free energy of water molecules as well as their dynamics.

Water is expected to exhibit a lower entropy when it is confined because of its lower degrees of freedom. However, Pascal et al. using MD simulation observed that the filling of the hydrophobic carbon nanotube with moderate diameter is spontaneous and hence counterintuitive[29]. They investigated the entropy, enthalpy, and free energy changes for water confined in carbon nanotubes (CNTs) with diameters ranging from 0.8 nm to 2.7 nm. Firstly, it was discovered that water confined in CNTs is more stable than in bulk. This favorable confinement of water changed with CNTs' diameter. They observed a vapor-like phase for small diameter CNTs is stabilized by entropy; an ice-like phase for medium-sized CNTs stabilized with enthalpy; and a bulk-like phase for CNTs larger than 1.4 nm stabilized by increased translational entropy[29]. Consequently, it was revealed that the HB network structure (i.e. tetrahedral in bulk water) significantly depends on the tube diameter changes in confinement. In CNTs smaller than 0.8 nm, water loses an average of 2 HB per molecule. In contrast, CNTs larger than 1 nm lose one HB till 1.6 nm. In general, the degree of confinement and the intermolecular interactions between the water molecules and the confining material determine the entropy and free energy of confined water.

2.3 A few examples of water confinement at the nanoscale

The selective and fast transport of nanoscale confined water was observed naturally, in biological, geological, or artificial systems. Clays, Zeolites, and activated charcoal are examples of natural systems for nanoscale confinement. While, metal-organic framework, synthetic zeolites, and nanotubes are artificial systems for water confinement. Metal-organic frameworks, zeolites, and nonporous silica can be utilized to confine and trap water molecules in their nanopores, changing their structural characteristics[30]. On surfaces such as graphene or in nanoscale channels or slits wettability and surface tension can be altered[31]. Water can also be confined within nanoporous polymeric or ceramic membranes. The basic working principle of the membranes for water desalination is based on separating water from the salts and contaminants by selectively blocking ion transport through the pores. Here, maximizing the flow rate while retaining good pore selectivity is the major objective. Nanofiltration is also used to remove various pollutants, such as organic pollutants and heavy metal salts[32]. To improve the efficiency of these artificial systems a better understanding of water confinement is needed.

2.3.1 Natural systems

The nanoscale confinement of water is often observed in natural systems. For example, biological cells, clay minerals, and active charcoals. Aquaporins are biological channels found in cell membranes that allow water to pass through while excluding other molecules. These channels are less than 0.3 nm in diameter. Clay minerals and active charcoals have a structure that allows the adsorption of water molecules. The interlayer spacing where molecules are adsorbed is typically less than 1 nanometer, making it an effective system for nanoscale water confinement.

2.3.1.1 Aquaporins (AQPs)

The movement of water within biological elements is in particular regulated by aquaporins (AQPs), which provide a clear explanation for how our brain can absorb water, how people can salivate, sweat, or cry, and how our kidneys can concentrate urine. With the use of X-ray crystallography, AQPs were initially discovered in red blood cells[33]. In 2002, P. Agre et al. discovered that these channels operate at the nanoscale with a channel dimension of about 3 Å[8] (Figure 2.4a). It was then shown that the permeability across these channels is selective and transport is directed by an osmotic gradient. Furthermore, it was demonstrated that proton transport is highly energetically favorable. They were categorized into AQP0-AQP9, some of which are selective to solutes and are known as orthodox AQPs, while others are known as non-orthodox AQPs (aquaglyceroporins) also permeable to ions[34]. Little polar molecules and water have less resistance to permeating through AQPs than large molecules. The permeability of water is also very high compared to bulk.

Murata et al. noticed that hydrophobic residues account for quick water transport[35]. In AQPs, such rapid and selective water transport is controlled by hydrogen bonds that are formed at the molecular level. Hydrogen binding sites at the pore entrance are thought to be necessary for interrupting the continuous chain of HB along a single file of water molecules in order to block proton transfer[36] (Figure 2.4b). According to molecular dynamics simulations, the amount of time needed for water molecules to reorient, to break existing H-bonds, and to create new H-bonds limits the amount of water that can move through the single-file region[37]. As a result, it is considered that water does not move without friction across AQPs[38].

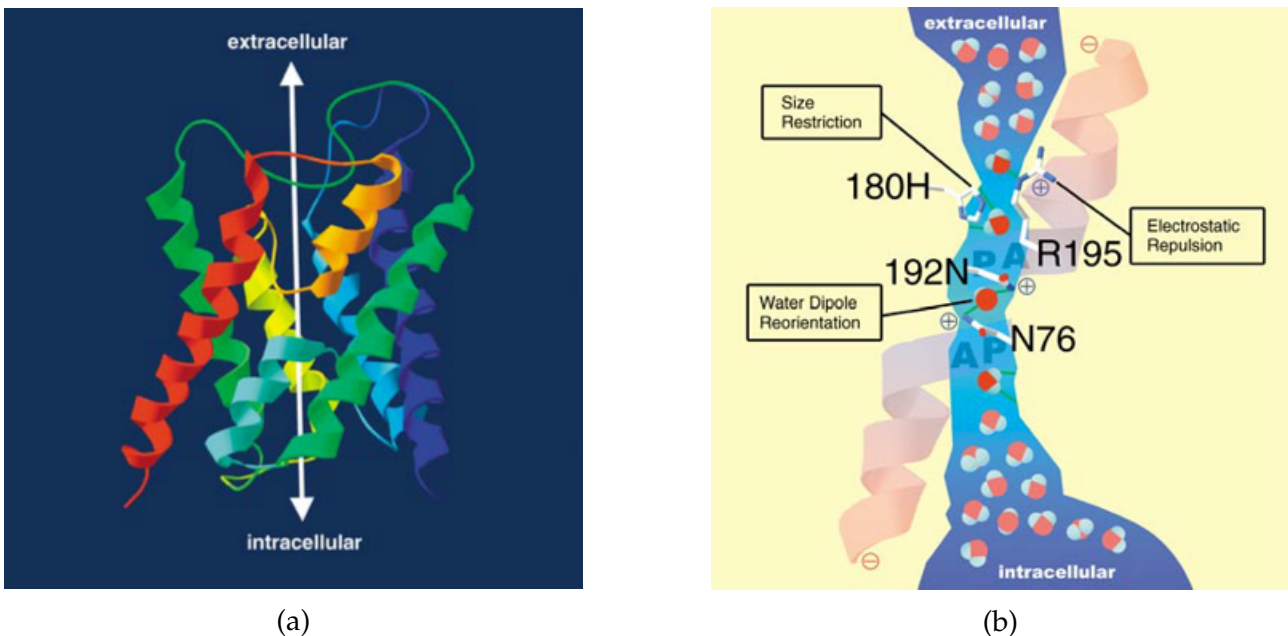


Figure 2.4: Aquaporins (AQPs): (a) 3D structure of the AQP1 subunit, (b) Schematic representation of the selective water flow (From [8])

2.3.1.2 Clay minerals

Clays as smectites are natural minerals with unique physicochemical properties such as high specific surface area, high cation exchange capacity, and high water-holding capacity in their nanoporosities. They have been extensively studied for water confinement and have many possible applications for various purposes such as water purification, water retention, and soil remediation. The swelling behavior of clay minerals structure underwater absorption was extensively studied. It was observed that the molecular packing of water molecules strongly influences swelling due to their interaction with exchangeable cations. Adapa et al. were interested in understanding the role of different cation hydration properties on the thermodynamics of clay swelling due to water adsorption[39]. They observed that the swelling capacity and stability of clay could change significantly depending on the exchangeable cations with hydration properties.

Caer et al. used IR femtosecond time-resolved experiments on water confined in the inter-layer space of montmorillonite to demonstrate that its behavior differs significantly from that observed in bulk neat water. The main difference between the liquid phase and the confined geometry was discovered to be anisotropy, indicating that there are no rotational motions. Gonzalez et al. also showed the impact of the interaction between the exchangeable cations and the confined water molecules as the dynamics of the latter using Neutron scattering[40]. In particular, it is shown that in uncharged clays water diffusion is faster than in the bulk due to the hydrophobicity of the surface.

2.3.1.3 Active charcoal

Activated charcoal, also known as activated carbon, is a common material used for water adsorption, purification, and confinement. It is a type of carbon that has been processed to have a high surface area and porosity, allowing it to absorb a wide range of contaminants such as organic compounds and heavy metals from water.

The dynamics of water confined in nonporous graphitic carbon structures were studied using molecular dynamic (MD) simulation. It has been observed that confinement has a significant effect on the dynamics of water molecules. They found that water molecules start to freeze at 190 K and the self-diffusion coefficient decline dramatically[41].

Adsorption isotherms and X-ray diffraction were used to explore the properties of water confined in activated carbon pores with an average diameter of 2 nm throughout a temperature range between 298 K and 228 K. The X-ray diffraction has revealed that the ice-like tetrahedral network of water is somehow disrupted by the bulk water structure. The hydrogen-bonded network of water was increased when the temperature was reduced, and hexagonal ice was partially produced in the activated carbon at 243 K[42].

Differential scanning calorimetry was used to study the freezing and melting behavior of water confined in the nanopores of activated carbon materials. Water confined in small pores with diameters less than 0.7 nm under atmospheric pressure. However, they did not exhibit phase transition which they interpreted as non-freezable water[43].

2.3.2 Artificial/synthetic systems

Artificial systems for water nanoscale confinement are materials and structures designed to confine water at the nanoscale level, typically with dimensions ranging from a few nanometers to a few hundred nanometers. These devices are fascinating because, among other things, they could be used for biosensing, energy storage, and water purification. Very small nanopores can be made in materials such as graphene or silicon nitride atomic layer. Controlling the flow of water molecules and ions through these nanopores can be useful for water purification processes. Metal-organic frameworks, zeolites, nanotubes, and mesoporous silica materials are other artificial systems for water nanoscale confinement. These structures can also be used to investigate the nanoscale behavior of water molecules and ions. Overall, artificial water nanoscale confinement systems have the potential to enable a wide range of technological advances and scientific discoveries in fields such as materials science, nanotechnology, and biophysics.

2.3.2.1 Zeolites

Zeolites can be found naturally in volcanic rocks as minerals, but most of the existing zeolites are synthetic. These are crystalline, three-dimensional, porous aluminosilicates with well-organized structures[44]. The behavior of the water molecule confined in zeolites is the direct result of various interactions between water, ion, and aluminum silicate frameworks[45]. The effect of these interactions (hydrogen bond, electrostatic, and ion-dipole) produce localized restrictions that change the behavior of water from that of bulk. Single-crystal zeolite nanomembranes are utilized as reverse osmosis membranes for seawater desalination because they have uniform pore sizes and high pore densities. It was found that salt rejection was almost flawless and that water permeability was two orders of magnitude more than predicted[46].

Experimentally, it was found that hydrophobic zeolites had an order of magnitude higher water permeability than hydrophilic zeolites[47].

2.3.2.2 Metal organic frameworks

Metal-organic frameworks (MOFs) are composed of metallic ions linking organic ligand in a 3D and periodic manner. They are nanoporous materials.

As for instance, the structure and dynamics of confined water as a function of relative humidity inside a MOF with ordered cobalt open coordination sites (CoCl_2BTDD) were investigated using infrared spectroscopy and MD simulations[48]. At low relative humidity, water bonds form short one-dimensional chains of hydrogen bonds. Then water chains nucleate as relative humidity increases, and finally water occupies the whole pore interior when the relative humidity reaches about 30 %.

2.3.2.3 Boron nitride and Carbon nanotubes (NT)

Carbon nanotubes (CNT) and boron nitride nanotubes (BNNT) are the most investigated nanotubes with diameters lower than 2 nm and can act as a channel for water confinement. The smooth hydrophobic surface of CNTs is a low friction interface, which induces a very

long slip length. When diameters are less than 1 nm, water molecules self-organize into a single file configuration, drastically changing the HB network.

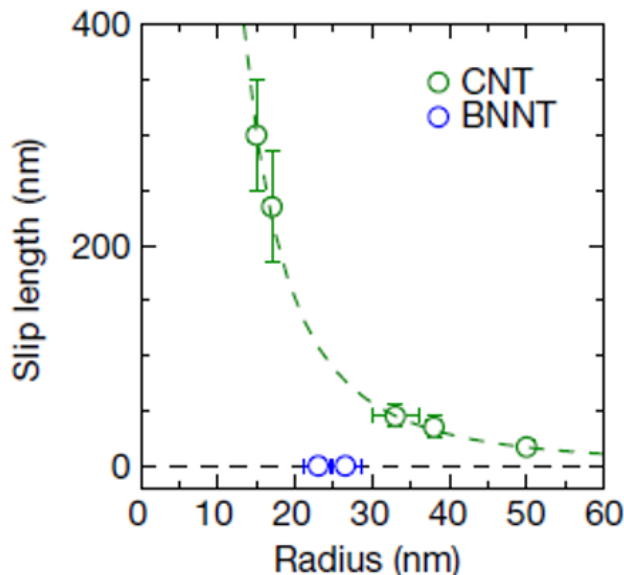


Figure 2.5: Slip length of water confined in a few individual MWCNT and BNNT (From [49])

Although BNNT and CNT have similar structures, boron, and nitrogen atoms form a more polar surface that can interact differently with water molecules than carbon nanotubes. BNNTs are wide-bandgap semiconductors with nearly insulating properties. Theoretical work on water permeation through SWBNNT has been reported[50]. SWBNNT conducts water, whereas the corresponding diameter SWCNT does not. It was assumed that a relatively strong interaction between the BNNT's nitrogen atoms and water molecules played a key role in the continuous wetting of the wall. Another theoretical work by Joseph et al. studied that despite the fact that the diameter of, their SWBNNT was 1.3 Å smaller than the diameter of their SWCNT, the axial diffusion coefficient and HB properties of water in these NTs were comparable. CNTs have the highest water velocity and flux among NTs of similar diameter when compared to BNNTs and hydrophilic silicon NTs[21].

Experiments with individual CNT revealed that as the diameter of the CNT diminishes, the values of the slip length became divergent and began to approach the single-chain nanopore regime. BNNT, on the other hand, has very small slip length values[49] (Figure 2.5). In contrast, one of the theoretical works predicted that CNTs have more charged surfaces, which therefore should interact strongly with water molecules, thus significantly slowing water flow through the tube. This prediction contradicts the difference observed in the water confinement between CNTs and BNNTs. The origin of this contradiction could arise from the exact atomic of the solid-liquid interface, including the electronic structure of the nanotube surface hence the possibility of quantum interaction, i.e. partly covalent bonding[51, 52].

2.4 Water confined in carbon nanotubes (CNT)

Carbon nanotubes with hydrophobic smooth surfaces and a high aspect ratio are promising materials for water confinement compared to other nanotubes. These nanostructures have unique electrical, thermal, mechanical, and optical properties. It was expected that water filling the hydrophobic interior of the CNT might reduce both entropy and energy of hydrogen bonding networking by breaking water-water HB and hence would not be spontaneous. On the contrary, it was reported that the filling is spontaneous since the free energy of confined water in the CNT is energetically more favorable than in bulk water. Confined water behaves differently than bulk water depending on the diameter of the nanotube. The principal predicted changes concern water phases. In this section, we will discuss theoretical and experimental works which have been carried out to understand the structure, phase change, and transport of water confined in the CNTs.

2.4.1 Theoretical studies

Molecular dynamic simulation (MD) has emerged as a powerful tool for studying the physical behavior of fluids by simulating atom and molecule motion. It is possible to obtain detailed information about molecular mobility and organization. Studying the phase behavior and structure of the nanoscale confined water is important for understanding its fundamental properties, and potential applications.

2.4.1.1 Structure of confined water

At the nanoscale, the structure of confined water is determined by the dimension and shape of the interface, as well as by the interactions between water molecules and the confining surface. In general, confinement impacts the hydrogen bond network near the wall, resulting in a change in the structure and dynamics of molecules. Water molecules in small channels or pores can form layered structures parallel to the confining surface. This can cause the formation of two-dimensional ice-like structures. Water confined within small tubes can form ordered structures like helical chains or one-dimensional ice-like structures. Hummer et al. were the first to report the spontaneous filling of a CNT with a diameter of 0.81 nm forms a one-dimensional ordered chain of water molecules[53]. However, in large-diameter CNTs, water molecules tend to form concentric layers. Based on MD simulation, Pascal et al. studied in detail the arrangement of the water molecules confined inside the CNT as a function of the CNT diameter. It was observed that water forms a single file chain in the smallest diameter ($d < 1$ nm), pentagonal ice-like water inside when the diameter is 1.1 nm, hexagonal ice-like with a diameter of 1.2 nm, and finally bulk-like in CNTs with diameters equal to or greater than 1.4 nm[29] (Figure 2.6). It was revealed that pentagonal ice-like water forms slightly more rigid and entropically more stable frameworks inside the CNT than hexagonal ice-like molecules. Interestingly, even at small CNT diameters, where water molecules form a single-file arrangement, water molecules have significant entropy because they freely rotate. It was also shown using MD that water could form a square ice sheet near the CNT wall and a chain-like configuration in the center[54].

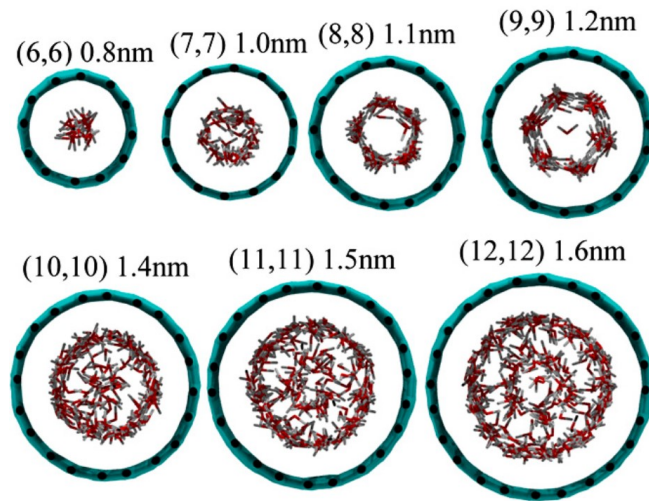


Figure 2.6: Confined water form different structure depending on CNT diameter (From [29])

2.4.1.2 Phase diagram of confined water in CNTs

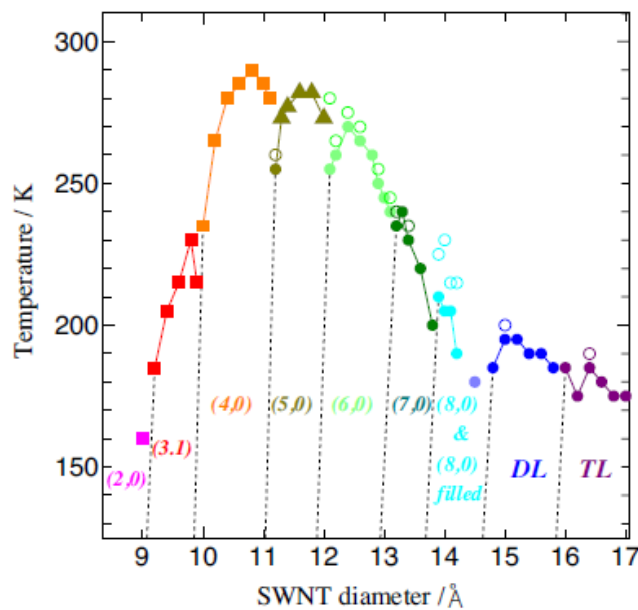


Figure 2.7: Melting/freezing temperatures of confined water as a function of SWCNTs diameter in the range of 0.9 - 1.7 nm at atmospheric pressure (From [55])

Water can exhibit complex behavior under strong confinement due to its anomalous properties. From MD simulation, Takaiwa et al. investigated the phase diagram of water confined inside SWCNTs with diameters ranging from 0.9 nm to 1.7 nm at atmospheric pressure in temperatures ranging from 100 to 300 K[55]. Their calculations revealed spontaneous freezing with at least nine ice phases. They mentioned that the ice in the smallest diameter CNTs is known as ladder-like ice, where each molecule is only engaged in three HB. Other types of ice included helical, square, pentagonal, hexagonal, heptagonal, octagonal, double, and triple-layer ice. When $d > 1,2$ nm, a liquid-solid change occurs discontinuously, whereas at smaller diameters of CNTs freezing to melting occurs continuously [55]. In Figure 2.7, full circles represent the freezing temperatures, and open circles are when the ice melts at

a different temperature upon heating. Triangles represent continuous freezing and melting, while squares represent the temperature at which an ice phase becomes unstable and breaks up when heated. The solid lines represent an estimate of the melting curves, while the dashed lines represent an estimate of the ice-ice phase boundary.

Farmani et al. explored the presence of multiple phases of water in CNTs at room temperature and pressure. They discovered that the ice-like layer which has the lowest entropy and highest density is one molecule layer thick and has an ordered rhombic structure near the wall. Between the ice-like layer and the wall, a vapor phase exists. They also observed continuous phase change from ice to liquid and then vapor. The presence of multiple phases of water near the interface could explain phenomena such as slip behavior and fast water transport[56].

2.4.1.3 Dynamics and Molecular transport

Another relevant issue in water confinement in CNTs is its diffusion properties. It has been demonstrated that the dimensional constraints and liquid-wall interactions enhance diffusion when compared to bulk water under certain conditions[57]. Furthermore, if the CNT is narrow enough ($d < 1$ nm), the dynamic process changes from classical Fickian to single-file diffusion. The filling of the hydrophobic interior of the CNT was debated until Hummer et al. reported for the first time that water could be filled forming a single file chain similar to the water arrangement in aquaporins. They calculated water transport through CNTs inserted into water reservoirs. Regardless of the CNT's hydrophobicity, the spontaneous filling was observed[53]. Flow enhancement correlated with structural properties change was obtained using CNTs with diameters of 1.66 and 4.99 nm. The flow rate enhancement with decreasing CNT diameter was attributed to a decrease in water viscosity and an increase in slip length at the NT surface[58]. Joseph et al. investigated the relationship between slippage and the nature of the confining material[21]. They reported that HB and water orientations affect the flow rates .

To understand the flow rate in detail, Falk et al. investigated the effect of curvature and confinement on friction between water and CNT surfaces. CNT with water inside or outside and water between two graphene sheets were all simulated using molecular dynamic simulation. It was shown that increasing the diameter of the CNT increases the friction coefficient inside while it decreases outside. Therefore, thanks to the low friction coefficient, large flow rates can be reached through narrow channels. Slip length was also calculated, and shown to decrease as CNT diameter increased, whereas constant slip length was reported for water confined between two graphene sheets with various distances, between 6.11 nm and 0.68 nm[59]. They also calculated the friction coefficient to predict slip length in CNT with diameters ranging from 1.62 nm to 6.5 nm. They obtained slip lengths ranging from 180 nm to 75 nm for diameters ranging from smallest to largest, as well as flow enhancement ranging from 870 to 90. Furthermore, for larger tubes, the slip length reached the one corresponding to graphene, i.e. 60 nm, indicating that curvature has a strong effect[60]. To sum up, the flow rate of water confined within the CNT exceeds the velocity of the bulk water.

2.4.2 Experimental works

A few experimental methods have been used to get insights into the properties of confined water. This includes X-ray and neutron scattering, which can be used to investigate the structural properties of confined water. Infrared spectroscopy can be used to assess the hydrogen bonding network. Nuclear magnetic resonance (NMR) is a technique that can be used to study the dynamics of water molecules. Based on the analysis of radial breathing mode (RBM) band shift, Raman can be used to gain information about the structure and phase diagram of confined water.

2.4.2.1 Structure

For the first time, single-file water transport into a CNT was observed experimentally through the shift of the radial breathing mode in Raman spectra. CNTs of various diameters, the smallest of which was 0.5 nm, were studied, and a single file chain structure was observed in the small diameter when both empty (closed) and water-filled (open) NTs were used[61]. Paienau et al. determined the radial density profile of water confined in the SWCNT at room temperature using X-ray scattering. They were able to identify the radial density profile during NT filling by analyzing the decrease in scattered intensity when exposed to water. They observed that the filling is uniform and structured into three layers depending on the amount of water molecules[62]. The filling of water into an opened SWCNT was identified using neutron diffraction and inelastic neutron scattering measurements in parallel with MD. Ice shell with a water chain structure was observed. It is observed that the ice phase formation is primarily due to a significant change in the central water chain's HB network[54].

2.4.2.2 Phase diagram

Some of the experiments used to gain information about water confinement investigated phase transition. Water adsorption in an SWCNT bundle was studied using X-ray diffraction. By observing the desorption and adsorption process of water, they discovered a phase transition from liquid-like into ice-like NT at 235 K for CNTs with a diameter around 1.37 nm[63].

Nuclear magnetic resonance spectroscopy was used to investigate the freezing temperature in SWCNT with a diameter of 1.2 nm, and within temperature interval ranging from 210 K to 300 K. It was observed that freezing of the water molecules occurs at nearly 212 K[64].

Infrared spectroscopy was used by Byl et al. to detect HB network and the bonding angle of water confined inside a CNT. They discovered unusual intra- and intermolecular HB structures with layered rings[65]. Thus, at higher temperatures, CNTs with diameters greater than 1.26 nm are predicted to have two liquid water phases, near the wall and in the tube center, which disappear upon cooling, resulting in a discontinuous liquid-solid phase transition.

The Raman spectroscopy method was used to determine the phase boundaries in SWCNT, with diameters ranging from 1.05 nm to 1.52 nm. A remarkable sensitivity to diameter was observed. It was noticed that the freezing transition is significantly higher (by nearly 100 °C) than the predicted MD simulation values[66]. Dynamic water filling and reversible freezing

transition have been observed by the shift of the RBM peak in the Raman spectra revealing the melting temperature ranges 105-151 °C and 87-117 °C for the SWCNTs with diameters 1.05 and 1.06 nm, respectively .

The melting point of confined water in SWCNTs with diameters ranging from 0.95 nm to 1.26 nm was also explored using photoluminescence spectroscopy. Encapsulation of water is identified as a change in the optical transition energy of SWCNT which was ascribed to the change in the dielectric constant of water[67].

2.4.2.3 Mass transport in CNT membranes

Because of their unique physical and dimensional (high aspect ratio) properties, carbon nanotube have been proposed as promising materials as membrane materials for the nanofiltration of water. CNT membranes have been shown to effectively filter out impurities and other contaminants from water while allowing water molecules to be transported quickly. For gas and water flow, the first experimental measurements were made with aligned double-walled CNT (DWCNT) membranes (inner diameter of the CNTs around 1.6 nm) sealed in SiNx ceramic. It was discovered that gas flow exceeded the predicted Knudsen diffusion model by more than one order of magnitude, while water flow rate surpasses the continuous hydrodynamic calculated from the Hagen Poiseuille equation under pressure-driven flow conditions by more than three orders of magnitude[68].

Whitby et al. used CNTs with larger diameters (10-100 nm) to observe flow rate enhancement. They reported that the flow rate exceeds the no-slip Poiseuille prediction by one order, but flow rate enhancement decreases dramatically as the diameter increases. Slip lengths of 113 nm and 177 nm were calculated[69]. Hind's group used chemical vapor deposition (CVD) to grow a vertically aligned CNT forest encapsulated in a polymer matrix. They observed successful water and ion transport through these membranes[70]. High water flux was observed by the same group through MWCNT membranes with CNT diameters in the 7 nm range[71]. Long slip length was reported, as well as more than four orders of magnitude increase in water permeability when compared to the prediction from the Hagen Poiseuille equation.

In a forward osmosis (FO) setup, high water flux was measured for water across from vertically aligned CNT membranes[72]. Despite their advantages, CNT membranes face several challenges before they can be used on a large scale. One challenge is scaling up CNT membrane production because current manufacturing processes are expensive. Controlling the selectivity of CNT membranes, which refers to their ability to filter out specific molecules while allowing others to pass through, is another challenge. Overall, CNT membranes remain a potential tool for water filtration in the future, but more research and development are required to make them commercially viable.

2.4.2.4 Mass transport in individual NTs

Investigating water transport at the level of individual NT makes possible to correlate this phenomenon more accurately with CNT properties such as chirality, in comparison to using CNT membranes. Qin et al. used a field effect transistor (FET) array to calculate the flow rate of water through individual ultralong CNTs with diameters ranging from 0.81 nm to

1.59 nm. With decreasing diameter, flow velocity values ranged between 46 and 928 $\mu\text{m/s}$. The corresponding slip length and flow rate enhancement range from 8-53 nm to 51-882, respectively. A discontinuity in the enhancement factor was observed in the diameter ranges of 0.98-1.10 nm, which was attributed to a transition from continuum to sub-continuum regimes[73].

In comparison to AQP1, Noy's group observed water transport through two types of CNT with diameters of 0.8 nm and 1.5 nm. For CNTs with 1.5 nm diameter, they observed bulk-like transport with flux lower than AQP-1[74]. However, CNTs with 0.8 nm diameter water flow exceeded that of AQP-1[75]. These findings confirm the data obtained on membranes but the exact mechanism of water transport within the NT remains under debate.

2.5 Conclusion

Carbon nanotubes are one of the best matrices to get insights into the properties of nanoscale confined water due to their unique geometry and surface features. The macroscopic law of hydrodynamics, as given by the Hagen Poiseuille equation with continuous description breaks down, when it is applied at the nanoscale. Because the smallest pore "squeezes" water molecules into a single file configuration, their HB network changes dramatically when compared to a continuum bulk water arrangement. Many theoretical and only a few experimental works have demonstrated that the filling of such small diameter channels is counter-intuitive to expectations: water filling is spontaneous. It was shown that the water molecules can form depending on the diameter of the CNT single file chain arrangement, exhibit peculiar "wet-dry" transition and melting temperatures, and enhance water flow significantly different from bulk water.

Despite the fact that this subject has been discussed for about two decades, the behavior of water confined at the nanoscale is still under debate. Because of the limited number of experimental results available so far and the lack of reliable experimental data with precise control of the individual CNT features, i.e. diameter, chirality, surface state, and so on. To gain reliable information, it is mandatory to be able to precisely relate the CNT's physical characteristics, i.e. diameter, chirality, surface state, and so on to the behavior of the water confined.

Manufacturing of a sealed Micro/ Nanofluidic device

Microfluidics and nanofluidic have gained popularity in a variety of research areas, including biology in the fabrication of biosensors for medicine; environmental monitoring in the sensitive analysis of pollutants, contaminants in air, water, and soil; energy and nanotechnology. Sealing the Micro/Nanofluidic device is one of the most challenging and unavoidable processes. Indeed, the majority of bonding methods and materials require strong surface activation (plasma, high temperature) or are not long-term stable, high-pressure tight, and vacuum compatible. The desirable vacuum compatibility of microfluidic devices recently gained popularity in the direction of highly sensitive mass measurements in liquid environments to weigh biomolecules and single cells. In these measurements, experiments are carried out under vacuum with microfluidic nanomechanical resonators and FETs[76, 77]. Therefore, it is advisable to have reliable and versatile sealing of microfluidic devices that are simple to fabricate and do not require aggressive chemicals, high temperatures, or high-energy plasma. The device should have high bonding strength, high-pressure leak tightness, long-term stability, and vacuum compatibility. In this chapter, we will discuss microfluidic device bonding methods such as direct and indirect wafer bonding to form μ -device, as well as its performance testing methods.

3.1 Direct wafer bonding

Direct wafer bonding is used to join hard surfaces such as silicon, glass, quartz, sapphire, diamond, and other materials. Because of its favorable physical and chemical properties, such as high thermal conductivity and chemical resistance, silicon (Si) is the most commonly used material. Quartz is used in applications operating in harsh chemical environments. Direct wafer bonding methods fall into two categories: fusion or anodic bonding.

3.1.1 Fusion bonding

Fusion bonding is based on molecular bonding principles. It entails bonding wafers without the use of any intermediate layers, adhesives, or bonding agents. Fusion bonding is used to bond a variety of materials such as silicon, glass, polymers, and plastics.

The main steps that occur during the fusion bonding process are sketched in Figure 3.1. The surfaces of both materials must be flat and clean in order to initiate fusion bonding. Surfaces are cleaned and activated either chemically or physically in order to make the surface either hydrophilic or hydrophobic. Following the cleaning and activation processes, the two wafers are brought together and annealed at high temperatures, ranging from several hundred up to thousands of degrees Celsius, while pressure is applied in a vacuum or inert gas environment to ensure intimate contact between the surfaces. The exact temperature and pressure conditions depend on the specific requirements of the bonding process. At such high temperatures, the wafers' surface atoms diffuse and form strong covalent bonds across the wafer interface[78]. Reptation refers to the movement of molecular chains in annealed substrates, while healing is the inter-diffusion of the chain when both wafers come into contact.

Fusion bonding has a very high bond strength and an atomically smooth bonding interface, making it ideal for high pressure with a bonding strength of more than 20 MPa[79] and low defect density applications. The technique is used in microfluidics, but it is also used for the fabrication of advanced microelectronic and optoelectronic devices, integrating electronic and photonic on the same substrate[80]. The main drawback of this bonding method is the requirement for high-temperature treatment.

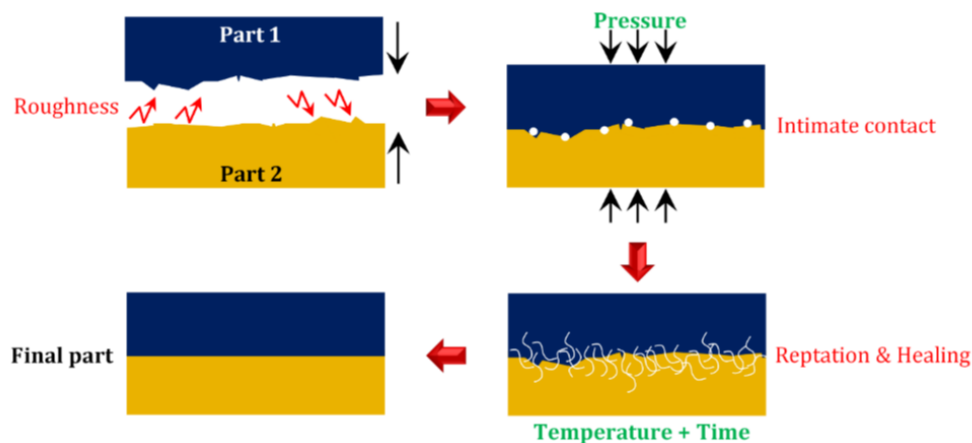


Figure 3.1: Schematic of the fusion bonding: Wafers bring in contact, intimate contact created with applying pressure and finally the device is heated at high temperature over a period of time (From [81])

3.1.2 Anodic bonding

Anodic bonding technique involves applying an electric field across the interface between the wafers in order to create bonding. It was discovered by Wallis and Pommerantz in 1969. They found that an electrical field could cause a bond to form between the metal foil and glass at 500 °C [82]. This method is based on ion migration principles, in which positive ions from one wafer are attracted to negative ions from the other, resulting in a strong bond with

a burst pressure of 0.3 MPa on glass bonding to Si[83] and bonding strength of more than 31 MPa[84].

Anodic bonding requires a lower temperature compared to fusion bonding: a few hundred degrees Celsius is sufficient to bond glass or silicon wafers. This bonding process is commonly used for device packing and bonding in MEMS/NEMS technology.

Bonding requires the wafer to be extremely clean in order to achieve intimate contact. Any surface roughness greater than 500 Å can prevent good bonding.

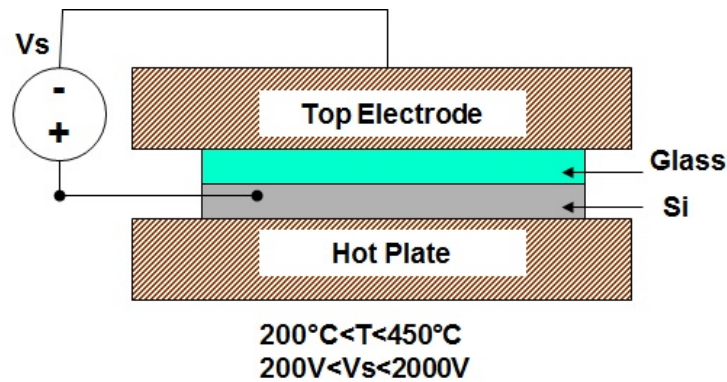


Figure 3.2: Schematic of the anodic bonding: high electric field is applied across the bonded interface while annealing and applying pressure (From [85])

As an example, glass wafers can be joined to silicon wafers using anodic bonding by heating at the temperature range of 200-450 °C while applying a high electric field in the range of 200-2000 V to the wafers[86] as sketched in Figure 3.2. The bonds begin at one point and spread across the surface, and the field generates a large electrostatic force that tends to pull the two wafers into close contact. The electric field causes positively charged mobile sodium ions to attract the glass. Owing to the influence of the combined electric field, temperature, and pressure, the wafer surfaces experience chemical reactions and molecular rearrangement. Finally, a very strong covalent bond is formed by ion exchange at both interfaces. Because of its significant advantages, such as optical transparency, chemical inertia, high and stable electroosmotic mobility, and good thermal conductivity, glass is a widely used material in direct wafer bonding processes. The creation of microfluidic channels in these hard surfaces requires the use of specialized techniques such as wet etching, chemical vapor deposition, and deep reactive ion etching. However, the anodic bonding process is not an ideal process for using glass substrates in microfluidics, because the applied high temperature during the bonding process can induce thermal stress into the glass and lead to the deformation or cracking of the substrate. The complexity of the bonding process and the difficulty to achieve uniform bonding across the entire surface limits this process to use in microfluidics .

Thus, direct wafer bonding is not as attractive as using adhesive layers to create structures and bonding.

3.2 Indirect wafer bonding

The process of bonding wafers with adhesive materials is known as indirect wafer bonding. Adhesive bonding is a quick, simple, and low-cost method for creating a uniform bond for microfluidic device fabrication.

Several polymers and adhesive films can be used in microfluidic chip sealing as an adhesive bonding material because of their great flexibility with specific properties. Polymers can be classified as elastomers, thermoplastics, and some epoxy photoresists such as SU-8. Elastomers consist of cross-linked polymer chains, such as polydimethylsiloxane (PDMS), polyethylene terephthalate (PET), and Norland Optical Adhesive (NOA). Thermoplastic polymers are materials that can be remolded several times by reaching their glass transition temperatures. These materials include polystyrene (PS), polycarbonate (PC), polymethyl methacrylate (PMMA), and so on. Polymers are called liquid adhesives while commercial adhesive films are called dry adhesives.

Liquid adhesives contain synthetic resins with photo or thermal initiators that form bonding when exposed to UV light or thermal heating respectively. Surface planarity, surface wettability, and adhesive layer thickness are the most important parameters to consider when using these materials. The most common liquid adhesive materials used in microfluidic device bonding are PDMS, PMMA, NOA, and SU-8. One of the challenges of using liquid adhesive is the inappropriate flow of the adhesive into the microchannel, resulting in channel clogging.

Dry-adhesive bonding materials are pressure-sensitive adhesive (PSA), doubly cross-linked nano-adhesive (DCNA), or adhesive tapes. Tapes such as Double-Coated PET tapes are dry adhesives. Tape thickness, bonding force, and substrate properties are important process parameters in dry-adhesive bonding. These materials reduce clogging, but thicker adhesive tapes are more likely to clog the microchannel. Clogging can be avoided by using the proper force and controlling the tape thickness[87].

One distinguishing feature of adhesive bonding is its ability to bond heterogeneous materials in "hybrid" (using various bonding techniques) microfluidics devices.

3.2.1 Polydimethylsiloxane (PDMS)

Polydimethylsiloxane (PDMS) is a silicon-based elastomer that is regarded as a fundamental building block in microfluidics (Figure 3.3). PDMS has become an attractive material for microfluidics because of its low cost and remarkable physical and chemical properties, such as wide temperature range, low stiffness, chemical inertness, biocompatibility, rapid prototyping, optical transparency, and non-reactivity[88]. These characteristics make PDMS a potential material for a variety of applications, including the fabrication of complex microfluidics systems[89]. Its low bonding temperature (less than 100 °C) makes it an excellent material for bonding elastomer substrates because many elastomer substrates cannot withstand a high-temperature treatment. Therefore, PDMS is gaining popularity in a wide range of fields beyond microfluidics, including biomedical applications[90], optical systems, drug delivery, implants, and photonics.

3.2.1.2 Pressure tightness, long-term stability of PDMS

Several methods exist for testing the bonding performance of microfluidic devices. Different device testing methods will be discussed in detail later (in section 3.2.4). Burst pressure refers to the maximum pressure that the device can withstand before observed leakage or failure. However, bonding strength refers to the quality of bonding between different layers in the device which can be tested by peel test or shear test measurement methods.

Here we will focus on the measured bonding performance of the PDMS-based microfluidic devices.

Using PDMS-based microfluidic devices for cell culture, Song et al fabricated a reversible and strong bonding of PDMS on polystyrene (PS) without the use of chemical reagents, which can have a negative impact on cell viability. In order to increase the bonding of PDMS and PS surfaces, the surface free energy is increased by adjusting the mixture of PDMS and curing agent and by treating the surface with O₂ plasma and annealing. They discovered that the stiffness of PDMS could influence its adhesion to PS. The treatment of PDMS and PS surfaces with O₂ plasma for 1 minute and annealing at 65 °C for 1 h stabilized bonding for more than 3 days. They also achieved a bonding strength of approximately 12 kPa for PDMS-PS[94].

Gonzalez et al. investigated the burst pressure of plasma bonding PDMS to a gold-patterned glass substrate. The burst pressure test demonstrated that using narrower gold electrodes that are inert to bonding can result in higher leak pressure. When the width of the gold pattern on the chips is reduced, a noticeable increase in leak pressure was observed. They measured burst pressure 238 ± 22 kPa for the narrowest gold pattern structure of 4 μm[95].

Saber et al. used a tensile strength and burst pressure test to determine the bonding strength of a PDMS microfluidic channel on a gallium arsenide (GaAs) substrate. They combined plasma O₂ treatment and annealing at 70 °C with a thin film SiO₂ intermediate layer on a GaAs substrate. The use of a SiO₂ intermediate layer enhanced the bonding of PDMS to GaAs, allowing the bonded chip to withstand up to 8.5 bar of burst pressure. Meanwhile, the study found that the sealed chips could achieve a high bonding strength of 2.01 MPa[96].

A room-temperature microfluidic bonding method was developed using a biocompatible adhesive layer and oxygen plasma treatment to create a strong bond between PDMS and polymethylmethacrylate (PMMA). The bonding quality of the PDMS-PMMA was evaluated through a burst pressure test and ~3.5 bar pressure was achieved[97].

The performance of the microfluidic device formed from PDMS & glass can be dependent on the level of the O₂ plasma surface activation and the uniformity of the glass surface.

The bonding strength of the PDMS & glass bonding using O₂ plasma was reported. It was observed that changing the wettability of the surface based on different levels of plasma exposure is a necessary parameter to achieve high bonding quality. It was observed that the plasma exposure decreases the contact angle between PDMS and glass, together with an increase in the bonding strength. The minimal value of the contact angle of 5° can be created in ICP with chamber pressure around 66 Pa, RIE power 20 Watts, and exposure time 30 seconds, resulting in a bonding strength of 3.2 bar[98].

The effect of the surface plasma activation on the bonding between PDMS and glass was also measured with peel test measurement. The bonding strength was measured around 7 N[99].

PDMS & glass bonding can be improved by enhancing uniformity of the glass surface while applying O_2 plasma. It was shown that 480 seconds of plasma exposure is enough to improve the uniformity of the bonded area, thus the burst pressure value of the device can reach up to 5.6 bar[100]. In an attempt to bond PDMS & glass without O_2 plasma, a silicon conformal coating material (dimethyl-methyl phenyl methoxy siloxane DMPMS), was used to bond PDMS & glass. This process only requires spin coating and curing without any functionalization of the surface. The bonding pressure measured is only 2 bars[101].

The PDMS durability was evaluated by Baraket et al. injecting a dye into the microchannel of the microfluidic devices, to observe optically the presence or absence of leakage. The microfluidic devices were formed by bonding PDMS with different thermoplastic films such as polyimide (PI), polyethylene naphthalate (PEN), and polyethylene terephthalate (PET) using (3-mercaptopropyl)trimethoxysilane (MPS) silane reagent. In order to form the device, first the polymers were hydrolyzed by KOH to form hydrophilic groups on the surfaces, then polymers were immersed in MPS at room temperature. And finally, O_2 plasma treatment was applied to initiate bonding. The devices were tested for long-term durability, and the liquid remained inside the microchannel for one month without degradation[102].

3.2.1.3 Drawbacks of PDMS

Numerous studies have revealed that PDMS is not a perfect material. PDMS has drawbacks, this includes small molecule adsorption, unstable wettability, leaching of the oligomers, water vapor permeability, and poor chemical compatibility[103]. These 5 drawbacks are sketched in Figure 3.4.

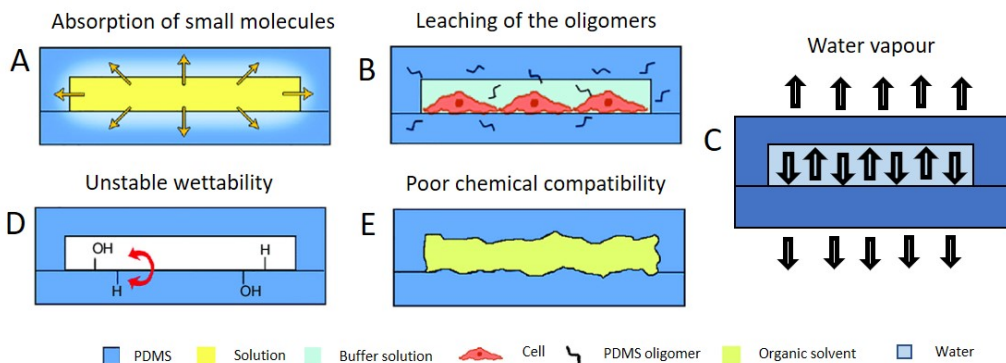


Figure 3.4: Schematic of the PDMS microfluidic chip drawbacks (From [104])

Small molecule absorption is caused by the porous structure of PDMS. It is an important issue for cell culture applications because it affects the concentration in the media, which can further affect signaling on cell behavior and function. Small molecules and molecules soluble in organic solvents can be absorbed by PDMS, affecting experiment accuracy and reproducibility. The permeability coefficients of various components in PDMS are shown in Table 3.1. When comparing large organic molecules to small molecules, the large differences in permeability are related to the interaction between molecules.

$$1\text{Barrer} = 10^{-10}\text{cm}^{-3}(\text{STP})\text{cm}/(\text{cm}^2\text{ s cmHg}).$$

The second issue is the leaching of PDMS uncross-linked oligomers (Figure 3.4b), e.g. uncross-linked chains that can freely diffuse throughout the bulk material. When these uncross-linked oligomers come into contact with the solution, they can leach out of the bulk and into the solution. These oligomers were discovered to be capable of incorporating into the membranes in cell culturing studies[105].

PDMS has water vapor permeability which can be attributed to its polymer chain with a high degree of internal free volume, allowing water vapor molecules to diffuse through the material (Figure 3.4c). The water vapor permeability of PDMS can be modified by parameters such as PDMS thickness, degree of cross-linking, and surface changes, but can not be suppressed.

The unstable surface property of PDMS caused by oxygen plasma treatment is another issue (Figure 3.4d). To facilitate chip bonding between similar or dissimilar materials, oxygen plasma is commonly used to convert hydrophobic PDMS surfaces to hydrophilic surfaces. Unfortunately, its polymer chains can replace the hydroxyl groups by diffusing from the bulk to the surface, resulting in hydrophobic recovery[107]. This may cause dynamic changes to the chip. Thus, PDMS devices with such surface treatment must be produced within hours before the experiments, which limits the engineers' ability to mass-produce devices in advance. Even when plasma activation is used to temporarily make the PDMS surface hydrophilic, the surface remains intrinsically hydrophobic. It oxidizes over time and the surface function changes to hydrophobic, causing for instance protein adsorption to the surface, which can affect the biological and chemical interactions that occur within the microfluidic channels.

Last but not least, PDMS has poor chemical compatibility, particularly with organic solvents (Figure 3.4e). PDMS dissolves in organic solvents, which leads to microchannel swelling and causes changes in the dimensions, integration, and surface characteristics of the channels[108].

PDMS sensitivity to temperature, pressure, and humidity can affect the mechanical properties and performance of the microfluidic device. PDMS can produce bubbles during fabrication and sealing, which can disrupt the fluid flow and reduce experiment reproducibility. It is worth noting that the hydrophobic nature of PDMS can be a huge advantage in other applications than microchannels such as implant coatings, solar panels, and face masks.

The bonding process of the PDMS-based microfluidic devices requires surface activation of at least one of the surfaces. While plasma activation makes the surface of PDMS hydrophilic to improve bonding, it can also damage the material's surface. It is therefore not suited for delicate materials deposited on a surface, such as nanomaterials.

Microfluidic devices have been extensively researched and developed, and in order to be

Table 3.1: Permeability of various components in PDMS at 40 °C (From [106])

Component	Permeability [Barrer]
nitrogen	280
oxygen	600
methane	940
carbon dioxide	3200
ethanol	53000
methylene chloride	193000
1,2-dichloroethane	248000
carbon tetrachloride	290000
chloroform	329000
1,1,2-trichloroethane	530000
trichloroethane	740000
toluene	1106000

commercialized, they must be low-cost and mass-producible. PDMS is not a material of choice for large-scale manufacturing because it requires molds, significant curing time, and considerable hand labor to unmold it after curing. For these reasons, PDMS has not gained the same traction in the industry as it has in academic research laboratories.

Overall, PDMS provides significant advantages such as optical transparency, ease of fabrication, and low cost, all of which are critical requirements for the fabrication of microchips. This material has a few drawbacks, including organic molecule adsorption, a hydrophobic surface, uncross-linked oligomer leaching, water vapor permeability, and poor chemical compatibility. These drawbacks also impact the fabrication of devices: the hydrophobic nature of PDMS imposes some constraints during fabrication and flow transport phenomena, particularly in biological applications.

3.2.2 SU-8

SU-8 is an epoxy-based negative tone photoresist developed by IBM in the mid-1990s that was initially used as a low-cost material for mold preparation, high aspect ratio patterns, and the formation of thick layers[109, 110].

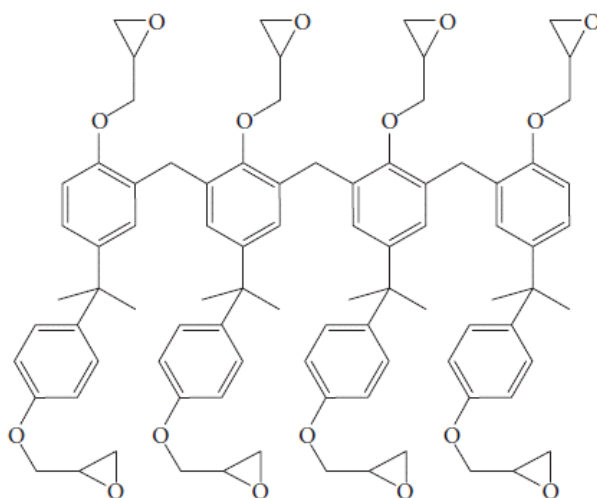


Figure 3.5: Molecular structure of SU-8 (From [111])

SU-8 photoresist is prepared by dissolving SU-8 resin in an organic solvent such as propylene glycol methyl ether acetate (PGMEA), cyclopentanone, or gamma-butyrolactone (GBL) together with a photoinitiator (triaryl sulfonium hexafluoro antimonate salt). Non-crosslinked SU-8 is a molecule containing eight benzene rings and eight epoxy groups as sketched in Figure 3.5. Its low UV absorption (up to 2 mm thickness), and high chemical and thermal resistance make it suitable for the formation of high aspect ratio structures.

The main advantages of the SU-8 photoresist are its thermal stability, chemical inertia (resistance to organic and acid solutions), optical transparency under near UV and visible light,

biocompatibility, low glass transition temperature, before cross-linking ($T_g=65\text{ }^\circ\text{C}$), compatibility with thin film deposition techniques, and a wide thickness range. Initially used as a replica molding of PDMS and other polymers, it was later used as a structural material or intermediate layer for adhesive bonding of microfluidic devices.

3.2.2.1 SU-8 for microfluidic devices

SU-8 is commonly exposed to UV light with a wavelength in the range of 350-450 nm. UV light with wavelengths shorter than 350 nm is strongly absorbed near the SU-8 surface. Selective filtration of the light source is frequently used to eliminate these unwanted shorter wavelengths (below 350 nm) and thus achieve better lithography results. MicroChem manufactures three different series of the product, including the SU-8 series which uses gamma-butyrolactone (GBL) as the casting solvent, SU-8 2000, and SU-8 3000 series which uses cyclopentanone instead of GBL. Cyclopentanone is a more polar solvent system that dries faster, resulting in better coating quality and higher process throughput[112]. Photoresists transparency to visible light above 350 nm, and biocompatibility, making it an excellent material for the fabrication of biological devices[113].

Because of the high functionality of the epoxy bonds, SU-8 can bond to a wide range of materials. The adhesive bonding of the SU-8 structures with a substrate is a simple and inexpensive method of sealing fluidic devices. This process is accomplished by applying pressure to the sample while heating it above T_g [114].

Dynamic mechanical analysis (DMA) was used to determine the glass transition temperature of cross-linked SU-8[115], and it was discovered that T_g varies between 150 °C and 240 °C depending on the level of cross-linking, which is dependent on the exposure dose and the post-exposure bake of the lithographic process[116].

It was observed that the applied pressure is one of the most crucial ingredient to get a higher bonding area. It was achieved that an applied pressure of 2.48 MPa produced the highest bonded area (90%). Lower-pressure bonded samples had less bonded area, while higher-pressure bonded samples had fractures.

SU-8 can be deposited and patterned in a wide range of thicknesses using a simple lithography process due to its sensitivity to both ultraviolet light and electron beams. The SU-8 pattern width can be varied from macroscopic to sub-micrometric. The latter requires bringing down the SU-8 thickness, which is accomplished by adding a solvent to SU-8, such as gamma-butyrolactone or cyclopentanone[117]. Thus, by using a simple lithography process, SU-8 photoresists can be used to form high aspect ratio structures, microchannels, multilayer structures, and metal-coated structures.

Abgrall et al. used various techniques to create SU-8 microfluidic devices, including successive lamination and patterning of SU-8 layers on existing topographies. They observed that SU-8 photoresists enable the coating of thick layers (up to 500 μm) on a single spin coat or thicker layers in multiple spin coatings[118].

A different type of resist profile should be obtained from the lithography process for different objectives. For metal lift-off undercut resist profile is required (resist sidewall $> 90^\circ$), resist sidewall $< 90^\circ$ enables continuous deposition of the thin resists, vertical (90°) resist sidewall angle is preferred when the resist is intended to act as a permanent structural element, such as in microfluidics and molding applications.

SU-8 photolithography is mostly performed on rigid substrates like silicon, quartz, and glass. It is preferable to choose a material with a coefficient of thermal expansion (CTE) close to SU-8 to obtain a reliable bonding.

3.2.2.2 Properties of SU-8 devices

Admassu et al. investigated the effect of bonding temperature, pressure, baking time, and thickness of the cross-linked SU-8 photoresist layer on the bonding strength of assembled microstructures. They discovered that lowering the exposure dose and post-exposure baking temperature has a significant impact on the bonding strength of assembled microdevice. SU-8 was used as an intermediate insulating adhesive layer to bond the device. This process had many advantages such as lower cost, the absence of electric voltage and current, and lower temperature processing. They were able to achieve a maximum bond strength of 1.3 MPa from the pull test. They explained that lowering the exposure dose and post-exposure temperature would inhibit hardening of the intermediate negative photoresist layer and increase softening of the SU-8 thin film, thereby enhancing device bonding strength[119].

The bonding performance of the SU-8 based device, where SU-8 is used to bond Si/pyrex was also reported with pull test measurement at 45 ± 15 MPa[120].

Bonding performance of the devices that SU-8 used as an adhesive layer to bond Si/Si or Si/pyrex was performed by tensile strength method and values of 20.6 MPa[121] and 30 MPa[114], respectively were reported.

Shear test and tensile strength test were carried out to measure the bonding performance of the glass/Si using SU-8 adhesive layer. It was reported that the device shear strength is 18-25 MPa and tensile strength is 20-40 MPa[122].

SU-8 is also used to bond glass or Si wafers with PDMS. The device performance was tested with tensile strength 1.4 MPa[123].

Liquid burst pressure test was carried out to test the bonding quality of PDMS to PDMS when SU-8 is used as an adhesive layer. The thickness of the SU-8 layer was in the range of 12-200 μm . The device could withstand about 0.1 MPa liquid pressure for 2 days[124]. The performance of the glass-glass wafers bonding using SU-8 adhesive layer was also tested with liquid leakage test and 1 MPa burst pressure was reported with durability for 2 days[125]. The highest liquid burst pressure bonding strength on SU-8/glass device so far reported was 3.8 MPa[126].

The bonding process of SU-8 devices is frequently limited because bonding of SU-8 layers usually requires the use of a special bonding apparatus. Naryan et al. presented a dependable and user-friendly SU-8 layer bonding method that simplifies the fabrication of SU-8 microfluidic devices. In this method, the top layer and main layer of a SU-8 channel were bonded at different applied pressures while curing at 110 °C. The resulting bonding was void-free in all cases, with a maximum bond strength of 6.5 ± 1.9 MPa[127]. Under flow conditions, all of the devices demonstrated excellent stability. The device was tested for 24 hours under flow shear stress with the lowest applied pressure (1 kPa) and showed no leakage. This type of bonding using low pressure is a promising method for fabricating SU-8 microfluidic devices[127].

Overall, the bonding strength of the devices where SU-8 was used as an adhesive material

to bond various layers had been mainly tested with tensile strength or shear method presented the performance in the range of from 1 MPa[119] up to 45 MPa[120]. The works have reported that the liquid burst pressure tightness of the SU-8 when used as an adhesive material is ranging from 0.1 MPa[124] up to 3.8 MPa[126].

The outgassing characteristics of cross-linked SU-8 layers were studied qualitatively and quantitatively using mass spectrometry (MS) and gas chromatography (GC-MS)[128]. The influence of hardbaking SU-8 was measured, and it was discovered that a hardbake is required to provide good performance in Ultra High Vacuum (UHV) environments. Firstly, it was claimed that hardbake can promote cracks[129]. However, later it was reported that hard baking can provide stress, which can overcome cracking and adhesion issues[130]. Thus, it was stated that hardbake steps can have a significant positive impact on adhesion strength[131]. The qualitative (MS) and quantitative (GC-MS) measurements show that a hard-bake of 150 °C is very beneficial for outgassing from SU-8 structures and that the rate of outgassing is inversely proportional to time. Benzene, 2-propenal, GBL, propylene carbonate and di-phenyl-sulfide were found as the main volatile components.

3.2.2.3 Limitation of SU-8

Some limitations of SU-8 photoresists include autofluorescence, high CTE, and low thermal conductivity. The difference in CTE between SU-8 and common substrates such as Si or glass produces stress and may cause film cracking. Because the absorption spectrum of SU-8 has much higher absorption coefficients at shorter wavelengths, lithography with a broadband light source tends to result in overexposure at the resist layer's surface and underexposure at the resist layer's bottom.

Overall, SU-8 photoresist is suitable because of its chemical, thermal, and strong mechanical properties, and biocompatibility for low-temperature bonding without requiring strong surface activation which can damage devices. This material is readily used to form the microfluidic channel, high thickness, high aspect ratio structures, and fabricate devices among many applications. It presents very few drawbacks and it overcome most of the disadvantages of the so far mostly used PDMS material, thus SU-8 can lead to extending the application area of the microfluidic devices.

3.2.3 Other adhesives: PS, PC, PMMA, and NOA

There are some other thermoplastics and polyester are used in the microfluidic device bonding, such as polystyrene (PS), polycarbonate (PC), polymethyl methacrylate (PMMA), and Norland Optical Adhesive (NOA).

Polystyrene (PS) is transparent, biocompatible, chemically inert, and mechanically rigid[132]. Using different chemical and physical surface activation methods such as corona discharge, gas plasma, and irradiation can modify its hydrophobic surface to hydrophilic. Fabrication of microfluidic channels with this material requires injection molding and hot

embossing methods which can limit its application[133].

Cell culture on PS microfluidic device is its main application[134]. The surface can be modified to enable cell growth and adhesion, by applying an oxygen plasma prior to bonding. However, O_2 plasma can change bond performance by modifying the chemical composition onto PS. The application of PS in microfluidic chip formation can present other limitations such as difficulties in thermal bonding when the aspect ratio of the microchannel is high.

Polycarbonate (PC) is formed through the polymerization of bisphenol A and phosgene, resulting in carbonate groups. Due to its high glass transition temperature ($\sim 145^\circ\text{C}$) and transparency in visible light, PC is used in DNA thermal cycling[133]. PC has high impact resistance, and minimal moisture absorption[135]. However, PC has lower resistance to certain organic solvents and low UV absorbance. The thermal bonding method is used to bond the device with the PC. However, it does not provide good bonding if a low temperature, 135°C is used. On the other hand, when that temperature is too high, it dramatically changes the channel geometry[135].

Among thermoplastics, PMMA is a commonly used material in microfluidics device bonding. It is an alternative to polycarbonate (PC), however, PMMA does not contain harmful bisphenol-A which is found in PC. Due to its mechanical properties, optical transparency, and compatibility with electrophoresis[136], it has been used in numerous microfluidic applications [137, 138]. PMMA structure may be manufactured using a number of processes including, injection molding, hot embossing, laser ablation, and UV lithography[136].

However, sealing of PMMA devices is more difficult than for instance PDMS, and relies on methods that can change the morphology of the device. The first one is thermal bonding. It is the most commonly used PMMA bonding technique. In this method, PMMA is heated above the glass transition temperature (T_g ranging from 85°C to 165°C depending on the composition[139] usually around 110°C [140]) and pressed together. The diffusion of polymer chains across two surfaces during thermal bonding leads to the formation of traps among the macromolecules[141] and permanent bonding.

PMMA microfluidic chips have been designed by using solvent and sacrificial materials to prevent channels from collapsing during the bonding [142].

At low temperature (70°C) and low pressure (1.6 MPa) ethanol was used as a solvent to bond different PMMA layers. The bonding strength of 1.5 MPa and burst pressure of 6.2 MPa was achieved by pressing PMMA layers for just 2 min at 70°C and 1.6 MPa. Bonding stability was demonstrated at 90°C (dry conditions) and 37.5°C in water for 216 h[143].

PMMA was also bonded using acetic acid as a solvent followed by 30 seconds of UV irradiation. The bonded PMMA achieved a bond strength of 11.75 MPa without the use of external hot embossing equipment and clogging-free microchannels were created under moderate conditions. After 3 days of cultivation, the microchannels of the device enabled cells with great viability and adhesion[144].

PMMA has numerous advantages to be used in microfluidic device bonding, however, it has low chemical resistance to organic solvents, aggressive chemicals[145] and low heat resistance[146] which limits its application.

Norland Optical Adhesives (NOA63 or NOA81) are transparent in the visual wave range.

This liquid polymer cures when exposed to UV, but NOA81 presents lower auto-fluorescence and thus it is better suited to fluorescence detection-based applications such as capillary electrophoresis experiments[147]. NOA81 has improved chemical resistance to strong solvents, is impermeable to air and water vapor, and is less prone to swelling upon contact with fluids[148].

Thin films of NOA and polyester were prepared to form an adhesive film. Using NOA, a high burst pressure of 12 MPa was obtained in a glass-polymer-glass device[149]. For comparison, the polyester/glass device tolerated a pressure of 0.22 MPa[148].

Even though NOA is a suitable material for microfluidic device forming, it has several limitations in terms of thermal stability, UV sensitivity, and surface properties such as wettability or hydrophobicity, which limits its application in microfluidic device fabrication.

3.2.4 Device testing methods

Leakage can be a huge problem in real-world testing. In biomedical applications, such as diagnostic medical devices, leaks can lead to the loss of blood analytes. In therapeutic devices, leaks can lead to leaching, toxicological safety risks, and drug delivery systems that can prevent the intended drug dose from being delivered to a patient.

In the application of microfluidic devices, high bonding strength, and long-term stability are desired. There are several methods for testing the bonding performance of the device. Visual inspection, leakage testing, shear testing, peel testing, and burst pressure are some of the methods used and are detailed in this section .

Visually inspecting the bond quality by looking at the interface between the bonded surfaces under a microscope is one of the simplest methods. The bond line can be examined for any gaps, bubbles, or delamination. It is frequently employed as a first method of characterization, although it is not sufficient to detect small leaks. In the burst pressure method, the pressure of the gas or liquid is gradually increased until the reliability of the bonded structure is compromised by delamination and leakage. Filling the microfluidic device with a dye solution and monitoring for leaks is the leakage testing method. If the dye leaks out, it indicates a weak bond and requires additional bonding. In the shear test or tensile strength method, a shear force is applied to the bond line, and the force required to break the bond is measured. In the peel test method, a tensile force is applied to the bond line and the force required to peel the bonded surfaces apart is measured.

Shear, peel test methods evaluate device stability and adhesion strength between layers of microfluidic devices, respectively. However, these methods do not assess the sealing quality or bonding performance of the device. The leakage and burst pressure testing methods are better to get insight into the bonding quality of the microfluidic device. The leakage method determines defects or weak points in the device, and the burst pressure method evaluates the resistance to the pressure of the device without failure.

Choosing of the method to test bonding quality depends on the specific application and requirements of the microfluidic device. In this section, we will present the most commonly used bonding test methods, as well as some quantitative data obtained while using various wafer bonding techniques and materials.

3.2.4.1 Tensile strength

The maximum stress that a material can withstand before breaking under tension is defined as its tensile strength. In other words, the tensile strength of a material is a measure of its ability to resist being pulled apart. In contrast, Young's modulus is a measure of a material's stiffness or resistance to deformation under stress. Tensile strength and Young's modulus are related in the sense that materials with higher Young's modulus tend to have higher tensile strength. This is due to the fact that a material's resistance to stress deformation (Young's modulus) is proportional to its ability to withstand tensile stress without breaking. This means that materials with higher tensile strength are stiffer and more resistant to deformation. However, this relationship is not always straightforward because other factors such as microstructure and chemical composition can also influence a material's tensile strength. Plastic materials such as polymethylmethacrylate (PMMA) and polystyrene (PS) are bonded together with a hot-press bonding method which requires well-controlled temperature and time[150]. Depending on the molecular weight of the materials and the process temperature, the bonding strength of devices that used these materials ranges from 110 kPa to 1.6 MPa[151].

The bonding quality of the PDMS-based devices was characterized. A bonding strength of 406 kPa for PDMS/PMMA bonding was achieved by using promoters to enhance the quality of the bonding[152]. The bonding strength of the PDMS and SU-8 was reported to be more than 1.4 MPa[123]. Kersey et al. studied PDMS adhesion to silicon, glass, and aluminum substrates and they achieved the bonding strengths of 0.841 MPa, 0.847 MPa, and 0.488 MPa, respectively[153]. Plasma bonding is the most commonly used method for PDMS-based channel sealing. The bonding strength for PDMS-PDMS using this method has been reported to be around 300 kPa[154].

The tensile strength of the devices, where SU-8 is used as an adhesive material to bond hard surfaces is presented in section 3.2.2.2 in the range of from 1 MPa[119] up to 45 MPa[120].

3.2.4.2 Burst pressure

The maximum internal pressure that the device can withstand before failing is referred to as burst pressure. Burst pressure is a critical criteria, especially for devices where failure is not tolerated or in high pressure applications. Burst pressure tests are performed with liquid or gas. To determine the burst pressure, the device is slowly pressurized, either continuously or stepwise, until it fails, which is usually when leak is detected. Real-time pressure monitoring or visual inspection can easily detect burst pressure. The duration at each pressure step is determined by the specified minimal leak rate tolerated, the minimally detectable leak rate, and the device's intended use duration.

The development of a doubly cross-linked nano-adhesive (DCNA) for the bonding of various heterogeneous substrates has been reported. The DCNA enabled the fabrication of microfluidic devices on both rigid (silicon wafer and glass) and flexible (PDMS, PET, and PI) substrates. The burst pressure of the DCNA-sealed devices was greater than 2.5 MPa, with a maximum burst pressure of 11.7 MPa. DCNA's resistance to chemical, thermal, and mechanical stresses, such as long-term exposure to strong organic solvents and heat, enables its use in low-cost, flexible substrates, particularly in harsh environments[155].

The highest burst pressure ever achieved for PDMS-based devices was 8.5 bar between

PDMS and GaAs (with SiO₂ deposited on top of the GaAs layer)[156].

Burst pressures between PDMS and various materials have been reported such as PDMS & Glass 5.1 bar[98]; PDMS & PDMS 6.7 bar[154]; PDMS & SU-8 1.5 bar[157]; PDMS & glass/ Au 2.68 bar[95]; PDMS & PTE 4.7 bar[158]; PDMS & PMMA 6.6 bar[159].

It was reported that when compared to other interlayer materials, using SiO₂ as an intermediate layer in the thermoplastic materials bonding demonstrated good performance in the burst test, reaching 436.65 kPa[160].

The liquid burst pressure of the SU-8 based devices is presented in section 3.2.2.2 ranging from 0.1 MPa[124] up to 3.8 MPa[126].

3.2.4.3 Liquid leakage

Liquid leakage testing is an important step in the fabrication and quality control of microfluidic devices because it ensures that there are no leaks or defects that could lead to inaccurate results, inconsistent flow rates, or sample contamination. There are several methods for testing the leakage of microfluidic devices. In the visually inspection method, the device is tested for any visible leaks, such as cracks or gaps.

The fluorescence microscopy method is used to detect leaks in the microfluidic channels after a fluorescent dye is introduced into them.

Last but not least, in the electrical resistance method, the microfluidic channels are subjected to an electrical current, and any leaks are detected by changes in resistance.

The choice of the corresponding testing method will be determined by the specific application and the device's sensitivity to leaks. Leakage testing should be done on a regular basis because leaks can occur over time due to changes in temperature or pressure, among other factors .

Leakage testing is especially important for microfluidic devices sealed with PDMS because PDMS is a porous material that can absorb small molecules and molecules soluble in organic solvents, affecting experiment accuracy and reproducibility. Furthermore, PDMS can swell in some solvents, causing the microfluidic channels to deform, potentially leading to leakage.

3.2.4.4 Gas leakage

Gas-based testing utilizes a large variety of external and internal sensing methods than liquid-based testing. This is non-destructive and suitable for large-scale production (using compressed air, nitrogen, or helium). The main difference between gas and liquid leakage test is governed by viscosity. Gas-based leakage testing may not be suitable when permeable materials like PDMS are used, or in cases where the leakage is influenced by the interactions between the device materials and the flowing medium. Liquid-based leakage testing is a bit less common for quality control assessment because of the contaminating and destructive nature of this test.

3.3 Conclusion

Microfluidic has gained popularity over the last decades in different areas ranging from electronics to biology and medicine. Sealing the microfluidic devices and choosing the corresponding bonding technology is challenging .

Direct wafer bonding and indirect wafer bonding have been presented as well as the methods to test the device bonding quality. Direct wafer bonding is used to bond hard surfaces, but this method requires special equipment, also it is expensive to create microfluidic channels in the hard surfaces. The indirect wafer bonding method uses an adhesive as an intermediate layer, and is a simpler and low-cost process. PDMS is mostly used material in this process because of its remarkable physical and chemical properties, optical transparency, and biocompatibility. However, it has many drawbacks such as absorption of the small organic molecules, hydrophobicity, and swelling.

All the reported bonding methods are not applicable in the case where sensitive, delicate materials are deposited on one of a surface (biological tissue, fragile nanomaterials, etc.) because these bonding methods require strong surface plasma activation, high temperature or chemicals which can destroy the material on the surface.

The use of UV-curable adhesives such as SU-8 relaxes some of these requirements. SU-8 photoresist is chemically inert, thermally stable, and biocompatible, it allows to make thick patterns and high aspect ratio structures. In addition, it is suitable for devices with high tensile bonding strength and high burst pressure leak-tightness over a long time.

In the Chapter 5, we present our work on a simple and low-temperature bonding process based on the SU-8 photoresist, which is microscale processable, shows high liquid water pressure leak tightness, long term stability and vacuum compatibility.

CNT, CNTFET, and interaction with water

Carbon nanotube-based field effect transistors (CNTFETs) are appropriate materials for chemical and biological sensor applications due to their outstanding properties and sensitivity. As water molecules are the primary component of biological materials, it is essential to understand the effect of water adsorbed at the outer surface and confined inside the CNTs. Adsorption from the environment is known to generate hysteretic behavior and irreproducible transport phenomena in CNTs. The electrical sensitivity of CNTFETs to water is therefore an essential tool to reveal the mechanism behind water and CNT interactions. Thus, in this chapter, we will discuss the fundamentals of CNTs, their growth, and the principle of CNTFETs, followed by a summary of the influence of water adsorbed on the outside wall of the CNT, as well as a few works on water confined inside the CNT.

4.1 CNT synthesis and giving features

4.1.1 CNT structure

A Single wall Carbon nanotube (SWCNT) is conceptualized by rolling a graphene layer (a single sheet of graphite) up into a seamless cylinder while the ends of the tube are closed with fullerene-like caps[161]. Because of their cylinder shape and hexagonal arrangement of the carbon atoms which form sp_2 hybridized bonding, they are considered 1D nanomaterials. The direction along which the graphite sheet is wrapped to form the CNT determines its chirality. The direction is defined by a vector known as a chiral vector or roll-up vector (\mathbf{C}_h), which can be expressed as a linear combination of the unit translational vectors in the hexagonal lattice (Figure 4.2).

$$\mathbf{C}_h = n\mathbf{a}_1 + m\mathbf{a}_2 \quad (4.1)$$

where, m and n are positive integers called chiral indices ($m \leq n$), while a_1 and a_2 are the lattice vector of graphene. The lattice vectors are related with a_{cc} which is the inter-atomic distance between neighbor carbon atoms, i.e. 1.42 Å.

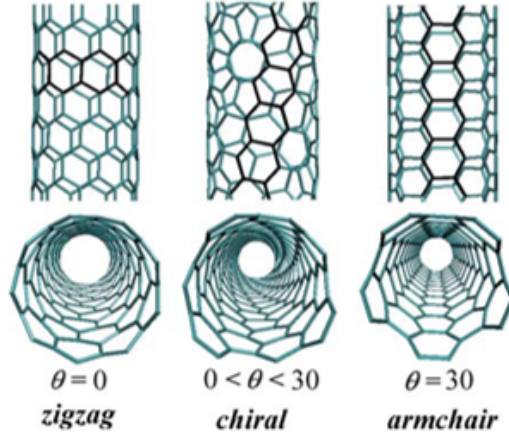


Figure 4.1: Different types of CNTs based on their chirality (From [162]).

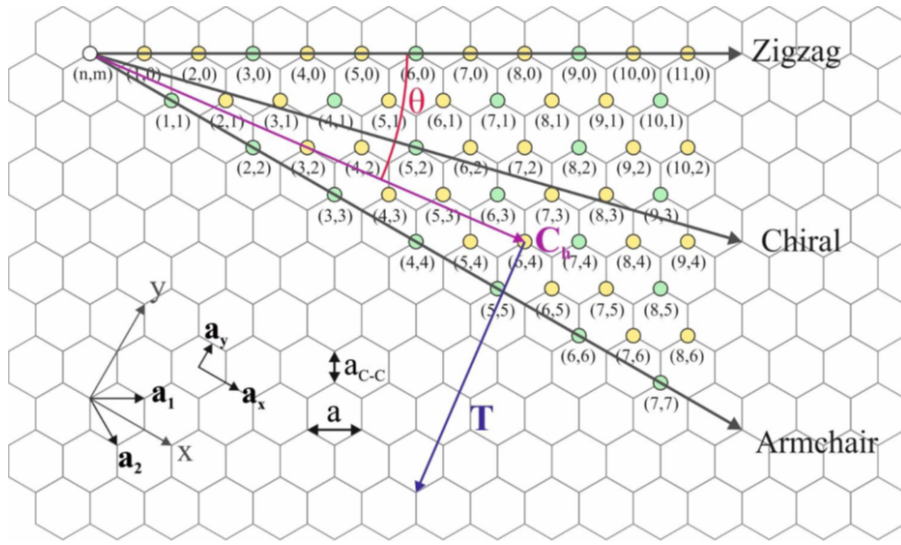


Figure 4.2: CNT indices on hexagonal graphene lattice (From [163]). See table 4.1 for element designations.

Table 4.1: Parameters of the CNTs (From [164]).

Parameter	Name	Formula	Value
a	Length of unit vectors	$a = \sqrt{3}a_{CC} = 2.46 \text{ \AA}$	$a_{CC} = 1.42 \text{ \AA}$
$\mathbf{a}_1, \mathbf{a}_2$	Graphene unit vectors	$(\frac{\sqrt{3}}{2}, \frac{1}{2})a, (\frac{\sqrt{3}}{2}, -\frac{1}{2})a$	x, y coordinates
\mathbf{C}_h	CNT chiral vector	$\mathbf{C}_h = n\mathbf{a}_1 + m\mathbf{a}_2$	$0 \leq m \leq n$
C_h	Chiral vector length	$C_h = \mathbf{C}_h = a\sqrt{n^2 + m^2 + nm}$	
d_t	CNT diameter	$d_t = \frac{C_h}{\pi}$	d_t is an integer
θ	Chiral angle of nanotube	$\tan \theta = \frac{\sqrt{3}m}{2n+m}$ $\sin \theta = \frac{\sqrt{3}m}{2\sqrt{n^2+m^2+nm}}$ $\cos \theta = \frac{2n+m}{2\sqrt{n^2+m^2+nm}}$	$0 \leq \theta \leq 30$
\mathbf{T}	CNT translation vector	$\mathbf{T} = t_1\mathbf{a}_1 + t_2\mathbf{a}_2$ $t_1 = \frac{2m+n}{d_R}, t_2 = \frac{2n+m}{d_R}$	t_1, t_2 are integer
d_R	Greatest common divisor ($2n + m, 2m + n$)	$d_R = d: n - m$ not multiple of $3d$ $d_R = 3d: n - m$ a multiple of $3d$	$1 \leq d \leq n$ $1 \leq d_R \leq 3n$
T	Length of translation vector	$T = \mathbf{T} = \frac{\sqrt{3}C_h}{d_R}$	
N	Number of hexagons in unit cell of CNT	$N = \frac{2(n^2+m^2+nm)}{d_R}$	

CNT diameter (d_t) can be calculated from the length of the chiral vector (C_h), ($C_h = |C_h|$) (see Table 4.1) with the following equation[165]:

$$d_t = \frac{C_h}{\pi} = \frac{a\sqrt{n^2 + m^2 + nm}}{\pi} \quad (4.2)$$

The helicity of the SWCNT is defined with chiral angle and chiral indices. The symmetric rolling of the graphene sheet leads to two types of achiral SWCNT, which are known as zigzag ($m, 0$) with chiral angle $\theta = 0$, and armchair with equal chirality (m, m) and the angle $\theta = 30$ (Figure 4.1). All other SWCNTs are generally referred to as chiral SWCNTs[166].

CNT can also be formed by the rolling of several layers of graphene thus resulting in concentric tubes in which the interlayer distances correspond to the one in turbostratic graphite. These CNTs are called multiwall carbon nanotubes (MWCNT). Furthermore, when individual carbon nanotubes come into contact with one another, they can interact and form bundles due to attractive van der Waals forces.

4.1.2 Synthesis, impurity, and purification of CNTs

Because of their remarkable mechanical, electrical, and optical properties, CNTs-based composites have attracted great interest. However, the main concerns with CNTs' uses are still related to their large-scale manufacture, purification, processability, and manipulation. CNT synthesis methods are broadly classified into three categories: arc discharge, laser ablation, and chemical vapor deposition (CVD).

The arc-discharge method was first developed by Iijima in 1991, which is based on the deposition of CNTs on a graphite cathode thanks to the action of an arc-discharge in an inert gas atmosphere (Figure 4.3a). The bulky graphite rod operates as the cathode, while the small graphite rod acts as the anode. To prevent CNT oxidation, the reactor is filled with inert gases such as helium and argon. The synthesis process is typically carried out under specific conditions such as current and voltage, as well as elevated temperature and reduced pressure. The graphite and metal catalyst of the anode graphite rod is vaporized and consumed constantly under the high-temperature plasma, and CNTs are deposited on the graphite cathode after the action of the metal catalyst[167]. This approach yields a complex mixture of carbon components (including fullerenes, amorphous carbon, and some graphene sheets)[168]. It is feasible to selectively grow SWCNTs or MWCNTs by varying the conditions (pressure, temperature, various gases, and catalytic metals). However, there is minimal control of the length and diameter of the CNTs using this method (see Table 4.2).

In the laser ablation process, a piece of graphite is placed in a vacuum furnace that is filled with an inert gas, i.e. helium, under high-temperature conditions (Figure 4.3b). Irradiating the targeted graphite with a high-energy laser beam locally causes carbon and metal catalysts to evaporate and be transported to the high-temperature zone. Finally, carbon atom clusters can be deposited on the collector to produce CNTs[173]. The most important advantage of this approach is the excellent purity of the yield and the minimal number of defects. However, this approach has a high investment cost and significant energy consumption which makes it unsuitable for large-scale synthesis; only bundles or an individual SWCNT are produced (see Table 4.2).

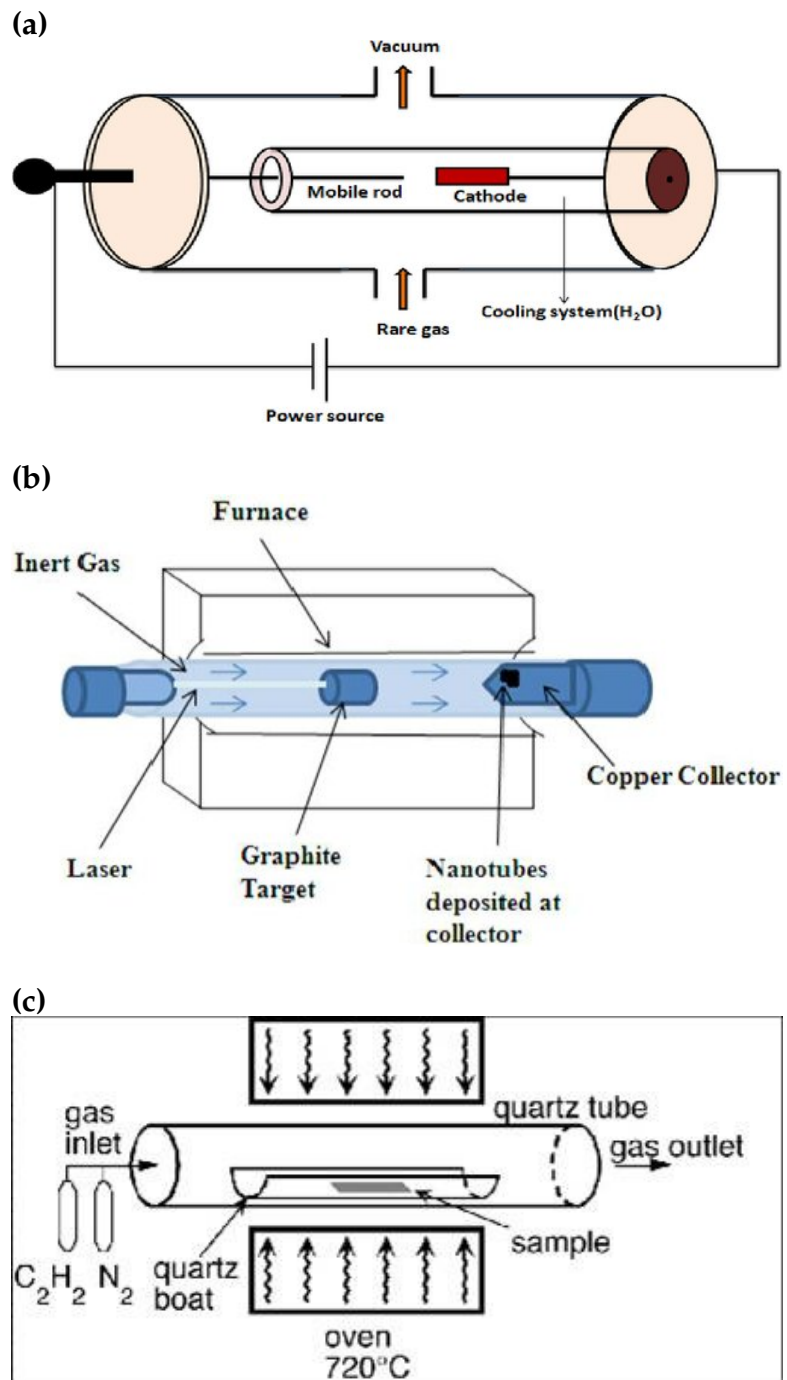


Figure 4.3: Synthesis methods of carbon nanotubes (a) Arc-discharge method [169], (b) Laser ablation[170], (c) CVD synthesis[171]

Methods	Progress	Consequence	
		Advantages	Disadvantages
Arc discharge	generated between two graphite rods under an inert atmosphere at different voltages, using a strong oxidizing agent instead of a metal catalyst and vacuum device	easy, defect-free CNTs, can easily produce SWCNTs and MWCNTs, high yield CNTs	short CNTs, random structures, and direction, needs purification
Laser ablation	graphite target is vaporized by laser irradiation under a flowing inert atmosphere and high temperature, laser pulses rather than electricity to generate carbon gas from which the CNTs form	high purity, defect free SWCNTs, good diameter control, relatively pure product	expensive, low scale production, short with random size and direction
CVD	decomposition of hydrocarbon gases in the presence of metal particles	high purity, simple, long CNTs,	limited control over the structure, defects

Table 4.2: CNTs synthesis methods and their efficiency (From [172])

Chemical vapor deposition (CVD) is the most frequently utilized and explored method for growing CNTs. The CVD method operates on the following principle: first, the carbon source gas enters the reaction chamber with the carrier gas at a temperature of 800-1000 °C, where they are decomposed to produce carbon atoms on a coated catalyst substrate at a high temperature, and finally, CNTs are generated (Figure 4.3c). Numerous metal catalysts (Fe, Ni, Cu, Cr) and carbon sources (methane, ethylene, ethanol, acetylene, benzene, and so on) can be used in this process. Carbon supply, carbon source gas flow, carrier gas flux, growth temperature, and catalyst concentration are the primary parameters of the CVD process. CNTs are grown directly on the substrate, and the equipment is simple, low-cost, and requires low-temperature ($T \sim 1100$ K) [174] (see Table 4.2).

Impurities embedded in CNTs have a large impact on their physical and chemical properties. Most of the CNT synthesis methods including, electrical arc discharge, laser vaporization, and CVD produce other carbonaceous particles in parallel with CNTs, such as amorphous carbon, fullerenes, nanocrystalline graphite, and metal particle resulting from catalyst decomposition[175].

The presence of multiple impurities in produced materials has limited the development of new applications. Different purification procedures lead to produce different types of CNTs. The type and amount of impurities depend on the synthesis processes, catalyst type, and carbon supply. Examples of chemical techniques include oxidation by heating, acids and oxidizing agents, and annealing in inert gases. These processes separate the various carbon and metallic particles depending on their reactivity with acid and oxygen. However, it introduces inevitable defects along the CNT that cause significant damage to the structure and hence significant modification of their electronic properties.

Ultrasonic, filtration, centrifugation, and size-exclusive chromatography are physical meth-

ods used to separate contaminants depending on their size. This procedure is more complicated and less successful. It is typically used to separate and remove aggregate, amorphous carbon, and nanocaps.

4.1.3 CNTs properties

CNTs have unique and outstanding mechanical, thermal, electrical, and optical properties. The excellent properties of CNTs are attributed to their unique structure and topological arrangement of carbon atoms[161]. The characteristics of CNTs are determined by the structure i.e., chirality, morphology, diameter, and length of the tubes.

4.1.3.1 Mechanical and Thermal properties

CNTs can have a high aspect ratio, are stronger than steel, and are more thermally conductive than copper[176]. They are mechanically the stiffest known materials, with an estimated strength of nearly 100 times that of steel at one-sixth the weight[177]. CNTs are thermally stable in vacuum up to 2800 °C and have a thermal conductivity approximately twice that of diamond[174]. Thermal conductivities of CNTs approach those of copper[178]. The addition of pristine or functionalized CNTs to various materials may increase their heat conductivity. The type of variables that impact the thermal properties of the CNT is the number of phonon active modes, the length of the phonon-free path, and the boundary scattering. These factors are also affected by the atomic arrangement, the tube diameter and length, the number of structural defects and morphology, and the presence of contaminants in the CNTs.

4.1.3.2 Electrical and optical properties

The carbon atoms in the CNTs are covalently connected to three neighbor carbons through sp_2 bonds organized as a hexagonal lattice. As a result, π electrons are delocalized over all atoms, contributing to the CNT's extraordinary electrical nature[179].

The electrical properties of CNTs are primarily influenced by geometric parameters such as defects, chirality, diameters, and the degree of crystallinities of the tubular structure[180]. Understanding the density of state (DOS) and band structure of CNTs is required to get a conclusive description of their electrical characteristics and to identify their potential applications. Using the zone folding approach, the optoelectronic characteristics of the SWCNT may be obtained from the corresponding 2D graphene sheet. This approach separates the electrical DOS by building cutting lines based on the geometrical structure of the CNT. Each of the cutting lines (except from the Dirac point (K) in the case of metallic CNT) causes a local maximum in the DOS, which is known as a 1D van Hove singularity (VHS) (Figure 4.4). These VHS can function as valence and conduction bands for electronic subbands. Because of the presence of the VHS in the DOS of the 1D structure, these structures behave somewhat differently from 2D graphene and 3D fullerene. The electrical band structure of SWCNTs depends on the chiral indices (n, m) of the tube. Depending on the configuration of the carbon atoms, CNTs can behave as metals or semiconductors[181, 182, 183]. Figure 4.4 illustrates the band structure (left) and DOS (right) of metallic and semiconducting SWCNTs, respectively. If $n - m = 3q$, where q is an integer, a SWCNT is metallic; otherwise, a

SWCNT is semiconducting[184].

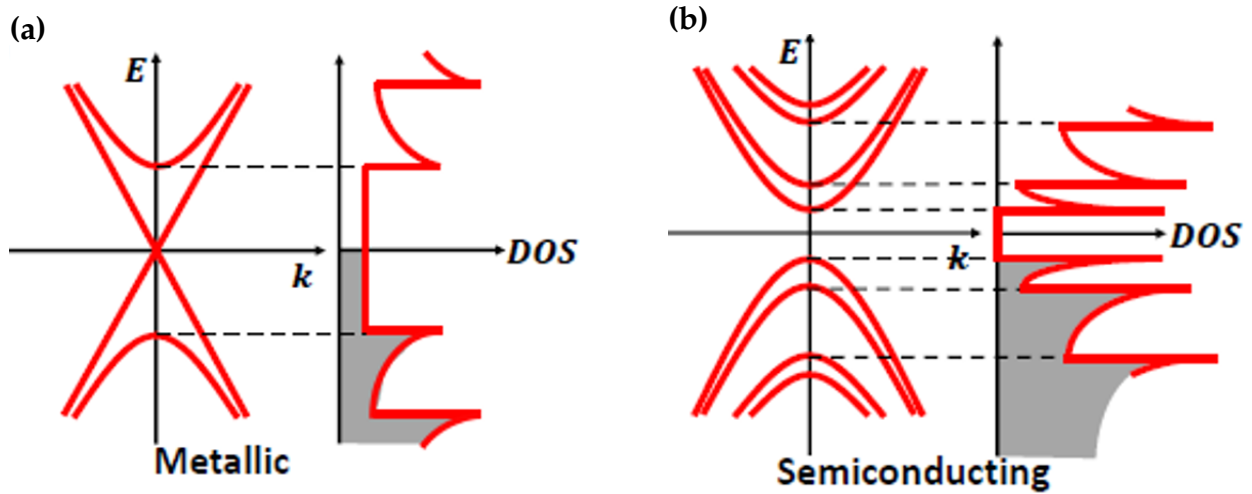


Figure 4.4: Band structure (left) and density of state (right) of CNT: a) metallic CNT, b) semi conducting CNT (From [185]).

All armchairs are metallic ($n = m \neq 0$), but zigzag nanotubes ($n, 0$) and chiral (n, m) can be metallic or semiconducting. It is well admitted that one-third of the CNTs are metallic, while the two other thirds are semi-conducting[186].

Armchair SWCNTs have a continuous DOS at the Fermi level; in other circumstances, metallic SWCNTs (m-SWCNTs) have a tiny pseudo-band gap that can typically be ignored at ambient temperature. Semiconducting SWCNTs (sc-SWCNTs) have a substantial band gap that decreases with diameter. The band gap of an SWCNT is described by the following relation. $E_{gap} = 2\gamma a_{CC}/d_t$, where γ is the carbon to carbon tight binding overlap energy (see Table 4.1 for element designations). The DOS at Fermi energy varies between metallic and semiconducting. At absolute zero temperature, the Fermi level is the maximum energy level that an electron may occupy. Because the electrons are all in the lowest energy state at absolute zero temperature, the Fermi level lies between the valence band and the conduction band. CNT optical transitions are transitions between VHS. The explained band structure is only relevant for isolated SWCNTs, however for nanotube bundles or MWCNTs, certain alterations might be necessary due to van der Waals intertube interactions. CNT in contact with substrate also exhibits alteration of their properties. The existence of VHS in CNTs' DOS has a significant influence on their physical characteristics, including electronic transport mechanisms, optical absorption, electron-phonon interaction, and so on. Because of the formation and recombination of electron-hole pairs or excitons, such a concentrated DOS causes substantial light absorption and emission. For example, when the excitation energy adheres to the VHS in the DOS in the valence and conduction bands, a considerable increase in optical absorption in the system can be observed[166].

CNTs are employed in transistors, sensors, and microelectronics due to all these remarkable electronic characteristics.

4.2 Manufacturing of a CNTFET

4.2.1 CNTFET fundamentals

Because of their unique electronic properties, CNTs can be used in different sensor applications. CNTs have been proposed as a potential material for future semiconductor devices thanks to their higher mobility, low defect structure, and intrinsic nanoscale size. Carbon nanotube-based field effect transistors (CNTFETs) minimize the transistors' dimensions and are more sensitive than silicon-based conventional field effect transistors (FETs).

4.2.1.1 Principle of FETs structure

The FET's working principle is based on the modulation of the channel conductivity by an applied external electric field, which controls the flow of charge carriers such as electrons or holes. Source, drain, gate, and channel are the main components of the FET (Figure 4.5). The source and drain are the electrodes on each side of the channel, while the gate electrode is separated from the channel by a thin dielectric layer, i.e. SiO_2 , Si_3N_4 , etc. Applying voltage to the gate electrode creates an external electric field that controls the charge flow between the source and drain electrodes.

The junction FET (JFET) and the metal oxide semiconductor FET (MOSFET) are the two main types of FETs. JFETs rely on a p-n junction to form a depletion zone that serves as the channel, whereas MOSFETs use a metal gate and a thin oxide layer. FETs have a high input impedance, a low noise level, and low power consumption. They are commonly employed in a wide range of applications such as amplifiers, oscillators, switches, and digital logic circuits.

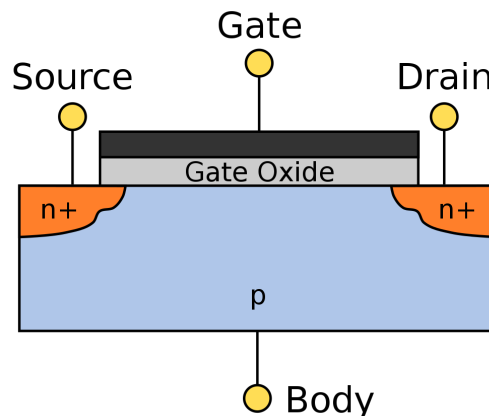


Figure 4.5: Schematic of FET (From [187]).

4.2.1.2 Electrical response of the CNTFET

A CNTFET is a FET that uses CNT as the channel material. CNTFETs provide unique properties that make them desirable for application in high-performance electronic devices. CNTFETs acquire attention in nanotechnology, in the actuation, sensing, and shrinking of electronics and optical devices as indicated in Moore's law.

A CNTFET's basic operation is identical to that of a regular FET. A CNT channel connects a source and a drain electrode, which is separated from a gate electrode by the solid-state insulating layer. CNTFETs are cutting-edge devices that are predicted to increase transistors' performance while maintaining their scalability. One of the primary distinctions between CNTFETs and MOSFETs is that in the CNT channel, it is possible to drive a higher current density due to the higher current carrier mobility compared to bulk silicon[188].

The first basic CNTFET was designed in 1998[189]. In this transistor, an individual sc-SWCNT connected the source and drain electrodes which are patterned on a silicon substrate and covered with a thick silicon oxide layer. It was observed that a gate voltage applied to the silicon back gate might be used to adjust the Schottky barrier between the SWCNT and metal electrodes, allowing the transistor current to be tuned.

There are two types of CNTFETs based on current injection methods: Schottky barrier CNTFETs (SB-CNTFETs), which employ metallic electrodes to generate Schottky contacts, and ohmic CNTFETs where the contact between the CNT channel and the source/drain electrodes forms an Ohmic contact (similar to the MOSFET).

Current transport in SB-CNTFETs is determined by electrons and holes displacement between potential barriers at the source and drain junctions. The gate voltage governs the barrier width, which in turn controls the current. The energy band diagram should be analyzed to better comprehend the SB-CNTFET. Schottky barriers form at the junction of the metal contacts and the sc-CNT. The Schottky barrier (SB) and work function of the metal used as source and drain contacts can be used to adjust the CNTFET's performance .

Three cases can be seen based on a comparison between the metal and the CNT work functions. First, if $\phi_m > \phi_{CNT}$, then CNTFET operates as a p-FET because the Fermi level of the source metal is close to the valence band of CNT. When a negative gate voltage is applied the valence band of the CNT aligns perfectly with the metal Fermi level. Then, by providing a negative drain voltage, a narrow SB is formed between the metal Fermi level and the valence band of the CNT, allowing holes to tunnel through it[190].

Second, if $\phi_m < \phi_{CNT}$, it works as an n-FET, with the conduction band of the CNT perfectly aligned with the metal Fermi level.

Third, if the metal's Fermi level precisely matches the Fermi level of the CNT, the device is ambipolar. Positive bias causes electrons to tunnel through the barrier, whereas negative bias causes holes to tunnel through the barrier. For short CNT transport becomes ballistic, limiting the current drive through the nanotube to the metal contact resistance and Schottky barriers at the source and drain ends. As a result, low contact resistance is preferred in SB-CNTFETs.

The source and drain electrodes of MOS-like CNTFETs are heavily doped semiconductors (p-type or n-type). These devices, also known as conventional CNTFETs, have the best "ON-OFF" current ratio. They also have various advantages such as unipolar properties, reduced leakage current in the OFF-state due to the removal of the Schottky barrier, improved scalability, and a larger source-channel junction switch-ON current. The potential barrier is generated in the channel's center, and the current is controlled by modulating the barrier height while adjusting the gate voltage.

Four types of CNTFETs can be categorized based on their design: back gate CNTFETs, top

gate CNTFETs, wrap-around gate CNTFETs, and suspended CNTFETs.

Because of the weak van der Waals connection of the devices to the metal electrodes of the back gate CNTFETs, this CNTFET type exhibits a high contact resistance (Figure 4.6a).

SWCNTs are placed on a silicon oxide substrate in the top gate CNTFET design. An atomic force or scanning electron microscope can be used to find and isolate each CNT. The source and drain contacts are then patterned using high-resolution electron-beam lithography. Lower contact resistance is achieved by high-temperature annealing that improves contact adhesion to the CNT. Following this, evaporation or atomic layer deposition is used to produce a thin dielectric layer on top of the nanotube. The top gate contact is then placed on the dielectric layer (Figure 4.6b).

Wrap-around gate CNTFETs have a better design than top-gate devices. The whole nanotube volume is gated in this configuration, whereas the top gate design simply gates the CNT closest to the metal gate contact. This advancement enhances the electrical performance of the CNTFET while decreasing leakage current (Figure 4.6c).

The suspended CNTFET design eliminates contact with the substrate oxide and thereby enhances the device performance (Figure 4.6d).

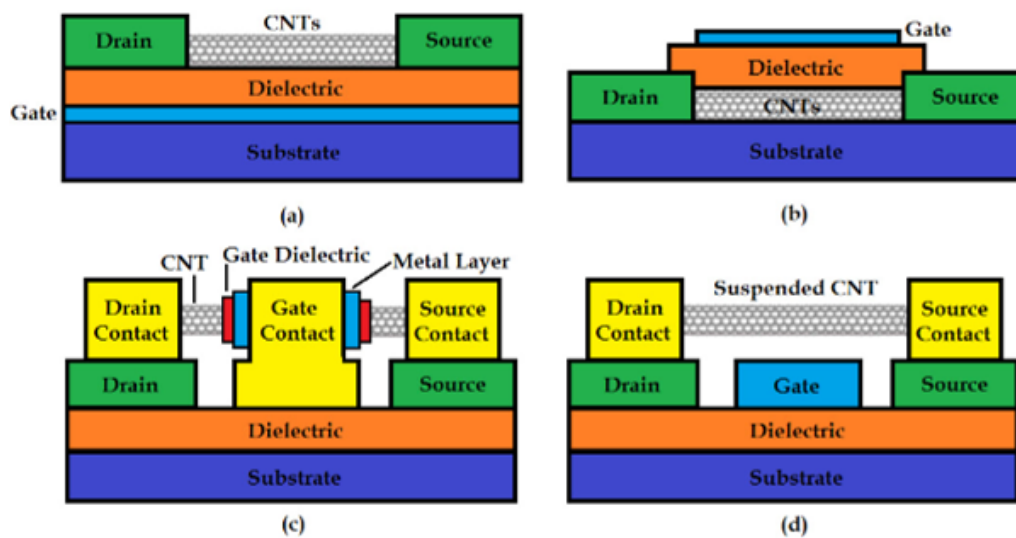


Figure 4.6: Type of CNTFET designs: a) back gate, b) top gate, c) wrap-around gate, and d) suspended CNTFET (From [191]).

To reduce the voltage necessary to generate the correct gate potential, the gate electrode should be composed of a material having a high dielectric constant. To reduce energy loss, the electrodes should be composed of a material with low contact resistance. The channel performance of the CNTFET is affected by the distance between the source and the drain. The gate electrode is shielded from the CNT using dielectric layers. The dielectric constant of the layer can influence the CNT's gate capacitance and threshold voltage.

The electrical characterization of CNTs is critical for determining their performance and suitability for any particular application. Thus, monitoring the source-drain current (I_{ds}) versus gate voltage (V_{gs}) and transconductance is included. Drain current against gate voltage dependency for several types of CNTs (semiconducting, metallic, or narrow band gap semiconducting) is illustrated in Figure 4.7. The $I_{ds} - V_{gs}$ dependency characteristic can

reveal information about the CNTFET's carrier mobility, threshold voltage, and saturation voltage. The change in current flowing through the CNT as a function of the gate voltage is measured as transconductance.

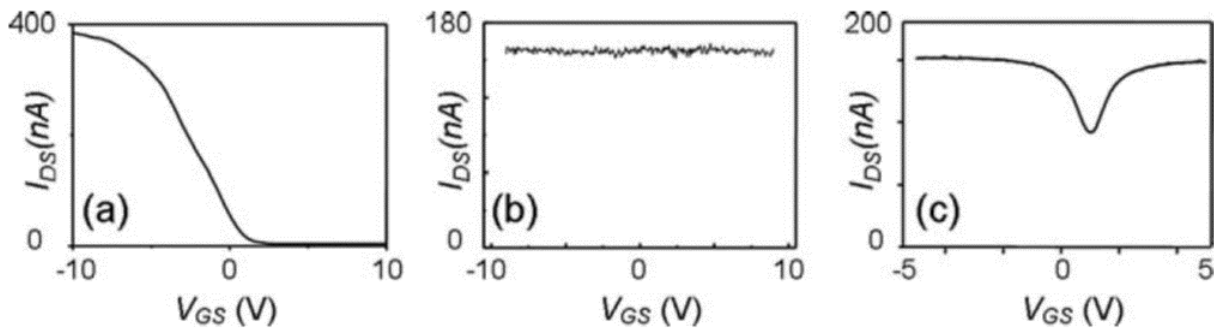


Figure 4.7: Drain current versus gate voltage dependency of (a) semiconducting, (b) metallic, and (c) semiconducting with a small bandgap SWCNT (From [192]).

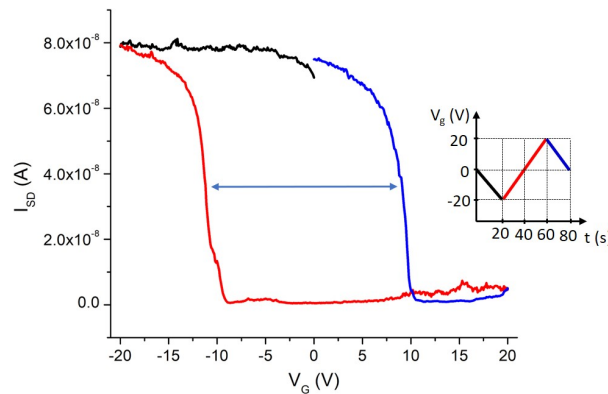


Figure 4.8: $I_{ds} - V_g$ curve of the sc-SWCNT measured with $V_{ds} = 10$ mV, the width of hysteresis is shown with blue arrow. Inset shows gate voltage sweeping direction

The impact of water on CNTFET has already been the subject of interest and it is well known that, charge trapping by water molecules around the CNT, including the SiO_2 dielectric surface, FETs exhibit hysteresis in the $I_{ds} - V_g$ plot[193] (Figure 4.8). Even though this process has not been studied in detail with identifying CNT such as SW, DW, MW, or even bundle and also if it is open or closed. It was reported that change has been observed in gate hysteresis during vacuum annealing of the CNTFET due to the desorption of the adsorbed water layer, which can be explained by a shift of the Fermi level alignment at the CNT/metal contact during the desorption process. However, water cannot entirely be desorbed due to charge traps on the surface of the SiO_2 dielectric layer[194]. Therefore, charge transfer through the CNT and charge traps at the silicon oxide in an ambient interface is the primary source of gate hysteresis in CNFETs on silicon oxide substrates. Hysteresis is associated with charge trapping (interface trapping, charge transfer to neighboring traps and adsorbates, and water ionization at the interface)[193]. Device characteristics (diameter, dielectric thickness, number of layers), environmental conditions (temperature and humidity), and measurement parameters (gate voltage sweeping rate, gate voltage interval, bias voltage) are used to

categorize hysteresis[195]. The decrease in sweeping rate caused a larger hysteresis, which can be explained by the fact that the trapping/detrapping process at the oxide surface is not instantaneous[193, 196]. This phenomenon was demonstrated using electrostatic force microscopy to look at charge injection at the CNT and SiO₂ contact[197].

Controllable hysteresis or hysteresis-free devices must be manufactured in order to use CNTFETs as memory elements or sensors[198]. Hysteresis-free devices can be achieved by the encapsulation of the CNT with a dielectric layer. Annealing under a vacuum is also beneficial in removing adsorbed water.

CNTFET performance optimization methods can be categorized as i) minimizing the resistance between CNT and metal, ii) enhancing the tuning efficiency of gate voltage to CNT channels, iii) reducing the CNT channel length[199].

One way for improving CNTFET performance is to reduce the contact resistance between the SWCNT and metal electrodes. CNT and metal interacted with weak van der Waals force, resulting in high contact resistance which degrades the device's performance. To overcome this drawback several approaches such as annealing or selecting better contact metals with higher work functions have been applied.

Another method to improve CNTFET performance is by increasing the tuning efficiency of the gate voltage. Top gate, back gate, and rolling gate are the three approaches to improve gate tuning efficiency. A thick gate insulator provides a high threshold voltage in the back gate design. Furthermore, when the device is exposed to air the gate capacitance is diluted by the air-low dielectric constant, resulting in poor tuning efficiency. The top gate structure improves gate bias tuning efficiency. The threshold voltage is reduced, and the device drives current and transconductance are enhanced.

Decreasing the distance between the gate electrode and SWCNT can increase gate capacitance and hence boost the gate electrode tuning effect. Adopting a gate insulator with a high dielectric constant (ϵ) can also improve device performance. For classic MOSFETs, the gate capacitance (C_g) and gate insulator thickness (t_{ox}) have a $C_g \sim t_{ox}$ relationship. For CNTFETs, it can be expressed as $C_g = 2\pi\epsilon\epsilon_0 / \ln(2h/r)$, where ϵ , h , and r are the dielectric constant, silicon dioxide thickness, and CNT radius, respectively.

Shortening the channel length is another technique to improve CNTFET's performance. When the SWCNT channel is long (more than a few micrometers), the carriers are reduced due to the structural defects and inhomogeneity of carrier mobility[200]. If the channel length is less than 500 nm, the carrier can perform a ballistic transport in the SWCNT. However, the conductivity enhancement is diminished when the length of the channel is less than the mean free path of carriers[201].

In summary, CNTFETs are a kind of FET that uses carbon nanotubes as the channel material. They offer special properties that make them attractive for high-performance electronic devices. CNTFETs have several advantages over traditional FETs, including larger current densities and faster switching rates. However, they have some drawbacks, including the presence of charge traps and Schottky barriers, which can limit their performance and reliability.

4.2.1.3 Charge traps, Silanol groups, and Schottky barrier

Charge traps can be caused by a variety of factors, including impurities in the nanotube material or defects introduced during the production process, which can create fluctuations in the transistor's electrical characteristics. Charge traps have the ability to collect and keep charge carriers (electrons or holes) for extended periods of time. This causes changes in the transistor's conductance since it impacts the channel conductance and modifies the device's threshold voltage. Charge trapping is classified into three types (surface trapping, interface trapping, and dielectric traps), all of which cause hysteresis. Surface traps occur on the device surface far from the CNT; interface traps occur between the CNT and the substrate; and dielectric traps appear inside the dielectric layer (Figure 4.9).

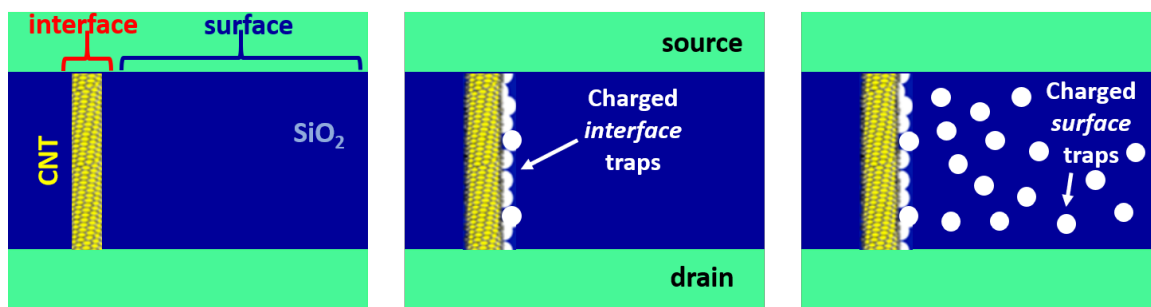


Figure 4.9: Charge traps in the CNTFETs (From [196]).

Chemisorbed water, physisorbed water, and silanol groups are the preliminary sources of surface traps. Two types of water charge traps were observed: The first includes weakly adsorbed water molecules on the CNT surface, which may be quickly removed by pumping under vacuum, as in the case of suspended tube devices. The second form of trapping includes surface-bound SiO_2 water near the CNT. The surface of thermally produced SiO_2 in ambient air is composed of silanol groups, i.e. $\text{Si}-\text{OH}$, that are hydrated by a network of water molecules. The monolayer or submonolayer of hydrogen-bound water adsorbed on SiO_2 cannot be totally removed by pumping under vacuum even for long periods of time at room temperature[193]. Sung et al. found that this second cause was the most significant. Indeed, after modeling the impact of hypothetical water-molecule doping on SWCNTs, they determined that the physisorption of water molecules on SWCNTs cannot account for the hysteresis in transfer characteristics[202]. Charge noise in suspended FETs was also discovered to be related to the insulating substrate and surface adsorbates[203]. Researchers are continuously investigating methods to reduce the impact of charge traps, such as utilizing chemical treatments or refining the production process.

Silanol groups are chemical functional groups that can be found around carbon nanotubes and are formed on the substrate surfaces. Silanol groups are formed by interactions with ambient moisture or chemical functionalization and consist of a silicon atom linked to a hydroxyl ($-\text{OH}$) group (Figure 4.10). The presence of silanol groups nearby the surface of CNTs can have a major impact on their characteristics, especially their electrical properties. In CNTFETs, for example, silanol groups can behave as charge traps. On the other hand, silanol groups formed on the substrate surface may also affect on the CNT proper-

ties. Silanol groups, for example, can be utilized to connect additional functional groups or molecules to the surface, allowing for the selective binding of biomolecules or the development of novel forms of nanocomposites. When the gate voltage is negative, silanol groups release protons and electrons. The lost proton may be trapped nearby, whereas the lost electron could be captured by nanotubes or electrodes. Because of the huge difference between the dielectric constant of water ($\epsilon \approx 80$) and silicon oxide ($\epsilon \approx 3.9$), the electrical field lines pass from the plane capacitor to the water layer. The strong electric field across the water layer causes protons to be desorbed and absorbed by terminal OH groups[204, 205].

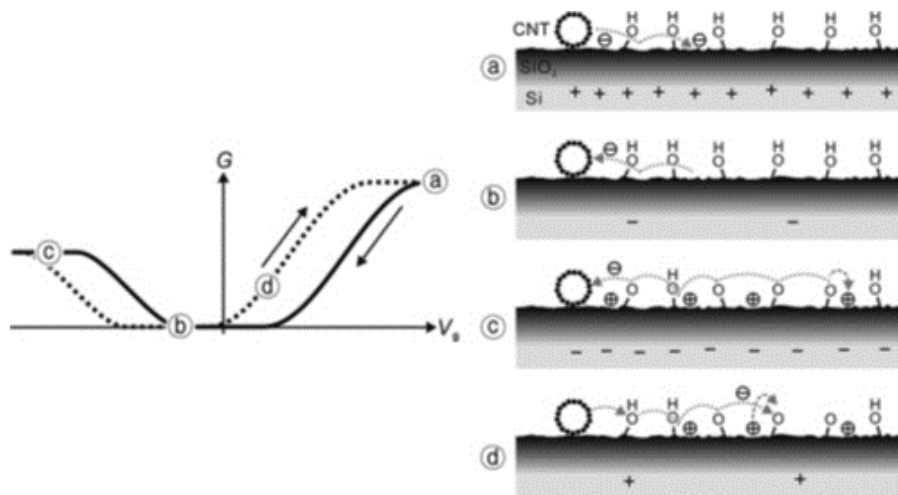


Figure 4.10: Hysteric surface charging process: a) start with positive gate sweep (V_{gs}), b) negative V_{gs} in the decreasing sweep, c) negative end of the decreasing sweep, and d) positive V_{gs} in the last increasing sweep. The circled plus marks represent protons released from the surface of silanol groups (From [194]).

The potential barrier that arises at the metal and CNT interface in a CNTFET is referred to as the Schottky barrier. The Schottky barrier is formed as a result of a difference in the work function of the metal and the CNT, which results in a potential energy difference between the two materials. Because it limits the passage of charge carriers through the CNT channel, this barrier has a substantial impact on the electrical characteristics of the CNTFET. The existence of the Schottky barrier in the CNTFET can result in non-linear current-voltage characteristics. Furthermore, the Schottky barrier increases the device's total resistance, limiting its overall performance. In gas sensing, the Schottky barrier at metal CNTs contact can be beneficial in determining whether the effect arises from the CNT or from the contacts[206, 207]. The alteration of the Schottky barrier can be detected from the transition between the n and p-type band based on the values of the applied gate voltage and bias voltage. This movement of the band ceases when the Fermi level reaches the valence or conduction bands. Researchers have investigated several strategies to reduce the impacts of the Schottky barrier, such as utilizing metal contacts with a lower work function or applying chemical treatments to change the CNT surface.

4.3 State of the Art about CNTFET behavior in interaction with water

Because of their reliability and outstanding sensitivity, CNTFETs have gained popularity as environmental sensors. In particular, the electrical sensitivity of these transistors can be seen as a novel technique for distinguishing the influence of water confined inside the CNT from water adsorbed at the external surface. Clarifying the effect of confined water while measuring the impact of water on CNTFET with sides open CNT should shed light on nanoscale confined water.

4.3.1 Possible mechanisms behind water effect on the CNTFET

CNTs are p-doped in the ambient condition because of the presence of oxygen molecules on their surfaces. Investigating the FET experimental $I_{ds} - V_{gs}$ behavior is a significant tool for understanding the impact of water interaction. Electrostatic gating, capacitive gate coupling, charge mobility changes, and the Schottky barrier effect were observed experimentally on sides close SWCNTs and simulated using molecular dynamic simulations as possible mechanisms behind the effect of charged species adsorption on CNT.

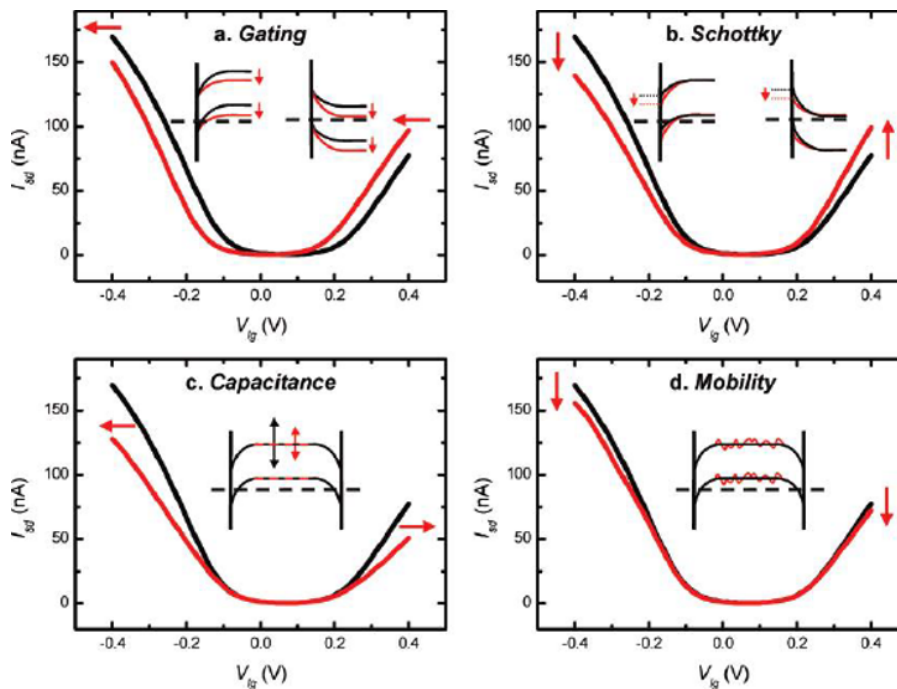


Figure 4.11: Sensing mechanism for calculated $I_{ds} - V_{gs}$ curve of CNT while species adsorption: a) Electrostatic gating effect. (b) Schottky barrier effect. In panels, a and b, the left and right insets illustrate the corresponding changes in the band diagrams for hole and electron doping respectively. (c) Capacitance mechanism. In panels c and d, the insets illustrate the corresponding changes in the band diagrams. (d) Mobility mechanism (From [208]).

Figure 4.11 depicts four different sensing mechanisms on the I_{ds} versus V_{gs} shape, black (before), and red (after) adsorption of species for a 10 mV source-drain voltage. Figure 4.11a illustrates the change in the $I_{ds} - V_{gs}$ curve caused by electrostatic gating by adsorbed

charged molecules, which produce doping in the SWCNT: the $I_{ds} - V_{gs}$ curve moves along the voltage axis. The Schottky barrier mechanism at the metal contact modulates the work function and hence the band alignment, as shown in Figure 4.11b. Because the Schottky barrier height varies in opposing directions for the hole (p) and electron (n) transport (see insets), the p- and n-branches of the $I_{ds} - V_g$ curves exhibit distinctive asymmetric conductance variations. Figure 4.11c shows the effect of decreased gate efficiency, which can occur when gate capacitance is lowered due to poor permittivity of adsorbed molecules in the CNT surrounding. Figure 4.11d depicts the effect of decreased carrier mobility on conductance in both the p- and n-branches. The insets in panels c and d show the relevant modifications in the band diagrams. Thus, it was determined that electrostatic gating and Schottky barrier effects dominate sensing, electrostatic gating being predominant[208]. When CNT is doped, a shift of the threshold voltage can be detected with no change in the slope. On the other hand, if the Schottky barrier height is varied at the metal/SWCNT contact, a quick change in the slope should be detected with no shift in the off-bias interval. Changes in CNTFET conductance resulting from doping or change in carrier mobility can be caused by the introduction of electrical defects due to the reorganization of the SWCNT network or charge carrier traps in both p- and n-channel operations[209, 210].

4.3.2 The effect of liquid or vapor water at the external surface of CNT

Several studies have been performed to investigate the effect of vapor and liquid water adsorption on the electrical response of closed carbon nanotubes.

While researching the effect of water partial pressure, i.e. humidity on the electrical characteristics of SWCNT-FETs, researchers discovered that water molecules act as electron donors to the nanotube. The adsorption of water molecules in p-type CNTFETs would compensate hole carriers, lowering conductance until the humidity level approaches 65%. Then, in the higher humidity values, conductance increases with humidity due to the compensation of electron carriers in CNTFETs[211].

The humidity sensitivity of suspended and non-suspended devices was compared. In comparison to non-suspended CNT, suspended devices that are made from thin film layers of SWCNTs demonstrated three times faster recovery time after desorption, negligible hysteresis, and better sensitivity[212].

Water molecules can form chemisorbed and physisorbed layers on the surface of the CNT. Chemisorption refers to the strong binding of molecules to a surface through chemical bonds. It was claimed that these bonds can lead to the dissociation of water molecules, resulting in the formation of hydroxyl groups on the CNT surface. Chemisorbed water is a combination of O_2 and H_2O which is important in the doping process, and the electrochemical redox reaction in alkaline is depicted as[213, 214, 215]: $O_2 + 2H_2O + 4e^- \leftrightarrow 4OH^-$. This is the most important cause of hysteresis.

Water molecules physisorbed onto the individual semiconducting close SWCNT surface are proposed to exist alongside chemisorbed water involving the non-covalent interaction between water molecules and the CNT surface. Physisorbed water may be removed from the material by pumping at ambient temperature for a short period of time, whereas water chemisorbed on silanol groups can only be removed by vacuum annealing at temperatures over 200°C[193].

A theoretical study on water adsorbed at the outside surface of CNT showed that the charge transfer between water and CNT is insignificant. It was then proposed that the effect of humidity on nanotube devices may be attributable to a variety of indirect processes such as charge trapping forming silanol groups which are assisted by adsorbed water, rather than to be due to physisorbed H₂O molecules[202].

However, another, MD simulation study about water adsorption on the open-ended SWCNT surface was found to decrease electrical conduction[216] as well as mobility and threshold voltage. This effect was supposed to be due to gate capacitance change because of water or charge transfer between CNT and water[217, 218].

The adsorption of water partial pressure has been shown to alter the CNTFETs' threshold voltages and its current at OFF-state which is made of CVD-grown SWCNTs[219]. Two mechanisms were proposed in this measurement: reorientation of weakly adsorbed water molecules around the carbon nanotube and charge traps forming silanol groups on the surface of silicon dioxide.

In the SWCNT network, charge traps caused by water adsorption on the SWCNT surface and on gate insulator oxide were measured[220]. At negative gate voltages, holes accumulate in the CNTs, lowering the depletion barrier and boosting the source-drain current (I_{sd}) through the channel. At positive gate voltages, the channel resistance increases owing to hole depletion, and hence I_{sd} drops. At zero gate voltage, the electrons that were provided by the water molecules resulted in a reduction in current. In this case, the electron-donating nature of water molecules to SWCNTs is assumed to explain the rise in current at positive gate voltages and the decrease in current at negative gate voltages.

Transistors were fabricated from an aligned thin layer of CNT networks cycled under water. Those enriched with sc-SWCNTs were more sensitive to analytes than those made using random, unsorted networks dominated by m-SWCNTs. They proposed that this discrepancy might be due to a lower density of states around the Fermi level in metallic tubes compared to the valence band edge of sc-SWCNTs[221]. This finding leads to propose of a mechanism behind interactions between carbon nanotubes and analytes that include either weak dipole interactions or greater charge transfer through $\pi - \pi$ bonding stacking.

The devices investigated by Foudeh et al. demonstrate modest device-to-device variance as well as strong current production at low voltages ($V_{sd}=0.5$ V), making them suitable for most physiological liquids[209]. When a network of SWCNTs' electronic properties is directly impacted by water, a significant difference from optimal properties is also found. Which can be linked to strong interactions between water molecules and sp₂-hybridized carbon structures[209].

As water molecules adsorbed outside of the CNT are randomly oriented, the interactions between them and the CNT's outer surface are less. Liquid water wetting the exterior of SWCNT-FETs increases their hysteresis and shifts their threshold gate voltage (V_{th}) [222]. Their observation was similar to previously reported work about water external wetness of CNT[216, 211]. When a p-type SWCNT-FET is externally wetted (while keeping the electrodes covered), the threshold shifts toward greater negative gate voltage, and hysteresis increases.

Thus, it was mainly reported that the effect of air partial pressure and liquid water adsorbed outside of the SWCNT network[220, 209, 219] or individual SWCNT[193] shifts its threshold voltage and changes hysteresis because of charge trapping on the substrate surface.

4.3.3 The effect of confined water

Contrary to common belief, the hydrophobic interior of SWCNTs is easily wetted since water's surface tension is significantly lower than the threshold wetting value of CNT which is reported with upper limit as $\gamma = 200\text{mN/m}$ [223]. Water has a lower chemical potential within the SWCNT than in the bulk, and water was shown to be transported at a speed of 2 or 3 orders of magnitude higher than the traditional Hagen Poiseuille flow[70, 68, 21].

When confined to small volumes or surfaces the behavior of water molecules is still not yet fully understood. Water molecules may easily rotate in bulk 3D environments. However, their rotational degree of freedom is diminished when they are confined in a small volume or adsorbed at the surface. This results in a significant decrease of water permittivity to about $\epsilon = 2$.

As far as CNTFETs are concerned, current, threshold voltage, and mobility can all be altered when CNTs' external wall is exposed to pure water aqueous electrolytes[209].

Cao et al. reported that filling the interior of the SWCNT with water activates the transistor but wetting the outside surface has minimal impact[224]. Confined water modifies the internal electric field of CNT, leading to charge polarization of the tube and metal electrodes, and to modification of the valence band as was shown from theoretical calculations[224]. Contrary to external wetting, it was found that internal wetting causes a shift of the threshold voltage to more positive gate voltage and a reduction of the hysteresis[224].

When electrolytes are confined, the properties of sc-SWCNT FETs were claimed to be sensitive to the concentration, pH, and ion nature[225]. It is also mentioned that such sensitivity was not detected when liquid water was wetting on the exterior surface.

Thus, the effect of water adsorbed inside is mysterious and requires more work to be understood completely.

4.4 Conclusion

CNTs are regarded as one of the best materials for water confinement due to their high aspect ratio and unique physical properties. Because of the CNTFET's remarkable electrical sensitivity, further research on the effect of water adsorbed outside and water confined inside appears to be needed. As discussed here above, several studies have been carried out to learn about the impact of water adsorbed outside of the CNT, but only a few studies have been achieved so far on the effect of water confined inside the CNT using CNTFET electrical sensitivity.

The key point is to be able to have a CNTFET made with a single SWCNT since, given the predominant effect of the tube diameter on the effects induced by the adsorption or confinement of water, a FET made up of a channel containing several SWCNTs, whose diameters and electrical properties may be different, cannot constitute a reliable object of study.

This is exactly what we propose to do. It was therefore the main purpose of our study to focus on CNTFETs consisting of an individual SWCNT. This work is detailed in Chapter 6.

Part II

Experimental work

SU-8 based high liquid water pressure tight, vacuum compatible, long-term stable sealing technology

As recalled in Chapter 3, sealing is one of the inevitable processes in micro and nanofluidic chip fabrication. Despite several decades of development, microfluidics lacks a sealing material that can be readily fabricated, leak-tight under high liquid water pressure, stable over a long time, and vacuum compatible as discussed extensively in Chapter 3. Various methods are used in microfluidics such as adhesive bonding[226], plasma bonding[227], thermal fusion[228], and anodic bonding[229], in order to seal conformal materials like PDMS, non-conformal materials like plastics, or hard surfaces (e.g. glass, silicon wafers). Most of the sealing materials and methods typically require at least one of the following conditions: activation of the extremely clean surfaces, and surface chemistry[230, 157].

Additionally, microfluidics is gaining popularity for highly sensitive mass measurements in liquid environments to weigh biomolecules, single cells, etc. In this measurement, experiments are carried out in a vacuum with microfluidic nanomechanical resonators[76, 77]. It is therefore desirable for the sealing material to be compatible with the vacuum.

So far, PDMS has been the most common material in chip sealing. However, this material has many drawbacks such as the adsorption of hydrophobic molecules, poor stability after surface treatment, swelling by organic solvents, vapor water permeability, and breaking under high-pressure operations[231, 232]. Moreover, sealing with PDMS requires activating at least one of the surfaces, typically using O₂ plasma which can damage the surface to be sealed.

Photoresist as SU-8 is expected to be better than the current PDMS technology. Interestingly, SU-8 being photosensitive allows forming of patterns by photolithography with micrometric dimensions. SU-8 is also used as both a structural material and an intermediate layer for adhesive bonding[233], exhibiting excellent physical and optical properties, good chemical stability, and low porosity[127]. It is suitable for sealing devices at low temperatures[115].

In this chapter, we will present an easy and permanent microscale processable sealing material with superior performance to PDMS. It is based on the use of SU-8 resin and only

requires the most basic clean room facilities. Since our goal is to develop the sealing process of microchips, our investigation focuses on the search for the thinnest possible wall of SU-8 that can exhibit high-pressure tightness, vacuum compatibility, and no liquid water porosity over a long time. The latter criterion is checked using an original and very sensitive method based on ionic conduction measurements as discussed in section 5.3. The sealing method investigated here is reliable, and versatile and does not require the use of aggressive treatments (chemicals, high temperatures, or high-energy plasma). We observed that micrometric walls made of SU-8 photoresist, whose thickness can be as low as $35\ \mu\text{m}$, exhibit water pressure leak-tightness from 1.5 bar up to 5.5 bar, no water porosity even after 2 months of aging, and are able to sustain under vacuum even lower than 10^{-5} mbar. It thus opens a new perspective to seal microchips where delicate surfaces such as nanomaterials are present.

5.1 Device fabrication/ assembling

5.1.1 Cleanroom fabrication

SU-8 patterning is performed in a cleanroom using photolithography as shown in Figure 5.1. Because of its improved adhesion and reduced coating stress (as specified by the manufacturer i.e., Kayaku - MicroChem®), we employed the SU-8-30xx series instead of the more widely used SU-8-20xx. More specifically, we worked with SU-8 3025 which has a viscosity of $4400\ \text{cSt}$, and a density of $1.143\ \text{g/ml}$. Optimal adhesion to the substrate is obtained using Omnicoat (Kayaku - MicroChem®) as a primer.

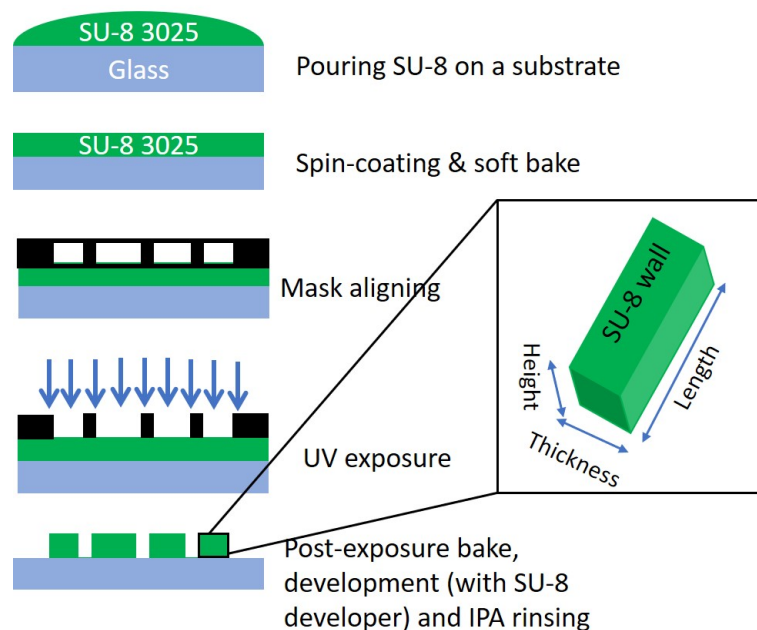


Figure 5.1: Schematic presentation of the SU-8 photolithography process. Inset illustrates SU-8 wall geometry adopted in this chapter.

A 4 mm thick glass substrate is used to support SU-8 patterns. First, it is milled to allow the

subsequent placement of capillaries of 1.6 mm diameter for the fluidic connection (Figure 5.6). In the case of ionic conductivity measurements (section 5.3), two holes are additionally drilled to insert Ag/AgCl electrodes (Figure 5.9). Surface cleanliness of the glass substrate is ensured by Piranha cleaning (3:1 ratio H₂SO₄: H₂O₂) followed by de-ionized water rinsing. Then, Omnicoat primer is spin-coated in 2 steps: first at 500 rpm for 5 s and then at 3000 rpm for 30 s. The substrate with Omnicoat is then baked at 200 °C for 2.5 minutes. The substrate is cooled down just below the glass transition temperature of the uncross-linked SU-8 and a few milliliters of SU-8 are poured all over the substrate. This temperature is recommended in order to remove bubbles[234]. Once the reaction between the Omnicoat primer and the SU-8 is complete, the substrate is cooled down to room temperature and spin-coated in 2 steps: first at 500 rpm for 5 s and then at 2000 rpm for 30 s. The SU-8 coated substrate is then baked at 100 °C for 35 minutes and slowly cooled down to room temperature.

The coating is exposed for 45 s to 365 nm UV photolithography, with a power density of 5.8 mW cm⁻² through a photolithography mask. A post-exposure baking treatment is applied at two different temperatures, i.e., 70 °C during 2.5 min and 100 °C during 6.5 min, followed by a slow cooling down to room temperature. Finally, the pattern of SU-8 is developed for 15 minutes in SU-8 Developer (Kayaku - MicroChem®) and rinsed with isopropanol. The height of the so-obtained SU-8 pattern is 35 μm.

Edge bead is an unavoidable effect of the spin coating process of the photoresist, as shown in Figure 5.2a. This effect is critical for viscous materials such as SU-8, and on wafers with a rectangle shape, yielding large inhomogeneity of the photoresist height on the surface. It has consequences such as the mask sticking with the wafer, which creates a gap between the mask and the wafer during the photolithography exposure process, and finally determines the homogeneity of the sealing.

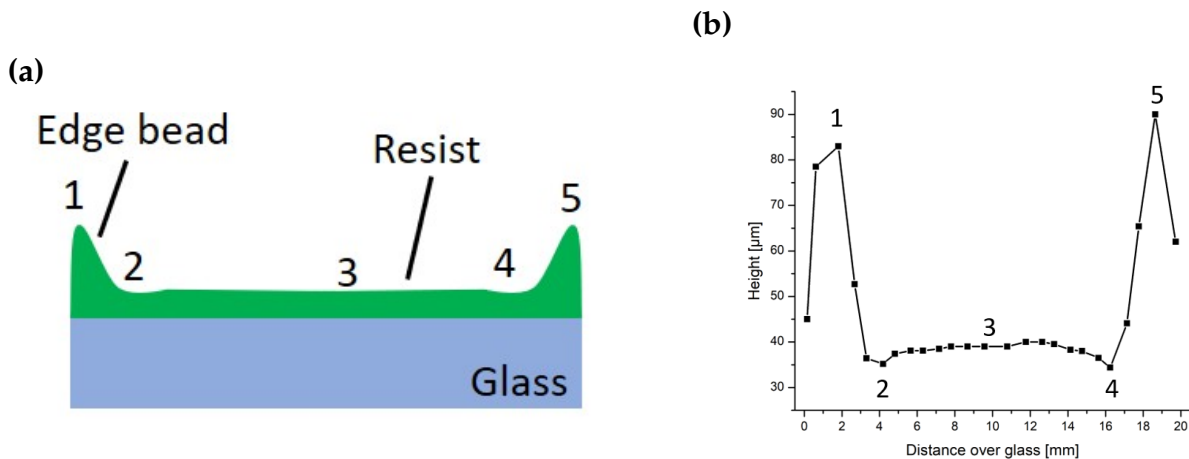


Figure 5.2: SU-8 photoresist homogeneity: (a) Shape of the photoresist after spin coating (b) SU-8 patterns homogeneity over the glass surface

Figure 5.2b presents the height distribution of the fabricated SU-8 pattern all over the glass wafer surface (20 mm). We observed that the resist layer becomes homogenous after ~ 5 mm from the edges (within ±10 %). One may note that the height of the pattern on the edge can be twice as high as the center (comparison of points "1" and "5" with the rest in Figure 5.2a). Thus, SU-8 patterns should be fabricated 5 mm in distance from the edge.

In addition, increasing the prebake time to 35 min was found to be essential to tackle the mask sticking problem.

The SU-8 wall height on points "2" and "4" are different (within $\pm 5\%$) from the center (marked as "3") in Figure 5.2a.

5.1.2 Device assembling

The SU-8 pattern on the glass substrate is bonded on a Si/SiO₂ wafer to form the reservoirs to be tested. To this aim, 2 mm thick brass rectangular frames are placed on either side and maintained with 4 screws (Figure 5.6b).

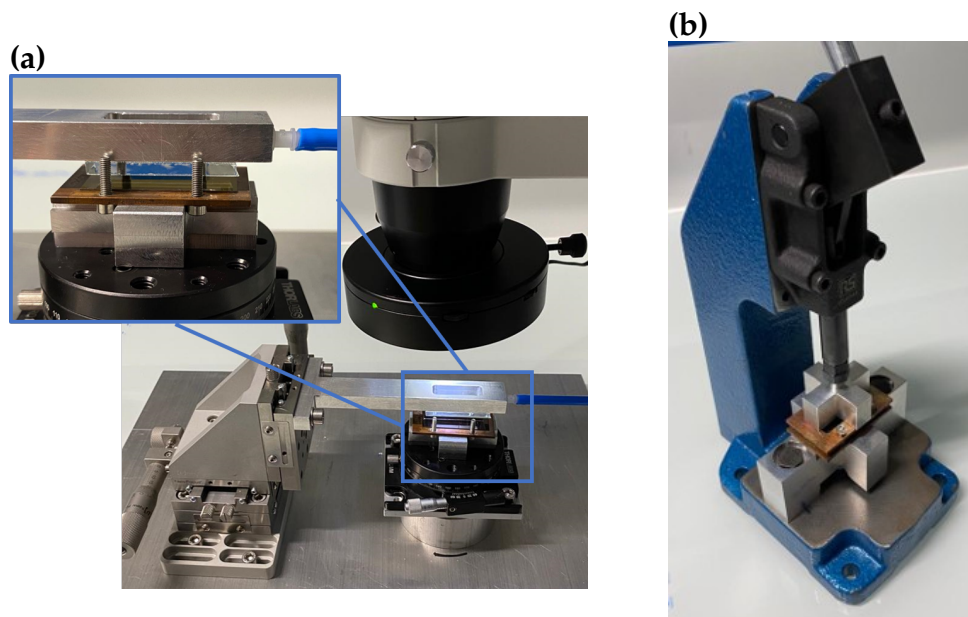


Figure 5.3: SU-8 assembling tools: (a) Alignment tool. (b) Homogenous pressing tool

The full process is the following: first, the SU-8 patterned glass substrate is aligned with the wafer using homemade alignment tool (10 μm resolution in x, y, z alignment on the glass side and 5 degrees precision rotation on the wafer side) (Figure 6.7a). Later the top frame is added and a pressing tool is used to complete the assembling by adding bolts (Figure 6.7b). This tool helps to keep frames parallel to each other while adding the bolts. The parallelism of the assembling of the SU-8 pattern is assessed by observing optically the device (Figure 5.4) while screwing the bolts. This crucial step is strictly controlled to obtain homogeneity by observing interferences/reflectivity with an optical microscope, in order to ensure the adhesion of the SU-8 wall on both the glass substrate and the wafer and to avoid any deformation of the pattern. Figure 5.4 shows the visual observation of the bonding area of the sealing material during sample assembling. Figure 5.4a shows sealing material directly after adding the frames and bolts. Later, bolts are screwed to apply an additional force in order to increase the bonding area, yielding the situation depicted in Figure 5.4b. While under-pressing can result in an unbonded area, over-pressing can crush of the SU-8 patterns (Figure 5.5a).

Finally, the sample is cured at 200 °C for 2 hours, exhibiting an increased bonding area (Figure 5.4c). It allows us to obtain surfaces that are completely in contact with the SU-8 pattern on centimetric distance. Noteworthy, during this baking step the thickness of the SU-8 layer extends from its fabrication thickness from 20 μm to 35 μm, 30 μm to 50 μm, 60 μm to 85 μm, and 100 μm to 135 μm.

After sealing the device, a capillary is inserted into the milling area of the glass substrate and sealed with Stycast 2850FT epoxy glue. The device is left at 65 °C for 2 hours in order to let the Stycast ensure efficient sealing. The performance of the Stycast sealing is verified on a device without SU-8: it showed high liquid water pressure tightness above 8 bars (the limit of our testing set-up) and even Helium leak tightness.

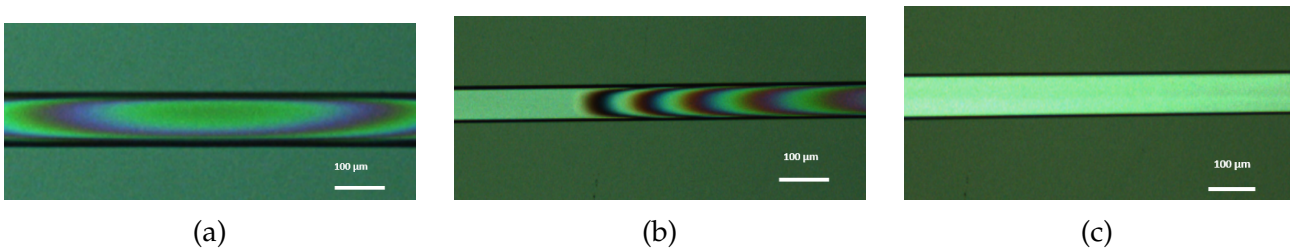


Figure 5.4: Sample assembling with the optical observation of the bonding area. (a) SU-8 pattern after assembling, (b) after adding bolts and screwing, and (c) SU-8 pattern after curing the sample at 200 °C.

The main factor limiting us from testing smaller wall thickness was the rolling of the SU-8 during the assembling process, as presented in Figure 5.5b for 10 μm SU-8 wall thickness. Thus, the minimum thickness of the SU-8 pattern that we got after assembling where 35 μm, corresponding to 20 μm lithography pattern.

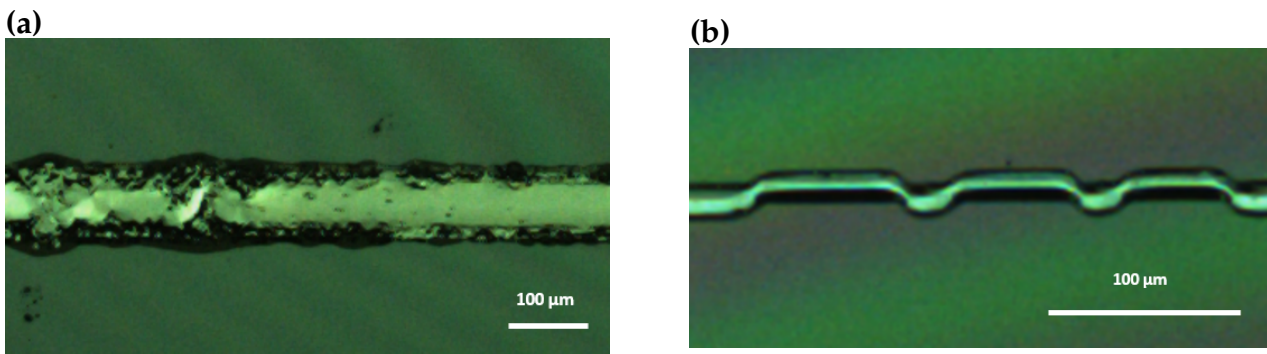


Figure 5.5: SU-8 assembling challenges: (a) Over pressing during screwing leads to crushing the SU-8 wall. (b) Smaller thickness SU-8 wall assembling leads to rolling

5.2 Liquid water pressure tightness test

5.2.1 Measurement set-up

Water pressure leak-tightness is measured thanks to the so-called burst pressure method. A schematic of the setup is shown in Figure 5.6a. At each pressure point, the presence of a leak

is visually assessed with an optical microscope: a change in the contrast/reflectivity indicates the presence of water outside the SU-8 reservoir as shown in Figure 5.7. This reservoir is filled with water at a pressure piloted by an Elveflow® OB1 MK3+ pressure controller. We tested SU-8 wall thicknesses ranging from 135 μm down to 35 μm . The given two boundary dimensions are set by our method of the chip assembly: 135 μm is the maximum compressible structure (given the large area of our device) that can be assembled, while 35 μm is the minimum structure below which the SU-8 rolls during assembly, as detailed in the section 5.1.2.

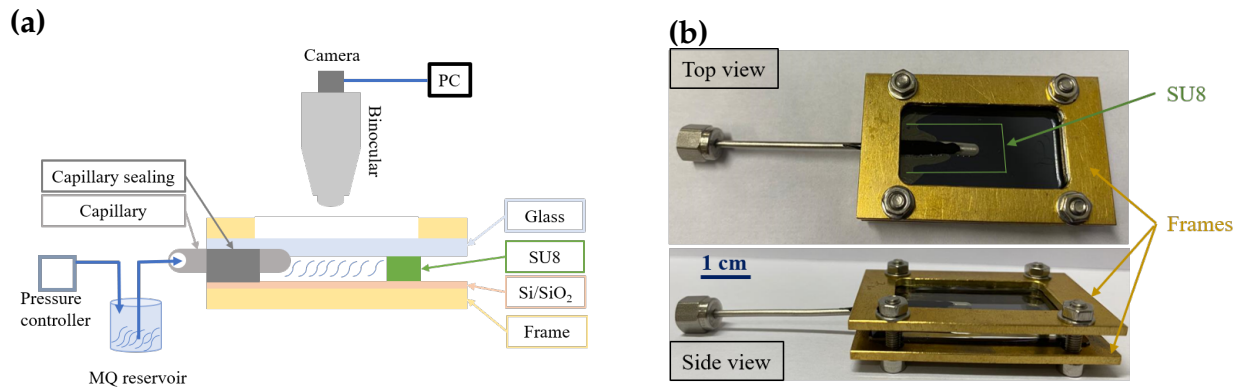


Figure 5.6: Liquid water pressure leak-tightness measurement setup. (a) Schematic of the setup. A pressure controller allows applying water pressure to the SU-8 reservoir. A binocular microscope is used for visual observation of the material's performance. (b) Photography of the sample with frames added to improve bonding of the material, and capillary for fluidic connection to the pressure controller.

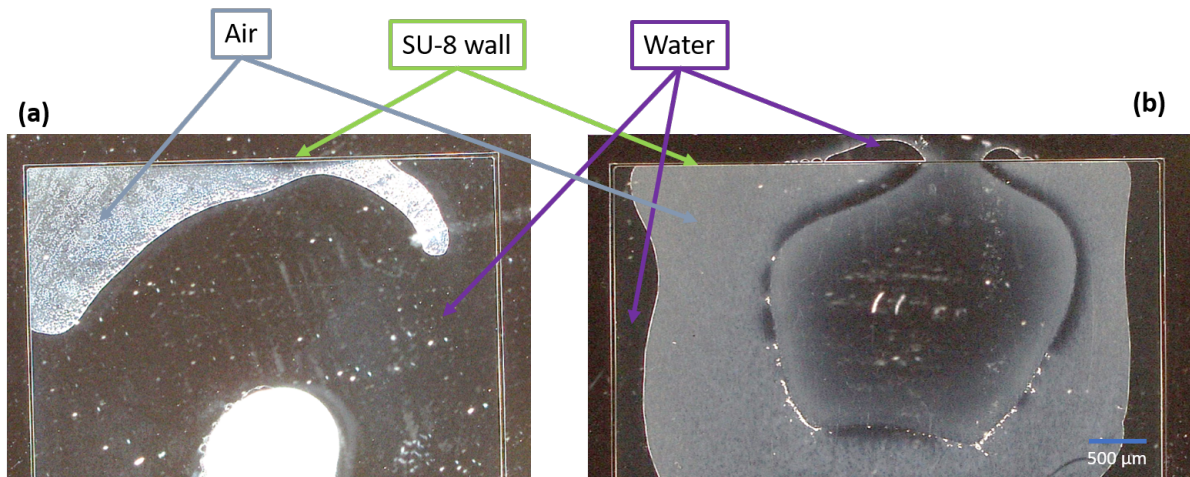


Figure 5.7: Optical observation of the SU-8 wall liquid water pressure leak tightness: a) liquid water pressure leak-tight SU-8 reservoir, b) leaky SU-8 reservoir.

Figure 5.7 illustrates the optical assessment of the burst pressure. In Figure 5.7a is shown a 2 bar liquid water pressure leak-tight reservoir. The SU-8 wall thickness is 45 μm . One can distinguish the presence of water in the reservoir as well as air bubbles. In Figure 5.7b is reported the case where the same reservoir is now leaking for an applied pressure of 3 bars.

5.2.2 Burst pressure tightness & dependence on device thickness

Bonding strength measurements are mainly based on three methods: tensile strength[235], burst pressure[236], and liquid leakage[237]. Among these methods, the most practical one to assess both the functionality of a microfluidic chip and the strength of the bonding is the burst pressure test.

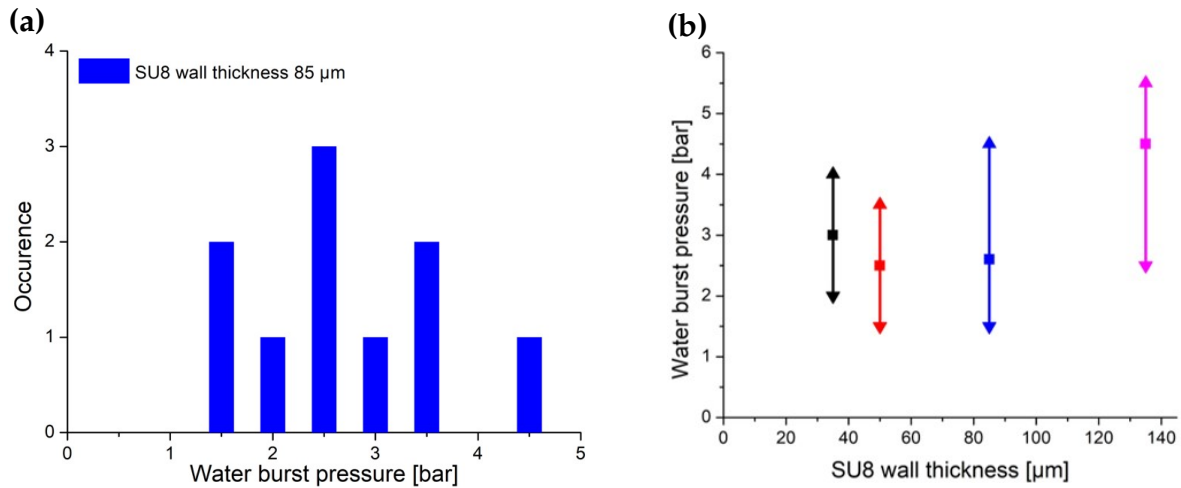


Figure 5.8: Liquid water burst pressure leak-tightness: (a) Liquid water burst pressure distribution for 10 devices with 85 μm thick SU-8 wall; (b) Liquid water burst pressure distribution of SU-8 walls with various thicknesses. The observed minimum, mean, and maximum burst pressures from several devices for each thickness is presented.

The burst pressure distribution measured for ten devices with 85 μm thick SU-8 walls is plotted in Figure 5.8a. The device's performance was measured for each applied pressure over 1 hour. In Figure 5.8b, we report the burst pressure distribution obtained for various values of SU-8 wall thickness. The symbols represent the mean, maximum, and minimum values of the burst pressure for each corresponding SU-8 wall thickness. One of the main outcomes is that the water pressure tightness does not depend on the SU-8 wall thickness: the absence of a trend of leak-tightness versus width (Figure 5.8b) is an indication that the resistance to pressure is more governed by random imperfections of the surface and dust rather than porosities. Another interesting feature of our SU-8 devices is that they can sustain pressures ranges from 1.5 bar up to 5.5 bar, which is significantly better than most of the other sealing materials reported so far with a maximum pressure of about [50-500] mbar[238, 239]. The defects during sample assembling might also explain the scattering observed in Figure 5.8a.

5.3 SU-8 porosity test using conductivity measurement

5.3.1 Measurement set-up

To test the liquid porosity of the SU-8 wall, we propose an original and extremely sensitive method based on the measurement of ionic conduction between two reservoirs filled with

an electrolyte and separated by a SU-8 wall. Indeed, it can be assumed that if the wall exhibits percolating paths through the entire thickness then an ionic current will be observed between both reservoirs. Knowing that ionic currents as low as pA were reported from extremely small porosities such as carbon nanotubes (~ 1 nm)[240], it can be assumed that in our case nanoporosity can be detected if a similar ionic current measurement method is used.

For that purpose, patterns of SU-8 walls were designed with 2 reservoirs on the glass substrate and assembled with an electrically insulating piece of quartz in order to lower the ionic noise[241]. The ionic current is measured via 2 Ag/AgCl electrodes placed in each micro reservoir and tightly sealed with Stycast glue in order to avoid electrolyte leak (Figure 5.9). Finally, the electrodes are connected to a high-impedance source-amplifier (Keithley 2636B), which enables both biasing the electrodes and measuring currents in the pA range.

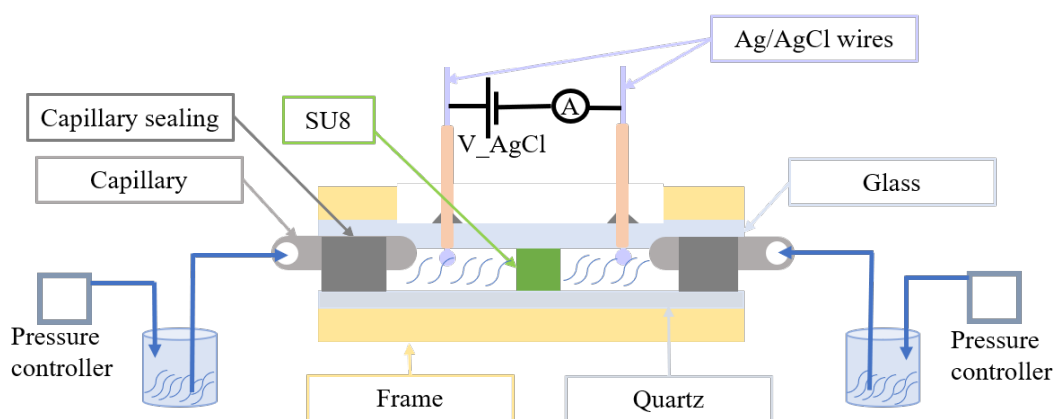


Figure 5.9: Schematic of the setup designed to measure the ionic conductivity between 2 micro-reservoirs filled with Milli-Q water or KCl electrolyte and separated by a SU-8 wall.

5.3.2 Conductivity: salt concentration & thickness dependence

First, blank measurement is carried out when both reservoirs are filled with Milli-Q water[®] whose resistivity is very high, about $18 \text{ M}\Omega \text{ cm}^{-1}$. Then, reservoirs are filled with KCl electrolytes at concentrations ranging from 10^{-4} to 1 M. The resistance, R of the SU-8 wall is readily determined from the current/voltage plot which follows Ohm's law, as can be seen in Figure 5.10a. Then the conductivity σ of the wall is calculated using the following equation:

$$\sigma = \frac{t}{Rlh} \quad (5.1)$$

where t , l , and h are the thickness, length, and height of the SU-8 wall after baking respectively. The ionic conductivity of our set-up filled with Milli-Q water is found to be about $1 \mu\text{S}^{-1} \text{ cm}^{-1}$ and seems independent of the SU-8 wall thickness (Figure 5.10b). It can thus be assumed that this background current originates from electrical leakage through the substrate and from the measurement set-up, but not from the wall thickness.

The dependence of the ionic conductivity with the ionic concentration in the log-log scale is reported in Figure 5.10b. We observe that the conductance does not follow the Kohlrausch's

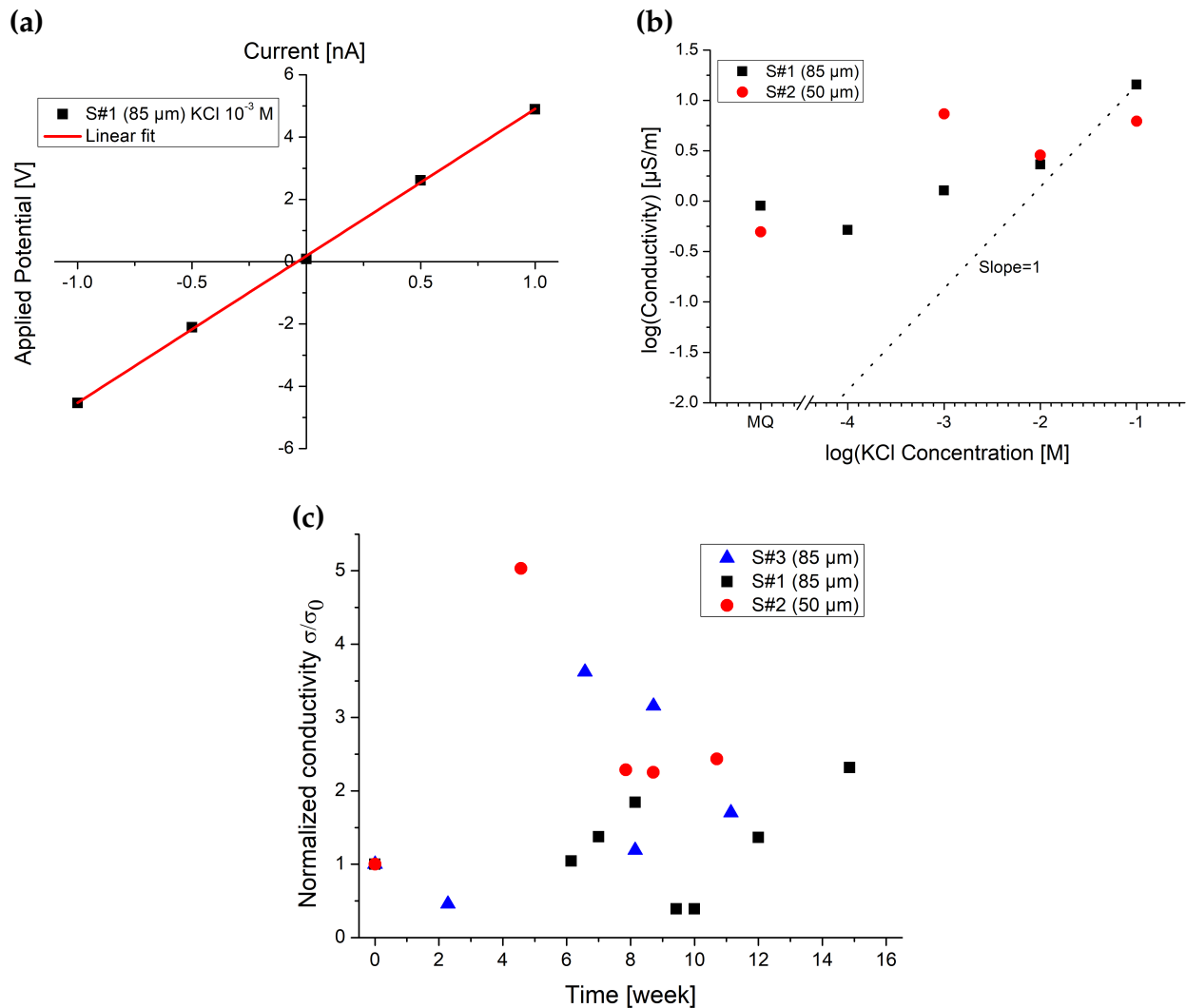


Figure 5.10: Ionic conductivity measurement between two micro-reservoirs filled with 300 mbar of either Milli-Q water or KCl electrolyte and separated by a SU-8 wall. (a) Typical example of current/voltage plot obtained with a KCl 10^{-3} M electrolyte and a SU-8 wall of w, l, h equal to 85 $\mu\text{m}, 10800 \mu\text{m}, 29 \mu\text{m}$. (b) Log-log plot of the ionic conductivity versus KCl concentration for two SU-8 walls with different thicknesses. The dash line with a slope equal to 1 represents the behavior expected for bulk ionic conductivity, i.e., Kohlrausch's law (Equation 5.2). (c) Conductivity normalized by its initial value as a function of time for SU-8 walls of 3 different thicknesses (KCl concentration of 0.1 M).

law for bulk conductivity of diluted electrolytes, i.e.,

$$\sigma = \sum_i \lambda_i C_i \quad (5.2)$$

where λ_i and C_i are the molar conductivity and the concentration of the solvated ion i respectively. Indeed, the log-log dependence would match with a straight line of slope 1 if Kohlrausch's law was obeyed. Instead, the evolution observed here for the device (see Table 5.1 for device dimension) S#1 ($t=85 \mu\text{m}$) is similar to the usual behavior reported for ionic conductivity through nanopores, i.e., a power law dependence of the ionic conductivity with the ionic concentration at low concentration, with an exponent much lower than 1. We also observe a flat slope for the conductivity of S#2 ($t=50 \mu\text{m}$) as a function of the concentration. The fact that reducing the dimension of the wall does not cause any conductivity change is an indication that transport occurs through fabrication defects rather than intrinsic wall porosities.

5.3.3 Comparison with PDMS

The comparison of the ionic conductivity obtained here with the one reported for similar walls made of PDMS shows that the SU-8 resin is similar or even less permeable to electrolytes and hence to water (Table 5.1). The ionic conductivity of the SU-8 was calculated for different wall thicknesses and compared with PDMS walls having different dimensions (Table 5.1). Data for the PDMS are taken from the work of another group in the lab[241]. Therefore, SU-8 is compelling with PDMS in terms of performance for any microfluidic device.

Table 5.1: SU-8 and PDMS ionic conductivity

Sample reference	Thickness [μm] & Length [μm] & Height [μm]	Conductivity [$\mu\text{S}/\text{m}$]
PDMS	40 * 40 * 1	8 - 15
PDMS	20 * 40 * 1	1.7
S#4 (50 μm)	50 * 10880 * 22	1.4 - 2.2
S#2 (50 μm)	50 * 10880 * 22	0.4 - 6.2
S#3 (85 μm)	85 * 10800 * 29	0.1 - 32
S#1 (85 μm)	85 * 10800 * 29	0.9 - 14

5.3.4 Ageing: time evolution of the conductivity

The measurement of the ionic conductivity as a function of time (Figure 6.17c) shows that there is no evolution trend over up to 16 weeks, although scattering is observed. One may expect a constant decrease or increase of the ionic conductivity if the nanoporosity was closing or opening when it is filled with the electrolyte. This shows that our SU-8 wall remains watertight for a longer period of time than usually observed on micrometric walls made of other materials. Indeed, materials such as PDMS/polystyrene (PS) based microfluidic devices were used for cell culture and showed 3 days stability[94], or the longest one month without degradation[102]. PMMA-based devices showed from 9 h[143] up to 3 days[144]. So far reported SU-8-based device durability time was 1 day[127].

5.4 Vacuum test

5.4.1 Measurement set-up

Finally, we assessed the ability of SU-8 to sustain fluids under vacuum. Noteworthy, it must be recalled that curing SU-8 at 200 °C for 2 hours significantly increases the reticulation rate of the resin, hence it is essential to limit outgassing as much as possible[128]. The proposed set-up used for this test is schematically drawn in Figure 5.11. It works on the principle of the so-called pressure rising method in dynamic vacuum[242]. In brief, the aim is to see an increase in the cell pressure while introducing water inside the test reservoir. The pressure rise would indicate a leak.

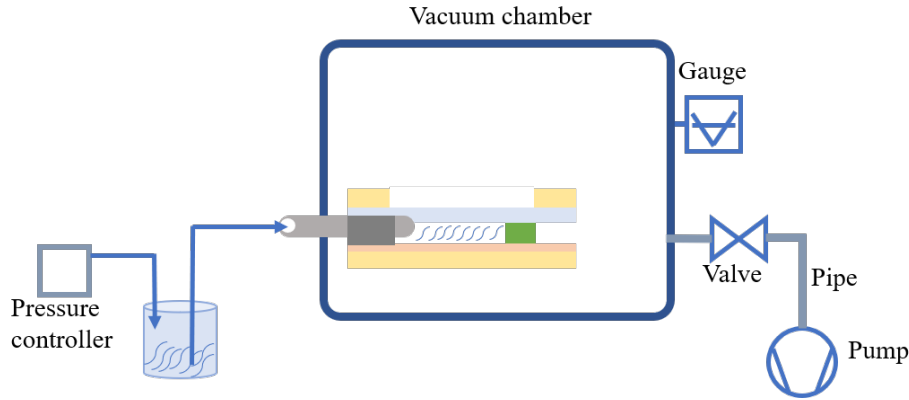


Figure 5.11: Schematic of the vacuum setup. The device is mounted in the chamber and SU-8 performance is tested by applying liquid water pressure under a secondary vacuum

5.4.2 Measurement of the leak rate

A single reservoir device, as shown in Figure 5.6, is mounted inside a vacuum chamber under a secondary vacuum, i.e., 5×10^{-5} mbar. First, we verified that the presence of the SU-8 device did not significantly degrade the vacuum in the cell. Then, the reservoir was filled with liquid water under pressure and the change in the gauge level was recorded. It is observed that applying a pressure of 1.5 bar of water for one hour does not induce any decrease of the vacuum, which remained constant at 5×10^{-5} mbar under pumping. This means that the outgassing from SU-8 and the SU-8 porosity to water must be extremely small.

We now estimate the leak rate Q_{leak} of particles, passing through our SU-8 device into the cell: By definition: $Q_{leak} = P_{cell} \times D_{leak}$, with P_{cell} the pressure at the level of the cell (as measured with our Gauge) and D_{leak} the debit in volume at a given pressure, expressed in $L \cdot s^{-1}$. Since the pressure in the cell is not changing over the leak test, one can write that the effective pumping speed at the level of the cell (D_{cell}) compensates the leak rate of our device (D_{leak}) and the outgassing ($D_{outgassing}$) from the cell: $D_{leak} + D_{outgassing} = D_{cell}$. For the sake of simplicity, we will estimate an upper bond of D_{leak} by writing:

$$D_{leak} \leq D_{cell} \quad (5.3)$$

To compute D_{cell} , we recall that the flux of particles Q is equal everywhere (from the cell to the pump) and can be written as:

$$Q = P_{cell} \times D_{cell} = P_{pump} \times D_{pump} = C(P_{cell} - P_{pump}) \quad (5.4)$$

Where P_{cell}/P_{pump} and D_{cell}/D_{pump} are respectively the pressure and the debit in volume at the level of the cell/pump, C is the conductance of the circuit connecting the cell to the pump (pipes and valve). From Equation 5.4, we can write: $\frac{1}{C} + \frac{1}{D_{pump}} = \frac{1}{D_{cell}}$. It comes:

$$D_{cell} = C \frac{D_{pump}}{C + D_{pump}} \quad (5.5)$$

$D_{pump} \sim 85 \text{ L} \cdot \text{s}^{-1}$ is obtained from the datasheet of our pump. Because D_{pump} is constant for pressures below 10^{-4} mbar , we approximate that $D_{pump}(P_{pump}) \sim D_{pump}(P_{cell})$. We will see in what follows that D_{cell} is anyway dominated by C .

We now need to compute C , which is composed of 2 terms: C_{pipes} and C_{valve} . From the datasheet of our valve, $C_{valve} = 160 \text{ L} \cdot \text{s}^{-1}$. C_{pipes} is given in the molecular regime by $C_{pipes} = \frac{d^3}{L} \sqrt{\frac{2\pi k_B T}{m_{N_2}}}$ [243];

Therefore, $C_{pipes} = 16.2 \text{ L} \cdot \text{s}^{-1}$ where $L = 2.4 \text{ m}$ and $d = 6 \text{ cm}$ are length and diameter of the pipes respectively.

Finally, $\frac{1}{C} = \frac{1}{C_{pipes}} + \frac{1}{C_{valve}}$ and $C \sim 14.7 \text{ L} \cdot \text{s}^{-1}$.

Injecting in Equation 5.5 we get $D_{cell} \sim 12.5 \text{ L} \cdot \text{s}^{-1}$.

And finally, Equation 5.4 gives us $Q = P_{cell} \times D_{cell} \sim 6.3 \times 10^{-4} \pm 1.9 \times 10^{-4} \text{ mbar} \cdot \text{L} \cdot \text{s}^{-1}$, with the error bar being set by resolution of the Gauge.

The calculated upper bound of the leak rate is better than the leak rate corresponding to the water vapor leak tightness which is in the range of $10^{-3} \text{ mbar} \cdot \text{L} \cdot \text{s}^{-1}$ [244]. We can therefore conclude that SU-8 is impermeable to water vapor, in addition to be compatible with UHV (no outgassing) operation.

5.5 Conclusion

We reported that micrometric walls made of SU-8 resin with thicknesses as low as $35 \mu\text{m}$ exhibit liquid water pressure leak tightness from 1.5 bar up to 5.5 bar and no porosity even after 2 months of aging. We also find that SU-8 can be operated under a secondary vacuum as a microfluidic seal with no degradation of the vacuum (neither outgassing of the SU-8 nor liquid water or gas permeability). Moreover, the fabrication process we propose requires neither aggressive chemical nor high temperature nor high energy plasma treatment. It thus opens a new perspective to seal microchips when sensitive surfaces or materials have to be used.

Electronic response of CNTFET upon water adsorption

It has been already shown that the extraordinary electrical sensitivity, small pore size, and high aspect ratio of a CNTFET makes it an excellent tool to use as an electronic sensor for analyte adsorbed on the outer surface[245]. However, the impact of the adsorption of water inside the CNT remains largely unexplored. The hydrophobic interior can be wetted because the chemical potential of water inside is lower than outside. It can thus be assumed that the confinement of water inside the CNT results from an entropic factor likely due to the specific structure and dynamics of the confined water molecules.

In this chapter, we will detail our research carried out on a FET made of individual SWCNT to distinguish the impact of water adsorbed outside the tube from that confined inside. Also, the effect of (i) the dielectric constant of the environment, (ii) the water filling & emptying kinetics, and (iii) CNT metallicity dependence is reported. To make it short, we observed that CNTFET is an excellent tool to study these processes. CNT doping due to the presence of water is observed as the main effect that appeared as the shift of the gate threshold voltage in the conductance curve of the CNTFET.

6.1 CNTFET device fabrication and characterization methodology

A back gate design is used to fabricate our CNTFET. The device fabrication is achieved in a clean room and CNT is synthesized using Chemical Vapor deposition (CVD) on the substrate. Finally, metallic electrodes are deposited onto it.

6.1.1 CVD: CNT growth (focus on individual SWCNT)

6.1.1.1 Optical mark etching

Firstly, optical marks are created on the SiO₂ (300 nm thick) / Si wafers to clearly identify the location of the CNT. This process is done in two steps. First, UV photolithography is used and the protocol process is detailed in "Protocol 1" (Appendix A). Shortly, the AZ5214EU photoresist is employed as a negative tone resist to cover the surface of the substrate and

to develop with a photoresist developer AZ726MIF the area for optical mark pattern. After patterning, two different methods can be used to create permanent optical marks on the substrate: (i) metal deposition or (ii) SiO_2 etching. We used SiO_2 etching because it is a simple and faster method.

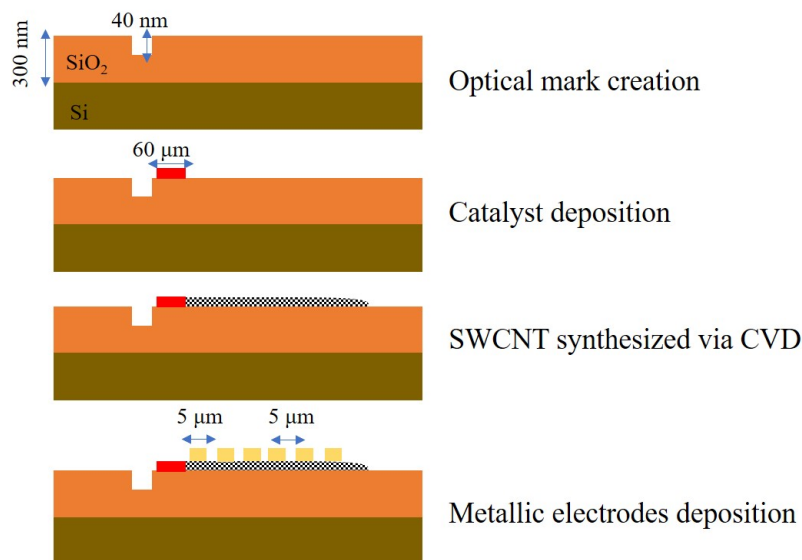


Figure 6.1: Scheme of the CNTFET sample fabrication processes step by step

Reactive ion etching (RIE) is used to etch SiO_2 . During this process, the "Dow Corning 704" silicone oil is added between the back of the sample and the sample holder to enhance thermal heat transport. Etching is achieved using O_2 and CHF_3 gases under 10 mTorr vacuum at 22 °C with radio frequency (RF) power of 150 W for 2 minutes. Then, the resin on the surface is cleaned with pure oxygen plasma for 10 min. It is observed that the cleaning process is one of the most critical steps in order to get high-quality CNTs from CVD. Poorly cleaned substrates have some resist residues which lead to contamination of the surface during CVD growth. Thus, after the inductively coupled plasma (ICP) process is completed, the wafers are sonicated in an acetone batch for 5 min followed by isopropanol (IPA) rinsing and N_2 drying. Then they are dipped into RPG at 80 °C for 1 hour to remove all resist impurities followed by rinsing with deionized (DI) water and IPA, and finally dried using N_2 flow. The etching depth measured with a profilometer is around 40-50 nm. The top design in Figure 6.1 presents this process.

6.1.1.2 Catalyst deposition

Hydrated FeCl_3 nanoparticles are used to prepare the catalyst solution. 15 mM FeCl_3 in Methanol solvent is prepared using sonication for 20 minutes in order to homogeneously dissolve the nanoparticles in the methanol. Once the catalyst solution is prepared, it is mixed with a photoresist resin. The mixture preparation and the lithography process to deposit the catalyst patterns are explained in detail in "Protocol 2" (see Appendix A). To make it short, the catalyst solution is mixed with the S1818 photoresist in a volume ratio of 3/20 and homogenizes with the stirrer at 2000 rpm for 1 min. Then the mixture is deposited on the substrate using the S1818 as a positive tone photoresist. After the dissolution of the exposed

part with the AZ726MIF developer, the catalyst patterns are formed on the substrate surface. The selected pattern dimension is $60\ \mu\text{m} \times 100\ \mu\text{m}$ (Right image in Figure 6.2). The scheme of the catalyst deposition is presented in Figure 6.1. The right image in Figure 6.2 shows the optical microscope observation of the device after catalyst patterns deposition.

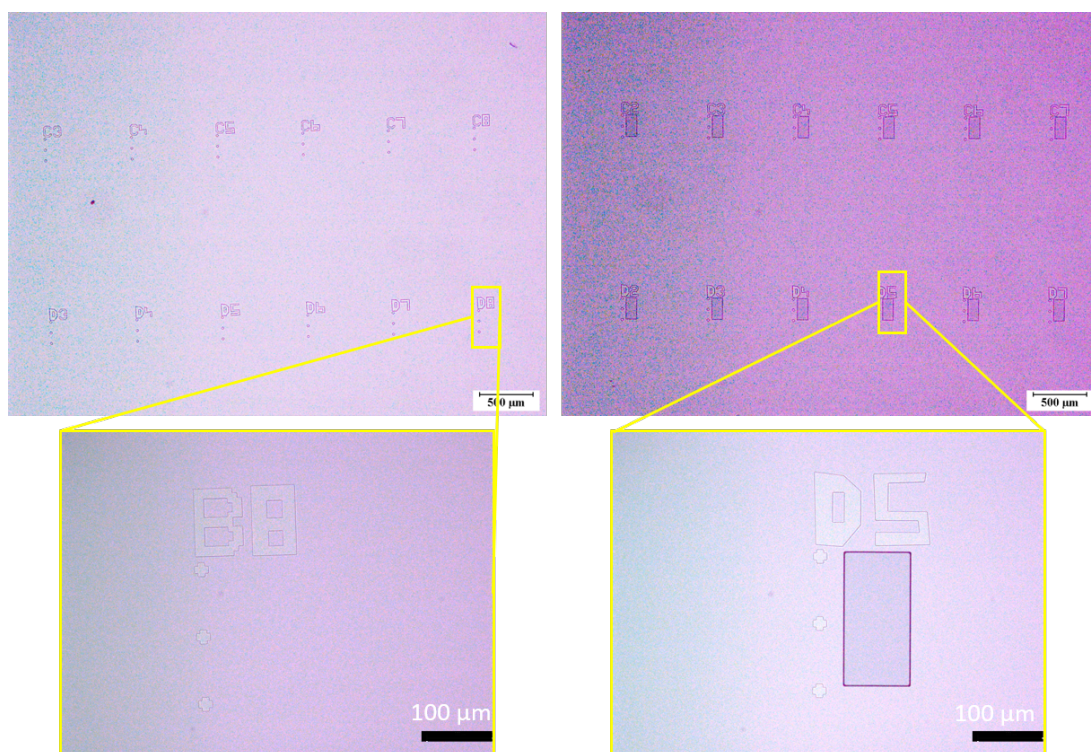


Figure 6.2: Image of optical marks and catalyst deposition by optical microscopy: the substrate surface after optical mark creation in the left, after catalyst pattern deposition on the right. The insets below show zoom images.

6.1.1.3 CVD growth

The CNT synthesis process is achieved by using chemical vapor deposition (CVD). The substrates are calcinated in air at $700\ \text{°C}$ for 5 min starting from room temperature with a heating rate of $15\ \text{°C}/\text{min}$. This step burns the photoresist which is used to pattern the catalyst and removed as much as possible from the CVD furnace, but also oxidization of catalyst particles. The synthesis process of CNTs involves the decomposition of carbon-containing gas to form nanotubes from the catalyst nanoparticles. The catalyst-patterned substrate is placed inside the CVD chamber. The chamber is then purged with Argon (Ar) to remove air or any impurities. The furnace is heated at $15\ \text{°C}/\text{min}$ to $900\ \text{°C}$. After temperature stabilization, the reactive gas which is made of Hydrogen (H_2), and carbon-containing precursors such as Ar/EtOH is introduced with a flux 190 standard cubic centimeters per minute (*sccm*) and $33.33\ \text{sccm}$, respectively. At this temperature, the carbon-containing gases decompose, releasing carbon atoms. The decomposed carbon species adsorb onto the catalyst nanoparticles, which act as nucleation sites for CNT growth. Various parameters, including temperature and gas flow rates, control the CNT growth rate as well as its diameter. After 30 min, the process is stopped by reducing the flow of carbon-containing gas and allowing the reactor to cool down. The third scheme in Figure 6.1 shows the sample after the CNT synthesis step.

While the CVD process mainly yields SWCNT, it is also known that MWCNT and Bundles can also grow from catalyst.

In Appendix B, we detail the CVD parameters, as well as catalyst particles, that have been used to synthesize as many as possible individual SWCNT with diameters below 1.4 nm.

6.1.2 SEM: selecting CNT

The synthesized CNTs are then characterized using techniques such as (i) scanning electron microscopy (SEM) to observe CNT on the substrate surface, (ii) Raman spectroscopy to determine the diameter of the CNT of interest, and (iii) atomic force microscopy (AFM) to get another approximation of the selected CNT diameter.

CNT characterization process first starts with SEM observation. A typical SEM picture of the sample after CVD is presented in Figure 6.3. SEM allows us to observe the surface morphology and composition of various samples with nanometric resolution. This is one of the most used tools to get preliminary information. SEM allows us to observe the growth density, and the CNTs' length and to locate them thanks to the optical marks. This is essential for the next steps: metallic contact deposition, Raman, and AFM measurements.

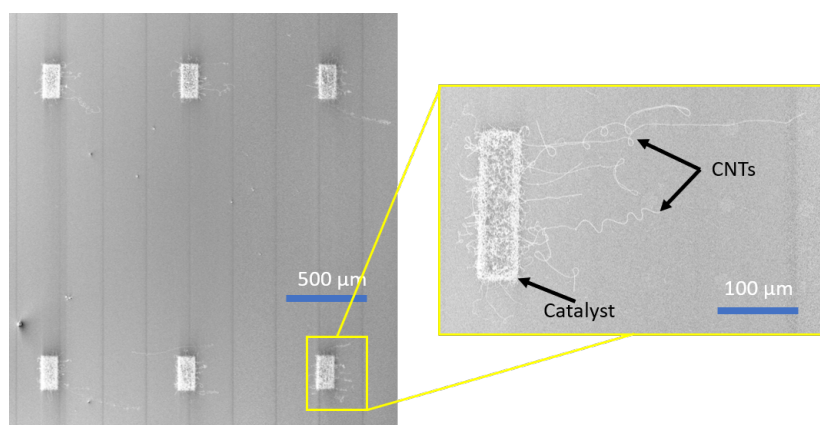


Figure 6.3: SEM observation of as-grown CNTs

6.1.2.1 Raman: Diameter distribution of CNTs in the catalyst pattern

μ -Raman spectroscopy is a tool to access the vibrational and rotational levels of molecules or solids, from which it is possible to get insight into the molecular composition and the structure of the investigated material. Here, we mainly look at the radial breathing mode (RBM) of the CNT, showing up as peaks in the range 100 and 300 cm^{-1} . Then the diameter can be estimated from the frequency of this band using the following equation[246, 247]:

$d_{CNT} = 217.8 / (\omega - 15.7)$, where d_{CNT} is the diameter of the CNT in nm, ω is the frequency in cm^{-1} .

A Renishaw spectrometer confocal microscope is employed to carry out our measurements. Three lasers with different wavelengths (532 nm, 633 nm, 785 nm) are used. These three wavelengths enable us to observe CNTs within diameters in the range of 0.5 nm up to 2.5 nm thanks to the Kataura plot (see Appendix B for more information). Figure 6.4 presents the diameter distribution of the CNTs synthesized with our protocol (see Appendix B for

the impact of different catalysts and CVD parameters on the CNT growth). The nanotubes growing outside the catalyst, which are used later to form the CNTFET, are expected to have a similar diameter distribution.

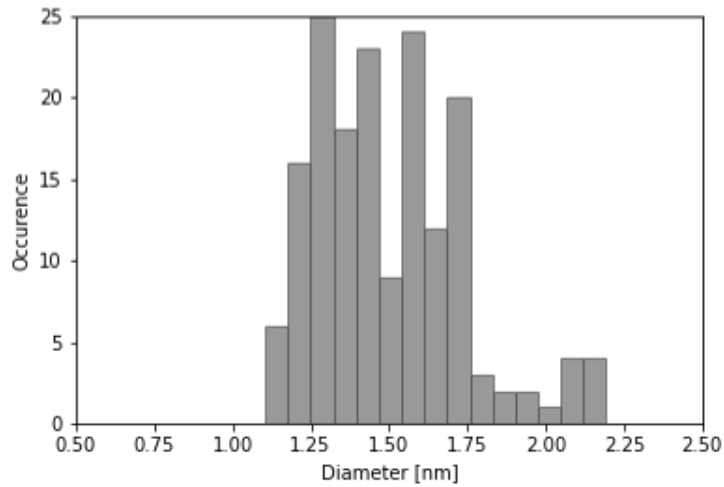


Figure 6.4: Diameter distribution of the CNTs synthesized from the catalyst pattern determined from RBM peak measured with Raman spectroscopy

6.1.3 Clean room fabrication

6.1.3.1 Metal contacts deposition and lift-off

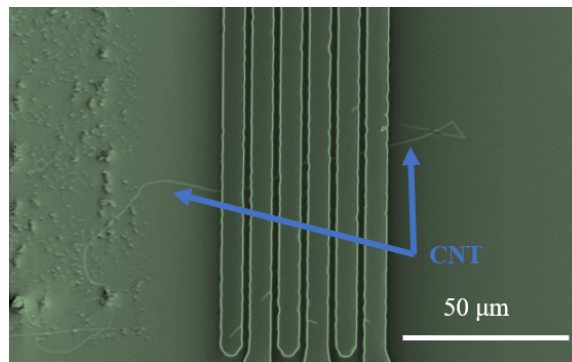


Figure 6.5: SEM observation of the sample after lift-off process

The CNT to be studied is selected using SEM and thanks to its precise location based on the optical marks, a bilayer photolithography process is applied to pattern the metallic electrodes. In order to have high-performance CNTFET, it is better to pattern metallic contacts closer. We patterned them 5 μm in distance in order to avoid electrical leakage and lithographic challenges. The LOR5A and AZ5214EU photoresist is used. The photolithography process is explained in detail in "Protocol 3" (Appendix A). After the development of the sample with AZ726MIF photoresist developer, Ti and Pt electrodes, 10 nm and 90 nm thick respectively, are deposited on the CNT. Figure 6.1 shows the sample after the deposition of the metallic contacts.

The lift-off process is done in two steps: firstly in acetone for 1 min to remove metals and

AZ5214EU from the undeveloped areas, and in the second step in RPG at 80 °C for 2 min in order to lift off Lor5A. The SEM image of the sample after the lift-off process is presented in Figure 6.5.

6.1.3.2 AFM: estimation of the nanotube diameter

Atomic force microscopy (AFM) technique allows for high-resolution imaging and characterization of surfaces at the atomic and nanoscale by measuring the forces and interactions between the tip and the sample surface.

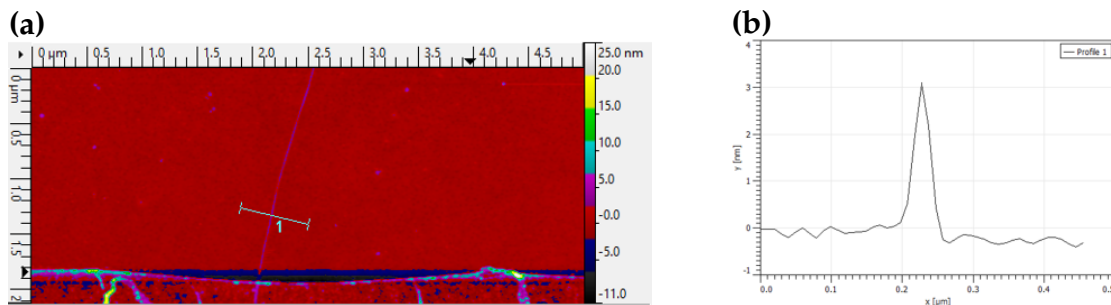


Figure 6.6: CNT diameter estimation with AFM: (a) AFM observation of the CNT on substrate, (b) cross profile extracted from AFM image allowing estimating the CNT diameter

Once the sample is ready, AFM measurement is carried out to estimate the diameter of the selected CNT. We observe that the diameter of the so-grown CNT is about 2-3 nm from the surface analysis of the AFM image (Figure 6.6). Observing a bigger diameter CNT compared to Raman is related to the precision of the AFM tool and the dirtiness of the device surface because of resist residues. This tool does not allow us to determine if the CNT is single-wall, multi-wall, or even bundle.

6.1.4 Measurement set-ups

6.1.4.1 Electrical measurement set-ups of CNTFET performance

The basic electrical measurements are carried out with a probe station. It is dedicated equipment to test and characterizes the electrical properties of CNT device (Figure 6.7a). It is used to verify that the devices are not leaky and to assign the metallicity of the CNT. The sample is placed on the sample holder of the probe station and a micropositioner is used to align and connect the sharp needle-like tips to metallic contact.

A dedicated custom vacuum chamber was designed to be able to measure the device under vacuum also made. The gauge is placed at the level of the sample and is connected to a secondary pump (schematic in Figure 6.7b).

In both set-ups the electrical measurements are carried out by a Source Measurement Unit (SMU), and DC voltage sources, which allow us to remotely control and measure the electrical response of the CNTFET.

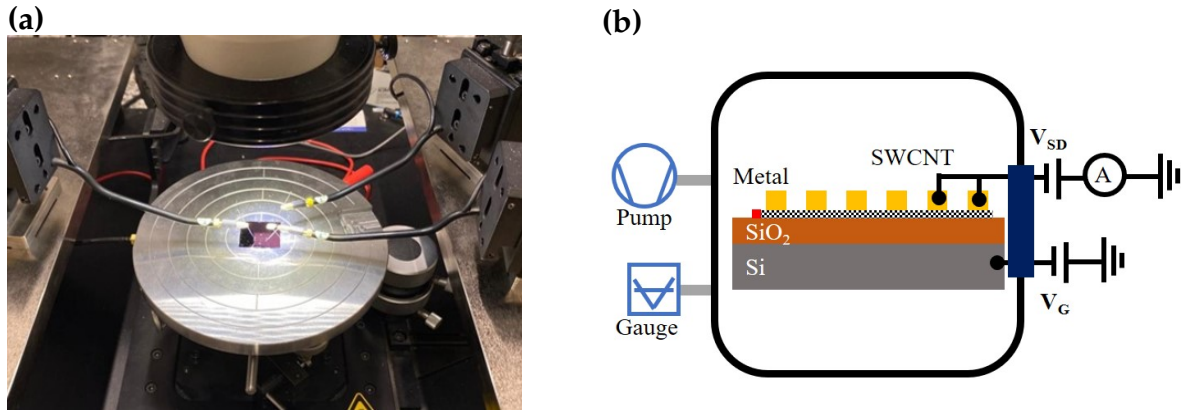


Figure 6.7: Measurement set-ups: (a) photography of probe station, (b) schematic of set-up for measurement under vacuum

6.1.5 About the two type of measurements

Various types of measurements can be carried out. In this work, we mostly use only two types. First, voltage-current (I_{SD} & V_{SD}) characteristics to access the resistance between the selected electrodes (see Figure 6.8a). This method is used to measure the CNT resistance, the contact resistance between the metallic electrodes, and the CNT. It was also used to determine resistance between electrodes when a liquid water drop is deposited on the substrate when there is no CNT. This is mandatory to check that the water conductivity can be neglected and, on the other hand, to fix the DC voltage range in which no water electrolysis occurs.

The second type of measurement is the conductance of the CNT where a voltage is applied to the back gate to modulate the CNT electrical features (see Figure 6.8b).

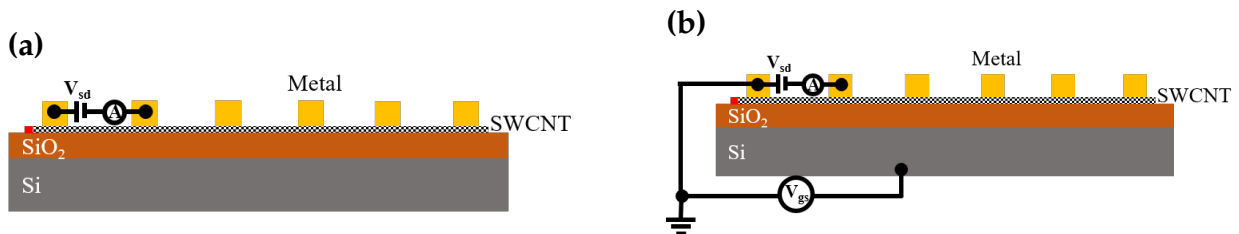


Figure 6.8: Schematic of the circuit for different measurement types: (a) schematic for I_{SD} & V_{SD} measurement, (b) schematic for I_{SD} & V_G measurement

One of the important characterizations is to precisely measure the noise of the set-up: this includes determining the baseline of the probe station in air and in the case of the vacuum set-up (in air and under vacuum). The electrical leak between the back gate and the electrodes is the main baseline which is measured in different set-ups for the sample without CNT at room temperature in the humidity 40%-50% (Figure 6.9). The observed difference in the case of vacuum set-up in the air is from the impact of the humidity on the electrical feedthrough, which disappeared under vacuum.

The resistance when water drops covers the CNTFET is compared with that of the CNTFET in air and the effect of applied voltage on the water electrolysis process are presented in Figure 6.10a. We observe that the resistance of the liquid water is \sim GOhm, which is much

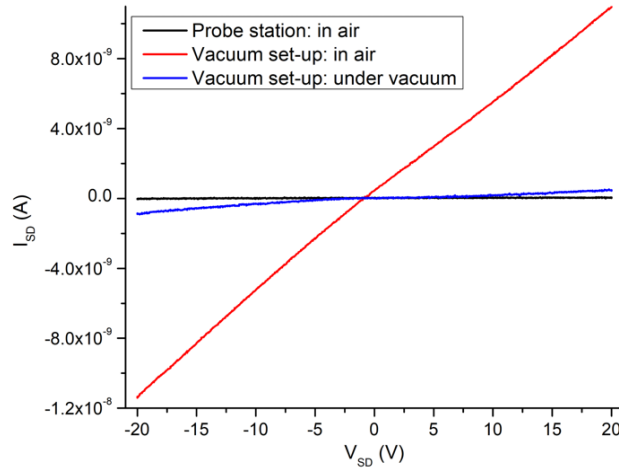


Figure 6.9: Gate electrical leak baseline for probe station in air, vacuum set-up in air and under vacuum measured in the [-20, +20] V ranges

higher than that of CNT in air, which is 1.4 MOhm. Liquid water conductance will thus be considered negligible in the following.

Measuring I_{SD} & V_{SD} dependence for liquid water on the electrodes without CNT in the [-2; +2] V ranges allows us to clarify the applied voltage interval within which the water electrolysis process can be neglected. It was reported that water electrolysis operates with a voltage for water splitting of nearly 1.2 V [248], which also explains why we observe such a difference when we measure I_{SD} & V_{SD} in the range of [-2; +2] V instead of [-1; +1] V in the case of Figure 6.10a. Our assumption is that it can be neglected in the [-100; 100] mV range (Figure 6.10b).

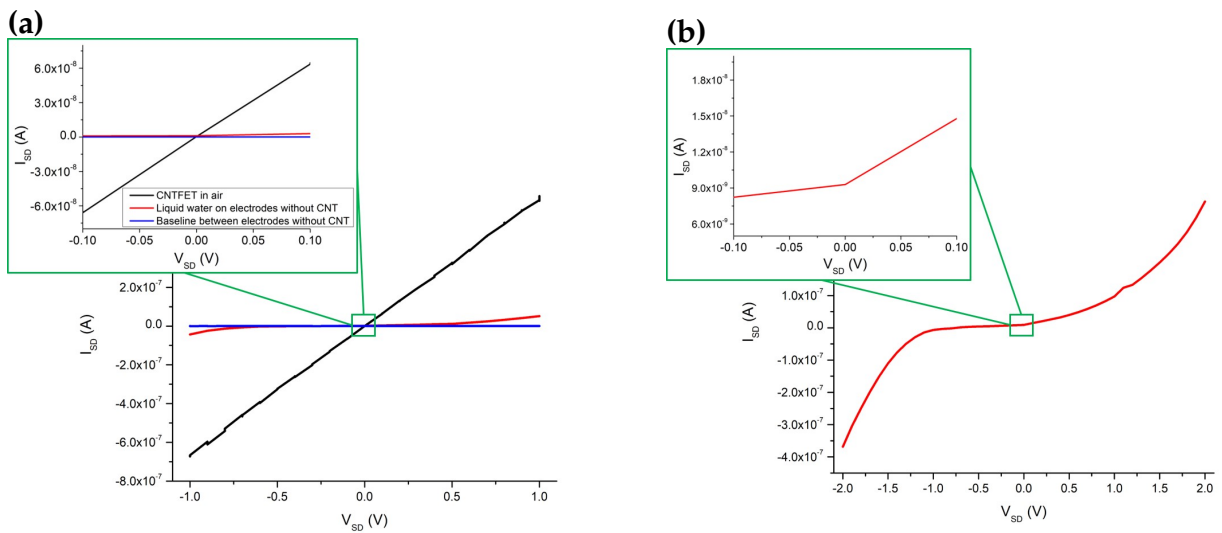


Figure 6.10: I_{SD} & V_{SD} primary measurements: (a) I_{SD} & V_{SD} comparison between water drop and CNT separately, (b) typical curve obtained with a water drop

6.1.5.1 CNT resistance in air & length dependence

The CNT is connected with metal leads to provide electrical contacts. The quality of the electrical contacts is important for the functioning and performance of our SWCNT-based devices. The main parameters that can affect the contact can be the geometry, the metal type, and cleanliness of the SWCNT surface.

Figure 6.11 shows the I_{SD} & V_{SD} dependence for various 5 μm CNT sections in the same sample, and the inset shows the extracted resistances. The scattering is observed in the resistance, while it is the same CNT and all sections are 5 μm . This scattering can be explained by either the defects formed on the CNT or the poor contact between CNT and metal at the specific area.

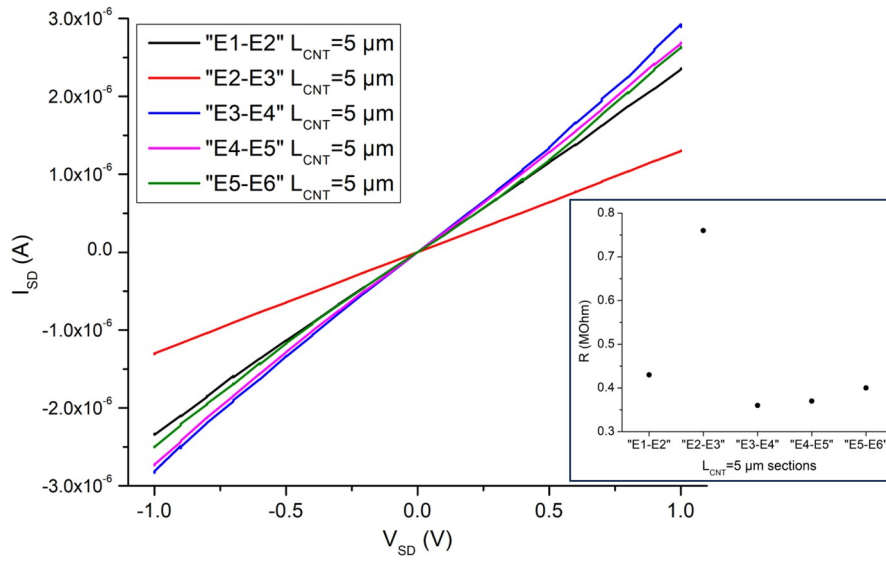


Figure 6.11: I_{SD} & V_{SD} curves for 5 μm CNT sections on the same CNT. Inset shows resistances extracted from these measurements for each 5 μm sections

Figure 6.12 shows the I_{SD} & V_{SD} and the conductance curve measured between different electrodes for different CNT lengths on the same CNT. We can see that there is a significant dependence on the CNT length but not as we may have simply expected. For instance, there is almost no difference when current is measured between electrodes 1-2 and 1-3, i.e. when CNT length is 5 or 15 μm . This outcome can also be related to defects or weak contact problems with one of the electrodes.

Two assumptions can be made for the current passing through the metal/CNT contact in order to calculate the CNT resistance and the CNT/metal contact resistance: i) current passes through the CNT (see Figure 6.13a), ii) current passes through the parallel circuit of metal/CNT contact (see Figure 6.14a).

We first calculate the resistance distribution of the current that passes through CNT by measuring the resistance for all channel lengths. From these measurements, we extract and calculate the R_{CNT} for 5 μm length with the following equations system (Figure 6.13a).

$$\begin{aligned}
 R_{i,i+1} &= 2R_c + R_{CNT} \\
 R_{i,i+2} &= 2R_c + 3R_{CNT} \\
 R_{i,i+3} &= 2R_c + 5R_{CNT}
 \end{aligned}$$

R_c is the contact resistance between the metallic electrode and the CNT, R_{CNT} is the resistance of CNT 5 μm long section, i is the number of the selected contact, $R_{i,i+1}$, $R_{i,i+2}$, and $R_{i,i+3}$ are the measured resistance between the selected contacts.

The histogram in Figure 6.13b shows the distribution of the values of R_{CNT} for 5 μm long section extracted from all measured values. The mean R_c and R_{CNT} values are about 70 kOhm. Noteworthy, having negative values for the resistance in the distribution is supposed to be related to the weak contact created with one of the electrodes as observed in Figure 6.11 and Figure 6.12.

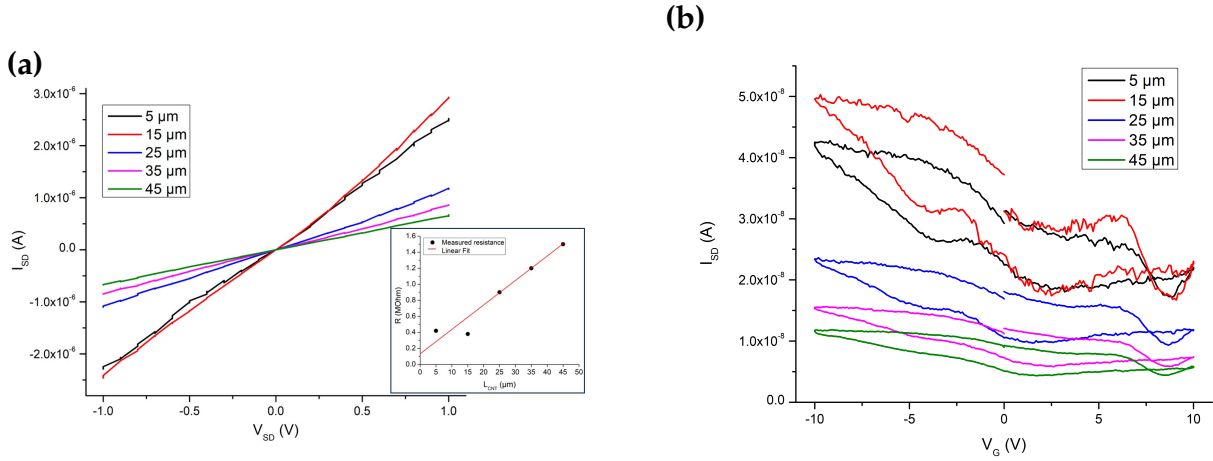


Figure 6.12: CNT electrical performance channel length dependence: (a) I_{SD} & V_{SD} dependence for different channel length on a same CNT (inset shows resistances extracted for each lengths, respectively), (b) I_{SD} & V_G dependence for different channel lengths on a same CNT measured with $V_{SD} = 10 \text{ mV}$

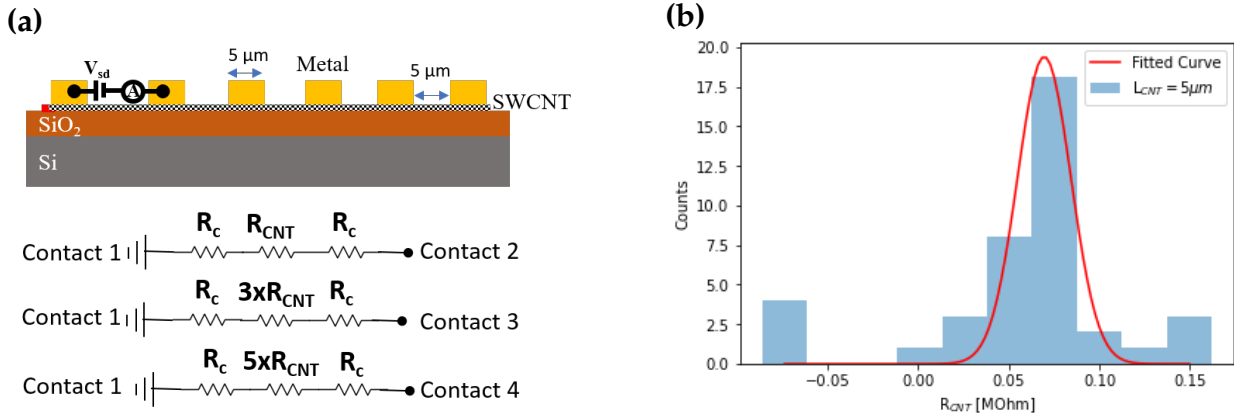


Figure 6.13: Calculation of the CNT resistance for 5 μm channel length extracted from the resistance of different channel lengths: (a) schematic to calculate the resistance, (b) resistance distribution calculated for $L_{CNT} = 5 \mu\text{m}$.

If we now take into account in addition that there can be current passing through the parallel circuit in the metal/CNT contact, then we can calculate the resistance distribution of $R_{CNT} + R_{MIX}$ with the same method using the equations systems below from which we can extract and calculate the $R_{CNT} + R_{MIX}$ distribution (Figure 6.14a).

$$R_{i,i+1} = 2R_c + R_{CNT}$$

$$R_{i,i+2} = 2R_c + 2R_{CNT} + R_{MIX}$$

$$R_{i,i+3} = 2R_c + 3R_{CNT} + 2R_{MIX}$$

Here, R_m is the resistance of metal, R_{MIX} is the parallel combination of R_m and R_{CNT} for 5 μm long section: $R_{MIX} = \frac{(2R_c + R_m)R_{CNT}}{2R_c + R_m + R_{CNT}}$.

The histogram in Figure 6.14b shows the distribution of the values of $R_{CNT} + R_{MIX}$ extracted from all measured values. The mean value is 136 kOhm. Then, we take into account the value obtained for 5 μm long R_{CNT} in assumption 1, we obtained that $R_{MIX} \approx R_{CNT}$. Thus, we can use assumption 1 (Figure 6.13), which means that the current passes through CNT rather than metal and CNT contact.

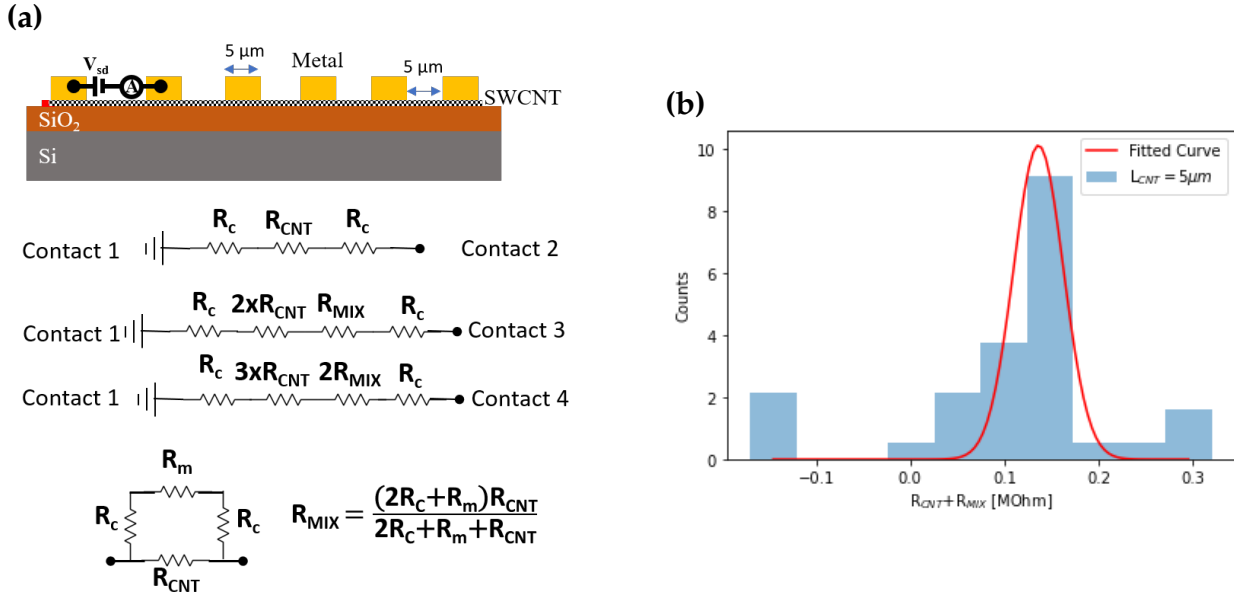


Figure 6.14: Resistance distribution of $R_{CNT} + R_{MIX}$ extracted from the resistance of different channel lengths: (a) schematic to calculate the resistance, (b) calculated resistance distribution

6.1.6 CNT opening and individual SWCNT characterization

6.1.6.1 Distinguishing individual SWCNT from MWCNT and bundles

As discussed in the CVD growth section, we obtain a majority of SWCNT. However, it is also possible to find MWCNT or Bundles.

Selecting individual SWCNT is one of the most important points in this work. SEM helps to localize the CNT, but cannot tell us whether the CNT is a single-wall (SW), a double-wall (DW), a multi-wall (MW), or even a bundle. It is the same with AFM. We thus need another tool to determine the exact nature of the CNT seen from SEM. This can be achieved using the current fusing method. The principle is to place the CNTFET under vacuum in order to avoid oxidation and to apply an increasing value of V_{SD} until a sufficiently high current is produced, inducing Joule heating in the CNT. Hence when the temperature reaches a sufficiently high value, the CNT fuses. The electrical circuit becomes suddenly open, and the current I_{SD} falls to zero.

The breakdown current and curve are important parameters to distinguish CNTs. CNTs with breakdown currents lower than 30 μA and with a single cut as reported in Figure 6.15

correspond to individual SWCNT. However, CNT which exhibits higher breakdown current and also exhibits two or more cuts can be bundle, DWCNT, or even MWCNTs (Figure 6.15b).

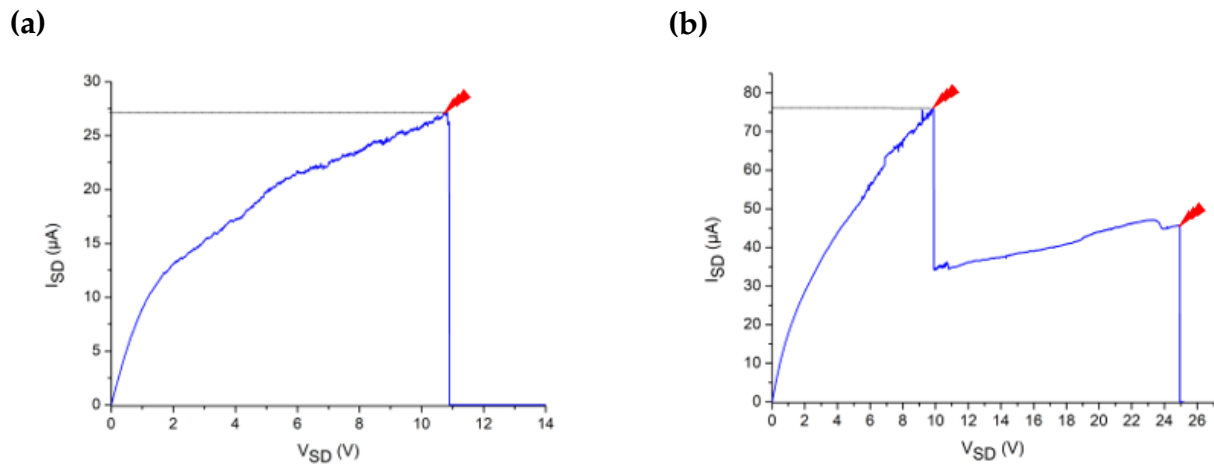


Figure 6.15: Sorting CNTs based on the fusing: (a) opening corresponding to individual SWCNT (b) opening corresponding to another group of CNTs

6.1.6.2 Current annealing

The current annealing method aims at cleaning the CNT surface from impurities and also curing of structural defects and thus increasing the CNT electrical performances[249]. This method can be used to remove the adsorbed and confined molecules by heating them at high temperatures. It was reported that with biasing the CNT in the 1-10 V range, the temperature can go above 1000 K via Joule effect[250, 251]. Providing that we know at which I_{SD} value SWCNT fuse, it is possible to apply a V_{SD} voltage before the breakdown value and thus to heat the CNT at temperature high enough to clean its surface and surroundings.

The conductance curve of a CNT 5 μm long in air before and after current annealing under vacuum is presented in Figure 6.16. An increase in the ON-state of the conductance and the shift in the gate threshold voltage is observed once CNT is exposed to air after the first current annealing which is done under vacuum. The increase can be related to the removal of the defects in the CNT or enhancing the metal/CNT contact, and the shift of the gate voltage can be explained as the decrease of the dopants after current annealing.

6.1.6.3 Effect of experimental electrical parameters on the transfer curve

Applying an electrical field through the p-doped local back gate of the device makes possible to measure the conductance curve (I_{SD} vs V_G) of the CNT. Before investigating the effect of the environment and the substrate, it is first mandatory to understand the impact of electrical parameters on the hysteresis observed on the conductance curve.

Hysteresis is formed in the conductance curve as a result of the impact of the environment or defects on the CNT. Charge trapping from the environment or even water on the SiO_2

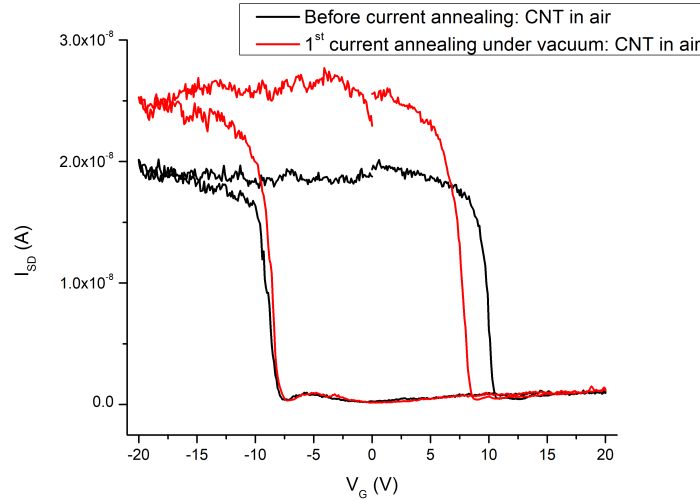


Figure 6.16: The impact of first current annealing on CNT conductance curve: Current annealing is done under vacuum, CNT is measured in air in both cases

surface and at the interface between SiO_2 and CNT lead to the form of silanol groups on the dielectric surface which exhibit hysteresis. We can see that some experimental parameters such as the gate voltage screening window (Figure 6.17a), the gate voltage sweeping rate (Figure 6.17b), direction (Figure 6.17c), and applied bias voltage (Figure 6.17d) can lead to change hysteresis. Hysteresis modification due to the electrical experimental parameters used is related to the charge trapping/detrapping mechanism.

Increasing the gate voltage range leads to an increase of the width of hysteresis, which is related to the density of the available charge traps[252] (Figure 6.17a).

Increasing the gate voltage sweeping rate leads to a decrease of the hysteresis. This might be explained since the required time for the charge trapping and de-trapping from the substrate takes time[253] (Figure 6.17b).

The gate voltage sweeping direction can also impact the width of hysteresis based on the same principle (Figure 6.17c).

The increased V_{SD} voltage can enhance the carrier injection into the CNT channel, resulting in higher current and also it can affect the charge distribution in the CNT and the interaction with nearby charge traps which results on a change of the hysteresis[254] (Figure 6.17d).

Thus, it is important to choose the same experimental parameters in all measurements for all CNTFETs whatever their environment. Therefore, we selected $[-20, +20]$ V gate voltage range, with normal sweep direction (see Figure 6.17c), 1 V/s sweeping rate, and $V_{SD} = 10$ mV which allow us to measure and observe the saturation values on both holes (p) and electrons (n) sides.

Based on the electronic properties of our CNTs, we observed two different types of conductance curves. The difference comes from their metallicity, as presented in Figure 6.18. We mainly observed semiconducting and semi-metallic (small band gap semiconducting). The semi-metallic or small band gap CNT has a higher ON-state current and lower I_{on}/I_{off} ratio compared to semiconducting CNT. Due to the lower band gap in the semi-metallic CNTs, electrons can require lower energy to pass from the valence band to the conduction band

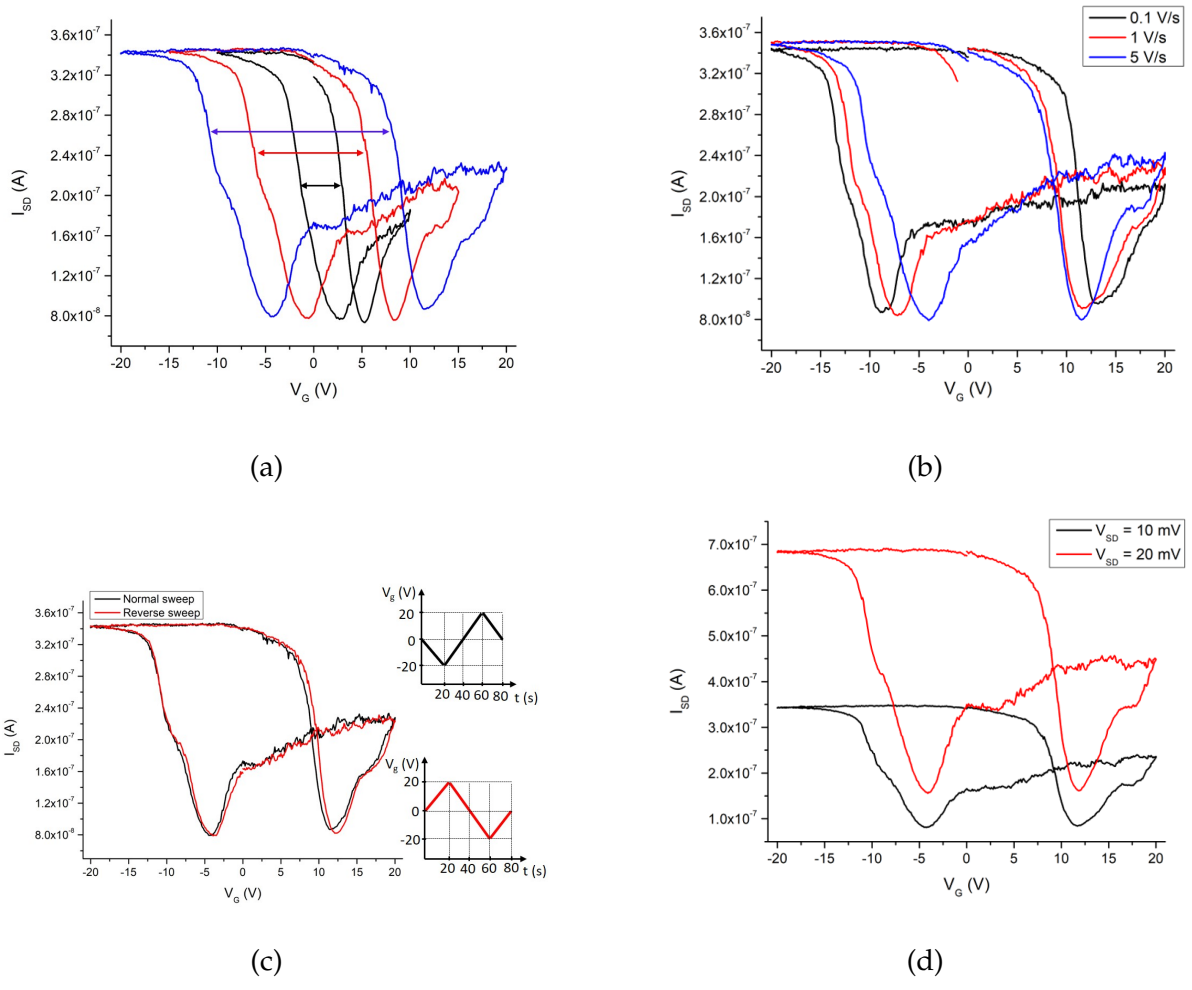


Figure 6.17: The effect of electrical experimental parameters on the conductance of CNT: (a) the effect of V_G screening window, measured with $V_{SD} = 10$ mV; (b) the effect of gate voltage sweeping rate, (c) the effect of gate voltage sweeping direction (insets represent directions), and (d) the effect of V_{SD} voltage

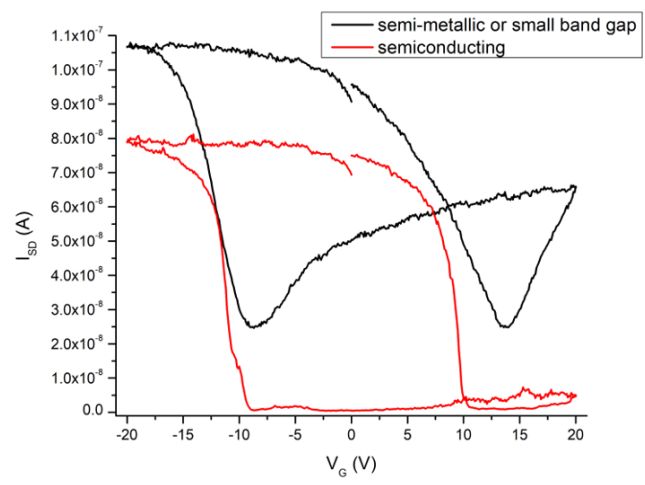


Figure 6.18: Conductance curve of semi-metallic (small band gap semiconducting) and semiconducting CNT measured with $V_{SD} = 10$ mV

and lead to current flow. The difference in the band gap in different CNT metallicities, the applied $V_{SD} = 10$ mV leads to a higher ON-state current when the band gap is getting smaller.

6.2 Impact of liquid drop on CNTFET electronic response

Here, our aim is to investigate the effect of liquid water as well as of a few other liquids having different dielectric constants on the electrical performance of our CNTFET by measuring the change on the conductance curve.

6.2.1 Case of "pure" water

The impact of liquid water on the electrical properties of a CNTFET is complex and has not been studied so far in detail. The effect of water drops on the conductance of the closed individual SWCNT is presented in Figure 6.19.

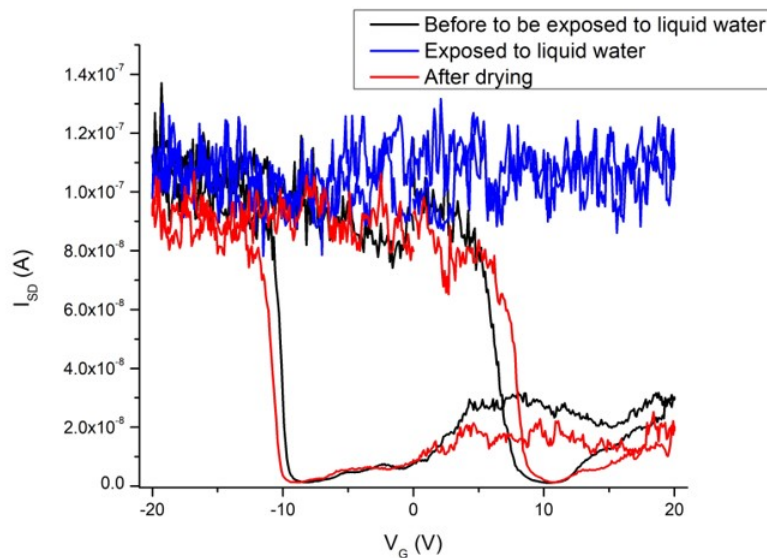


Figure 6.19: The impact of liquid water on the conductance curve of the CNTFET

It is observed that liquid water has a strong impact on the electrical response. When it is exposed to liquid water the hysteresis disappears while the I_{SD} remains unchanged. This outcome is similar to the work of Cao et al.[224], they also observed that the impact of liquid water on the closed and open individual SWCNT leads to the disappearance of the hysteresis. It is thus extremely clear that the occurrence of liquid water on the top of the tube can easily be detected electrically. Furthermore, it can be seen that after the water evaporation, the CNTFET recovers the same conductance curve, with only a very small shift, which can be related to the increased amount of charge traps on the substrate surface. In conclusion, the effect of liquid water is reversible, and the effect can be either doping based on the increased amount of charge traps in the case of liquid water or the capacitance effect based on the higher dielectric constant of water.

6.2.2 Case of other liquids: effect of the dielectric constant or charge traps

In order to explain the impact of liquid water, if it results from the capacitance effect (owing to the high dielectric constant of water), non-aqueous liquids with different dielectric constants are tested. The I_{SD} vs V_G curves recorded with the CNT in air or covered by exposed to silicone oil ($\epsilon=2.96$) is presented in Figure 6.20a.

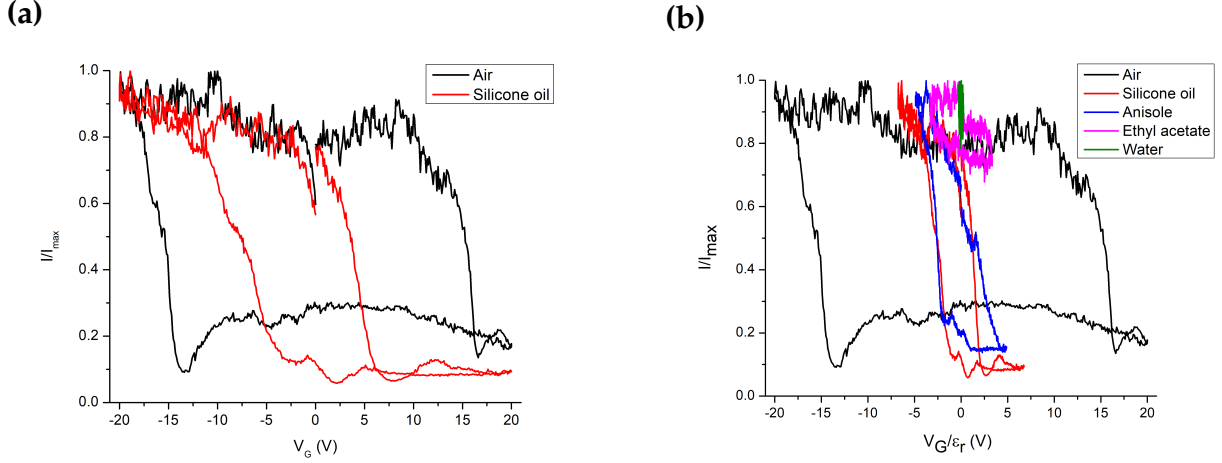


Figure 6.20: The impact of liquids with different dielectric constants: (a) the impact of silicone oil on the CNTFET, b) liquids with different dielectric constants

We observe a shrinking of the hysteresis but still with a significant I_{on}/I_{off} ratio, which is roughly centered around $V_G \sim 0$. The effect is thus clearly different from that observed with water. Testing other liquids having different dielectric constants thus appears to be potentially informative. If the change is due to the dielectric constant of the liquids, then it should be possible to obtain a master curve by rescaling the V_G axis. The created charge or electric field based on the applied gate voltage is calculated as $q_G = C_G V_G$. Here, C_G is gate capacitance, which is calculated as $C_G = 2\pi\epsilon_r\epsilon_0 / \ln(2h/r)$, where ϵ_0 , h , and r are the dielectric constant of vacuum, silicon dioxide thickness, and CNT radius, respectively. ϵ_r is the dielectric constant of the dielectric material or environment. Thus the main changeable parameter in C_G is ϵ_r . Therefore, as the transconductance is proportional with the created charge: $G \propto q_G(V_G, \epsilon_r)$. Rescaling of the axis is made by dividing V_G by the dielectric constant of liquids in order to account for the electric field. The normalized I_{SD} versus V_G/ϵ_r dependence for different liquids such as Silicone oil ($\epsilon_r=2.96$), Anisole ($\epsilon_r=4.1$), Ethyl acetate ($\epsilon_r=16$) and water ($\epsilon_r=80$) is presented in Figure 6.20b. It can be seen the dielectric constant of the liquid is likely not the dominant parameter to explain the change in the curves. Therefore, we conclude from Figure 6.19 and Figure 6.20b that the dominant effect of water is doping. Needless to say, all these liquids are insulators and hence do not significantly modify the level of I_{on} .

6.3 Impact of water partial pressure and current annealing

The impact of water vapor on the electrical performance of CNTFETs when it is adsorbed outside has been reported by different research groups. It has been observed that air humidity leads to a change in the gate voltage[193, 222].

However, there are few experimental works about the effect of water when it is confined inside CNTs[224]. So, distinguishing the effect of water when it is adsorbed at the CNT external surface from when it is confined into the CNT channel must be clarified.

In this section, we present our results obtained on CNTFET with close and open tubes subjected to various water partial pressure. To make it short, it is possible to gain repeatable and reproducible behavior when the CNTFET is made of an individual SWCNT, whereas no clear trend could be identified if it is made of an MWCNT or a bundle. Thus we mainly report, in the following CNTFET behavior only when we could prove from the breakdown current, i.e $\sim 30 \mu A$, that it is made of a SWCNT.

In order to interpret the mechanism of the water vapor on the electrical performance of our CNTFET, we focused on the 4 possible mechanisms obtained from theoretical consideration about the effect of molecule adsorption on the CNT conductance curve (see Figure 4.11 in Chapter 4). I_{SD} & V_G curve is used as a tool to understand the molecule adsorption mechanism. These mechanisms are assumed as: i) gating effect which can be associated to the doping of the CNT, ii) change in the Schottky barrier, iii) change in the capacitance that may affect the CNT modulation, and iv) change in the charge carrier mobility which can be observed as a degradation of the CNT conductance.

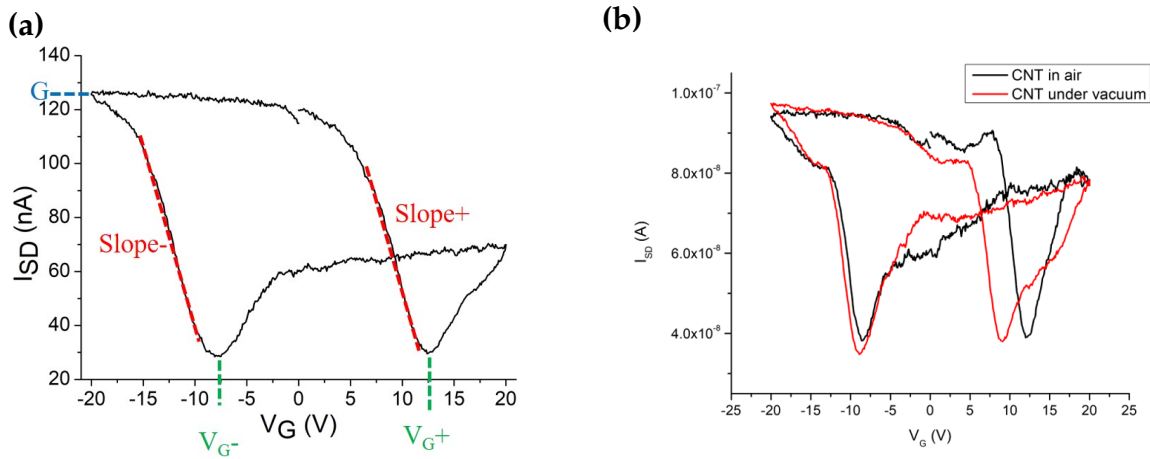


Figure 6.21: Main metrics in conductance curve of CNT in water & CNT interaction: (a) Main metrics in the conductance curve of CNT, b) the most reproducible and repeatable change based on water intercalation

The possible effects on the conductance curve were calculated by Heller et al.[208]. One of the changes in the I_{SD} & V_G curves caused by the adsorbed molecules can be related to a charge doping effect, which shifts the curve along the V_G axis. Another one related to the adsorbed molecules at the located metal interface corresponds to a change in the local work function and hence the band alignment, therefore, changing the Schottky barrier. The n or p Schottky barrier effect leads to asymmetric conductance change. In the case of this theoretical study[208] the low permittivity of the adsorbed molecules relative to the permittivity of

the FET dielectric layer results in a lowered gate capacitance. Finally, the decrease in carrier mobility reduced conductance in both the p and n branches.

In our measurements, we analyze the $I_{SD}&V_G$ curve of the CNT based on electrical metrics to distinguish the water partial pressure effect outside and inside the CNT. These metrics are the change of the ON-state conductance (G_{on}) value, the threshold voltages (V_G^+ or V_G^-), and the change of the slope in the transition between ON and OFF-states of the conductance (Figure 6.21a). After several measurements where CNT is treated in air, vacuum, and current annealed under vacuum, it clearly appears that the main repeatable and reproducible change concerns the threshold voltage on the positive gate voltages (Figure 6.21b). Based on the possible mechanisms associated with the molecule adsorption and on the evaluation of the electrical performance of the CNTFET, we conclude that the shift of positive threshold voltage V_G^+ corresponds to the doping of the CNT when exposed to moisture.

6.3.1 Case of close and open SWCNT in air

In order to clearly distinguish the effect of the water partial pressure outside and inside the individual SWCNT, we are first constrained to study the behavior of our CNTFET on the close tube, that is before the opening procedure and hence without knowing exactly what kind of CNT is present (SWCNT, MWCNT or bundle, see discussion in 6.1.6.1).

Four types of successive conditions are used when CNTFET is: (i) in the air directly after annealing (~ 1 min), (ii) in the air after an hour, (iii) under 10^{-3} mbar vacuum, and (iv) after current annealing under 10^{-3} mbar vacuum. Several cycles are performed once the behavior of the closed tube CNTFET is investigated. Then, the tube is opened and subjected to the same protocol.

Figure 6.22 reports the shift of the threshold voltage of the closed and open individual SWCNT during the different treatments. The protocol is successively repeated twice, denoted 1 and 2. "Air" means short time exposure (~ 1 min), "Air*" an hour exposure.

The comparison of the CNTFET response with a closed and open tube with $5 \mu\text{m}$ long section shows a significant difference.

Before interpreting these data, let us first recall that water molecules can either be physisorbed or chemisorbed; physisorbed means that the interaction with the substrate is rather weak while chemisorbed means that strong chemical bonding, either ionic or covalent, takes place. As far as our CNTFET is concerned, the physisorbed water molecules can be those adsorbed at the surface of the substrate, at the external wall of the tube, or confined inside its channel. The chemisorbed water corresponds to the silanol groups that are instantaneously formed at the SiO_2 surface. While the physisorbed water molecules can be desorbed under vacuum, even primary, at room temperature, much more energy is required to dehydroxylate the silanol groups and hence to recover a SiO_2 surface.

Taking as a reference state the state of our CNTFET after annealing under vacuum, that is when there is the sample has been totally dehydrated, it can therefore be concluded that the increase of V_G^+ when it returns to the air, whether the tube is close or open, indicates a strong impact of the water molecules, whether physisorbed or chemisorbed. This effect is rather fast, at least faster than the time scale which is needed to transfer the CNTFET from the secondary vacuum chamber and to the electrical measurement platform in ambient air,

i.e. about 1 minute. This is supported by comparing the data Air and Air*, showing no differences. The other outcome is that, in air, there is no way to discriminate between closed or open tube. It would mean that the impact of the water molecules confined inside the channel, if any, is averaged out by that of the physisorbed or chemisorbed water outside.

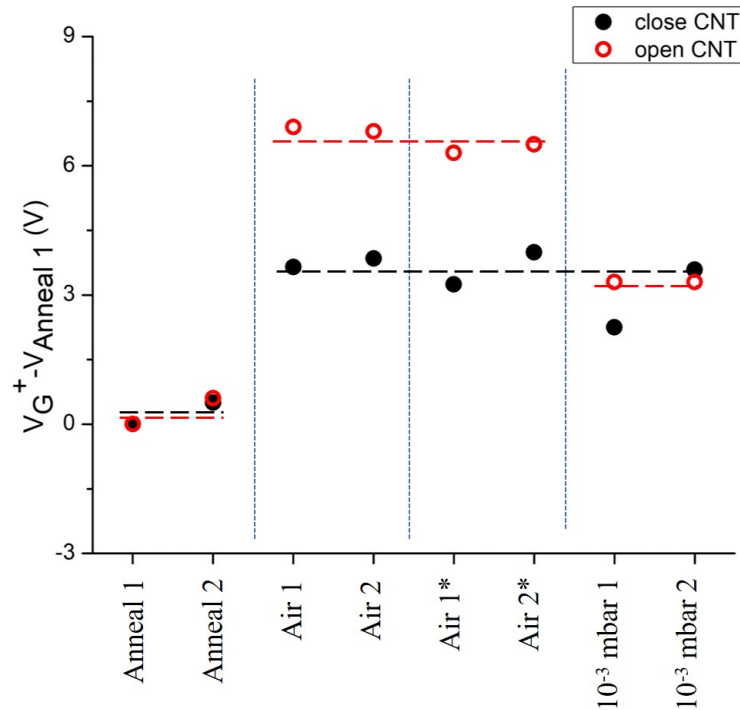


Figure 6.22: Comparison of air partial pressure effect on the close and open individual SWCNT. Symbols are experimental data, horizontal and vertical dashed lines are guided to the eye

The difference in behavior between the close and open SWCNT becomes clear as soon as the CNTFET is placed under a secondary vacuum at room temperature: when the tube is closed, the vacuum causes no significant change, whereas when it is open, V_G^+ is shifted towards lower values. From this observation and assuming that the secondary vacuum eliminates the physisorbed water, it can be stated that the desorption of the physisorbed water located outside the tube makes no real change in V_G^+ while that of the molecule confined inside the open tube makes a much more consequent change.

Finally it can be seen, in both close and open tube situations, vacuum annealing causes a significant shift in V_G^+ towards lower values compared to the situation in vacuum at room temperature. It means that the annealing treatment eliminates the "same" water in both cases, that is the silanol groups, and allows the CNTFET to return to its "reference" state. This repeatable evolution, therefore, indicates that the presence of silanol surface groups on the substrate, at least in the SWCNT vicinity, has a strong impact on our CNTFET electrical behavior. To sum up, the most important impact of water is linked to the presence of the water molecules confined inside the tube and of the silanol groups at the surface of the substrate.

In the case of close SWCNT, our observations are similar to most of the so far reported works about air partial pressure[193] or humidity[211] impact outside of the CNT, which can be observed as the shift of the gate threshold voltage mainly because of the silanol group

forming on the substrate.

6.3.2 After evaporation of a liquid water drop

In section 6.2 (Figure 6.19), we have shown that exposing to liquid water our CNTFET when the tube is close is reversible: after water evaporation with a dry air flow the conductance turns back to its original (before wetting) state. The same test carried out on CNTFET with open tube leads to the same conclusion. Indeed, we can see in Figure 6.23 that the level of V_G^+ is not changed after water evaporation. It means that evaporating the liquid water just using a dry air flow does not empty the tube, the influence of drying is to remove outside physisorbed water. It is in line with simulation work in the literature [53, 29] that showed a preference for water to be inside.

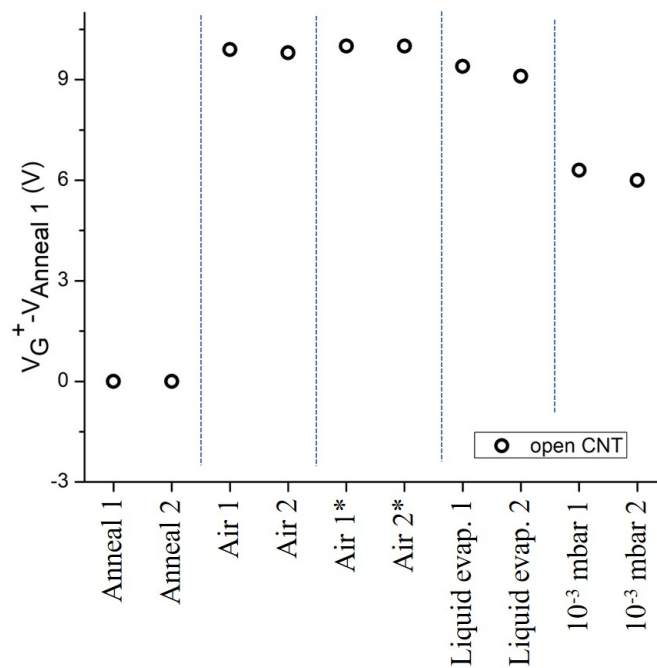


Figure 6.23: An open 5 μm long CNT treated under different conditions including after CNT is exposed to liquid water and evaporated

6.3.3 Comparison of different CNT metallicities

The same protocol is tested on FET made of SWCNT with different electronic properties, i.e. semiconducting and semi-metallic. Data obtained on opened semiconducting and semi-metallic CNTFET with 5 μm long CNT are presented in Figure 6.24. Again, we observe the same trends corresponding to open individual SWCNT (three plateaus after annealing, in air, and under vacuum, respectively) independently of their metallicity. This confirms that even though CNTs have different metallicity they exhibit the same response to water adsorption. Therefore, the effect of water (adsorbed and confined) on a CNT is independent of the density of states of the tube.

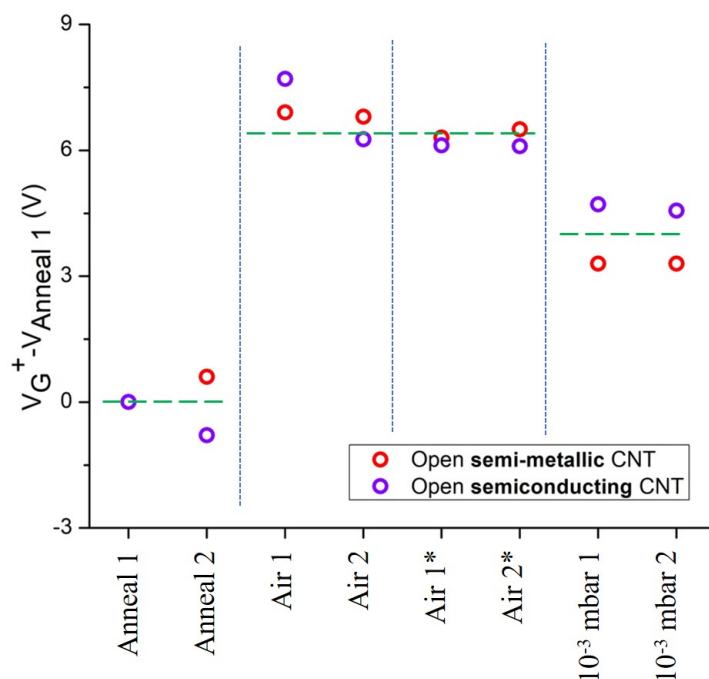


Figure 6.24: Impact of the CNT metallicity on the evolution of V_g^+ as a function of the hydrated state: semi-metallic and semiconducting open individual SWCNTs with $5 \mu\text{m}$ long. Symbols are experimental data, horizontal and vertical dashed lines are guided to the eye

6.3.4 Case of Bundle or MWCNT

So far we focused on the study of nanotubes identified as "individual" and "single wall", as discussed in section 6.1.6.1. Data obtained on CNTFET that we categorize as MWCNT or bundle (from the breakdown current) are reported in Figure 6.25. The behavior of two CNTFETs made of different CNT having the same metallicity is presented when the tubes are closed or open. In these cases, and whatever the exact nature of the CNT, we do not observe any significant change with the presence of water whether it is chemisorbed outside the tube or physically confined inside.

Liu et al. showed that CNTFET is made of DWCNT or MWCNT, the measured electronic properties are those of the external wall[255]. We can thus assume that in the case of an MWCNT, the conductivity of the external wall is not influenced by the presence of water confined inside the central channel. The underlying hypothesis is that the water and carbon interaction is either short-distance or screened by the innertube(s). In the case of a bundle, the structure of nanotubes packed together yields additional adsorption sites located in the space between the tubes. Because the bundle can include tubes of different diameters, together with impurities, one can expect that the geometry of the interstitial adsorption states is complex, making a precious experiment difficult. The simplest explanation, also unprovable in the present case, would be that this diversity of configurations means that, only one average behavior can be observed.

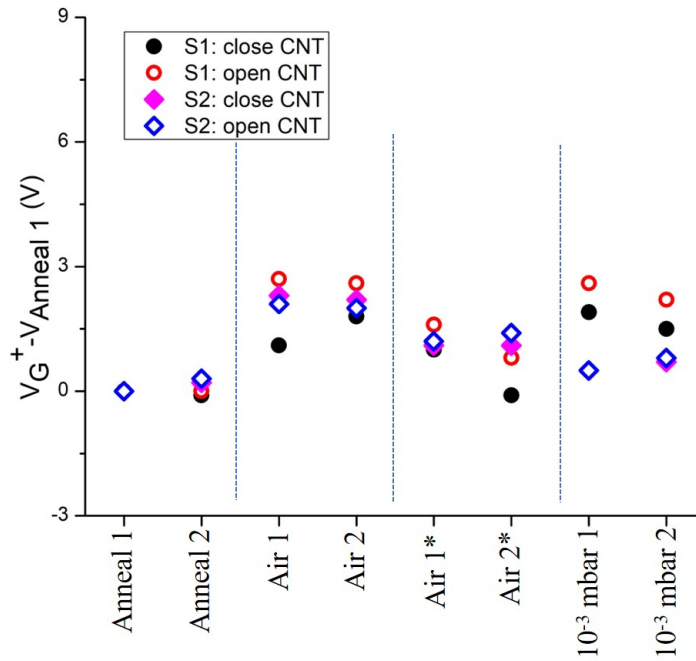


Figure 6.25: Comparison of close and open cases for two different CNTFETs with same apparent metallicity made of either a bundle or a MWCNT

6.4 Desorption of water under vacuum

When working with individual closed or open SWCNT, we have seen in the previous section that water adsorption is spontaneous whether it is inside or outside of the tube. Here, we attempt to understand the desorption process by exposing the annealed CNTFET to air and then to different vacuum levels.

6.4.1 The effect of pressure

The impact of vacuum is tested between 10^{-1} to 10^{-3} mbar. The first response is measured as soon as the desired vacuum is reached. Then, it is recorded upon time, i.e. every 30 minutes. When it is stabilized, the pressure is decreased to a lower level.

Two cases are studied here:

- i) A CNTFET made of a 5 μm long opened SWCNT,
- ii) A CNTFET made of the 25 μm long opened SWCNT. Here, it is possible, thanks to the design of our FET to measure the change in the electrical response between several electrodes, i.e. on sections of the tube with different lengths.

Data obtained on both FETs are reported in Figure 6.26a where it can be seen that there is no significant difference between them. The general trend is that the change in V_G^- is not instantaneous, as there is always a slight jump between the 1st and 2nd measurements separated by 30 min. We also clearly observe a slight decrease in V_G^- when the vacuum reaches 10^{-1} mbar and that it is not significantly modified when going down to 10^{-2} mbar. Then a larger decrease is observed when reaching 10^{-3} mbar.

No clear difference is seen between both CNTFETs, thus indicating that the CNT length has

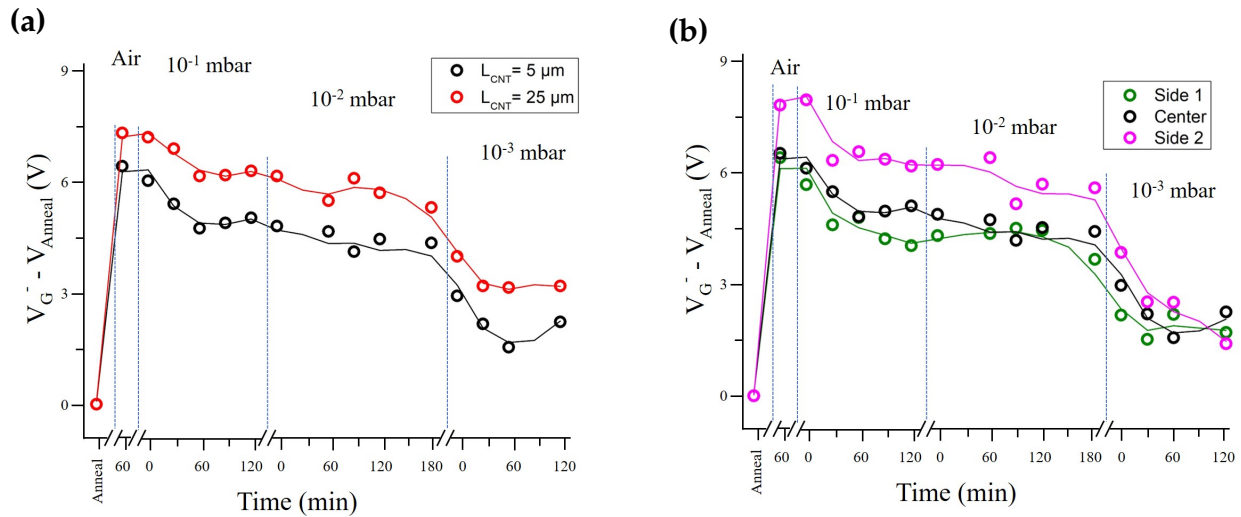


Figure 6.26: Water desorption as a function of the level of vacuum. Symbols are experimental data, horizontal solid and vertical dashed lines are guided to the eye: (a) water desorption from CNTFET with different channel lengths, (b) water desorption for the same channel length of CNT near to open sides and in the center

no impact on water desorption.

Indeed, there is no prior reason why the electron properties of the CNTFET should vary according to the length of the tube being probed and the surface condition of the substrate, which can be assumed to be homogeneous throughout the tube.

On the other hand, we could have imagined that the desorption of water confined within the tube does not take place homogeneously and, consequently, that the response of the CNTFET depends on the part being probed. This is clearly not the case. The most reasonable hypothesis is that each time a water molecule is extracted from the channel, the remaining ones reorganize themselves homogeneously.

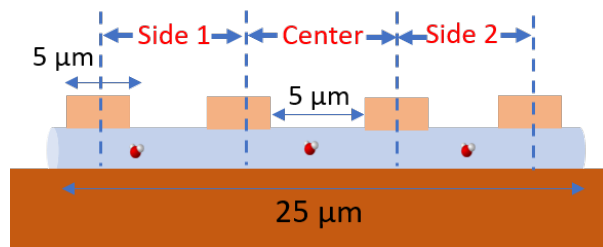


Figure 6.27: The schematic of measuring water desorption on different sections of a same CNTFET device

This observation is consistent with the instantaneous adsorption already observed which suggests an important free enthalpy decrease in favor of water adsorption and consequently a large free enthalpy step to be overcome during desorption; this entropy-driven process is a reason for an easy re-homogenization after each desorption. In other words, a large barrier exists for extracting from the CNT, but not for diffusion of molecules inside.

The data reported for the CNTFET made of the $25 \mu\text{m}$ long tube and measured at different sections is also quite informative (Figure 6.26b) and consistent with results reported in Figure 6.26a. (nb: to make clear the different sections, a schematic representation is proposed in Figure 6.27). It means that this long tube is impacted by the various type of adsorbed

water in a rather homogenous way. As far as water is confined inside the tube is concerned, the removal of a given quantity of water molecules causes a reorganization of those which remain homogeneously distributed/structured throughout the length of the tube.

So based on what is reported in Figure 6.22, the evolution observed in Figure 6.26a can be interpreted as follow:

- 1) Desorption of external physisorbed water at 10^{-1} mbar (very small effect)
- 2) No further desorption at 10^{-2} mbar (no more water to be desorbed)
- 3) Desorption of the water confined at 10^{-3} mbar
- 4) Dehydroxylation of the silanol groups under annealing.

The desorption of the water physisorbed and chemisorbed outside of the CNT is in line with the literature, as Kim et al., reported that physisorbed water can be removed easily at room temperature while chemisorbed water can be removed at 200 °C under vacuum[193]. However, it is quite well known that some types of silanol groups can be removed at 200 - 400 °C temperature ranges, while all different types of formed silanol groups can only be removed completely in the temperature ranges 400-1200 °C[256]. Our annealing process let us fuse CNT in such high temperatures under vacuum to remove the silanol groups formed around CNT.

6.5 Conclusion

The data reported in this chapter constitute a large part of my Ph.D. work. They have required a great deal of testing, as it is both time-consuming and difficult to manufacture CNTFETs made from an isolated tube, and rare to obtain properly functioning ones made only from an SWCNT. Whenever the CNTFET can be manufactured and responds satisfactorily, i.e. level of conductivity and shape of the I_{sd} vs V_G curve, to an initial measurement in air or in vacuum, the whole series of measurements must be first carried out without knowing whether the tube is a SWCNT or a MWCNT, or even a bundle. We have to check the opening process to find out.

Nevertheless, we have been able to collect sufficient reproducible data on several CNTFETs made of individual SWCNT and compare the results before and after opening the tubes.

Our main conclusions are:

- 1) It is impossible with the procedure used in our work to obtain reproducible and consistent outcomes when the CNTFET is made of MWCNT or bundles. This proves that the impact of water on the behavior of our FETs can only be analyzed when they are made up of individual SWCNT, which we can hope, given the synthesis method, are all of comparable diameters. In other cases, the diversity of tubes and hence their properties is too large to yield reliable conclusions.
- 2) Comparison of the behavior of CNTFETs with closed or open tubes leads to conclude, as it has been already reported, that the filling of the tube is rather fast. This time is not measurable using our protocol but it is for sure shorter than one minute or two.
- 3) Comparison of the behavior of CNTFETs with closed or open tubes leads to a clear distinction between the effect of the water chemisorbed on the surface of the substrate, most probably in the form of silanols, in the tube external environment, and of the water confined

in the internal channel of the tube. Results suggest that the impact of the silanol groups even covers that of the confined water molecule.

4) Studying the desorption of water as a function of the vacuum applied shows that there is a smaller effect of water physisorbed outside the tube, whilst it is not possible at this stage to specify whether it is on the surface of the substrate or on the tube wall.

5) Studying the desorption of water as a function of vacuum, the SWCNT length and the section of the tube indicate that the removing of the confined water molecules is more difficult than their filling and that it proceeds homogeneously, i.e. as soon as some water molecules leave the channel, they likely re-organize homogeneously throughout the length. This conclusion is fully in line with the principles of a filling process governed by entropy.

Positioning of the different water states (physisorbed, chemisorbed, confined) on the tube is presented in Figure 6.28. The process of water adsorption and desorption on the closed and open tube is schematically presented in Figure 6.29.

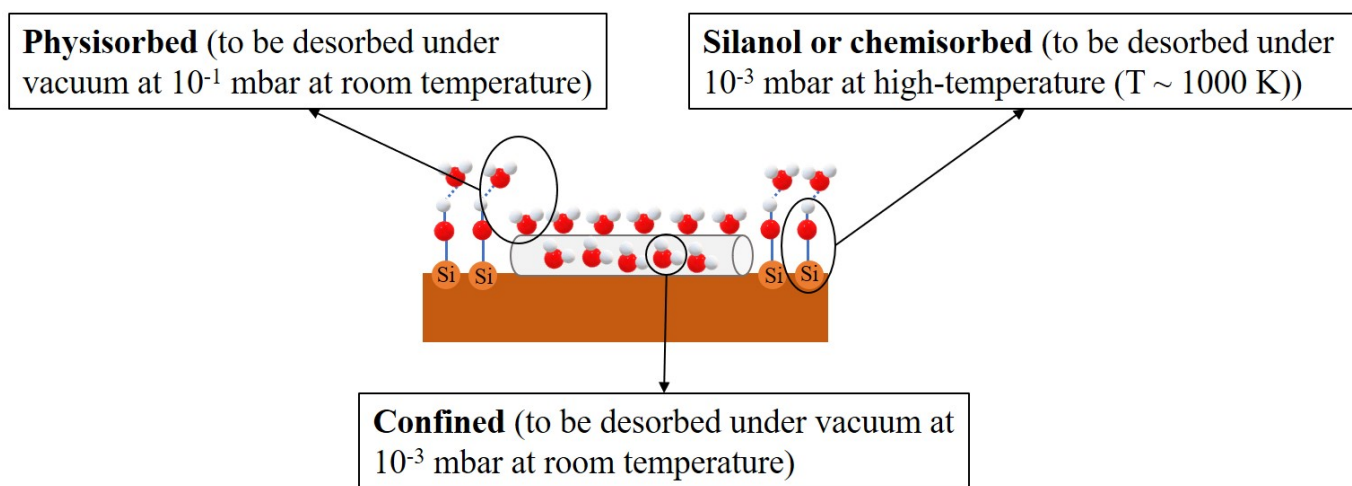


Figure 6.28: Scheme of different types of water forming

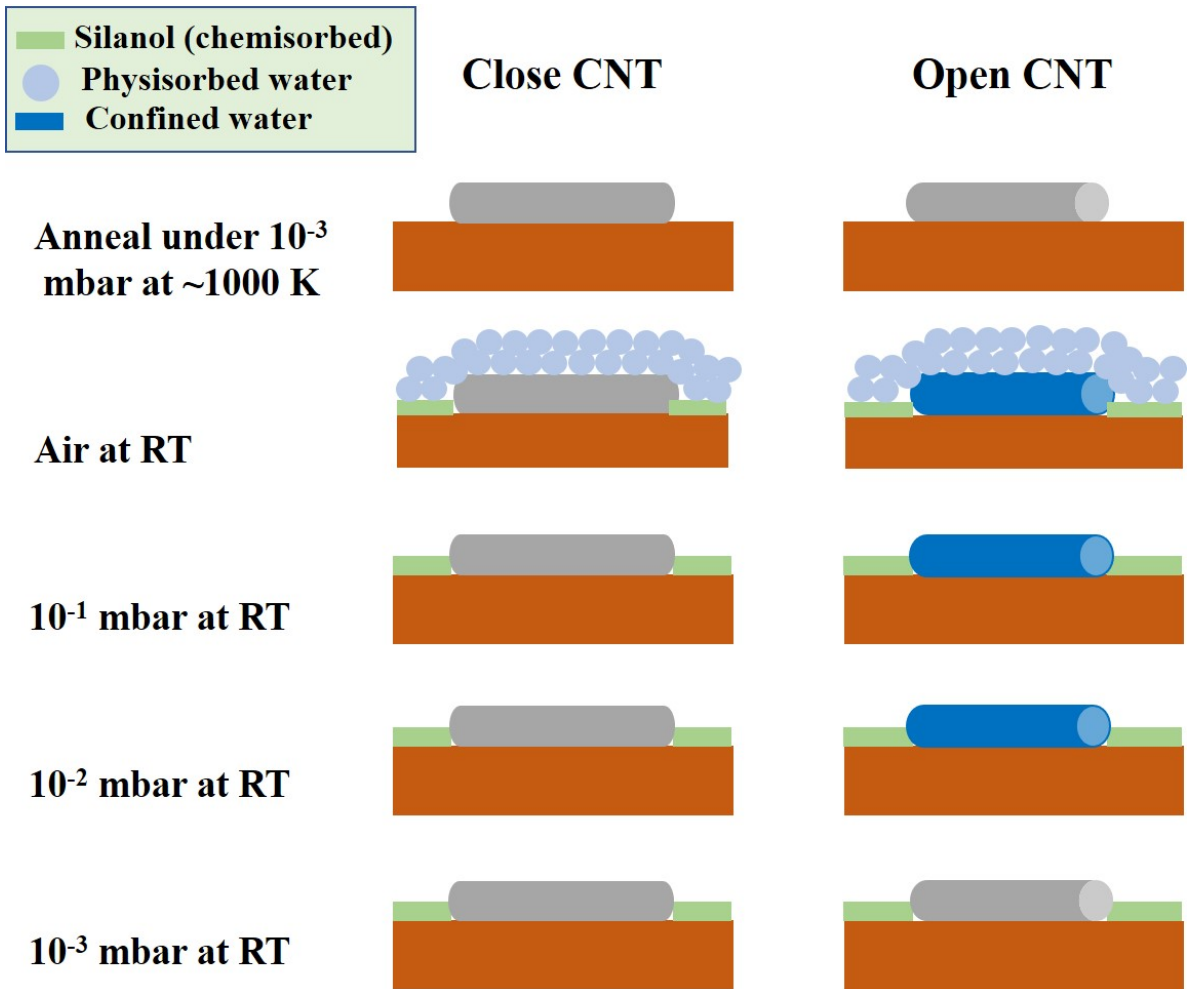


Figure 6.29: The schematic of water adsorption/desorption process for the close and open CNT

Prospectives and General conclusion

Being the main liquid of living organisms and being essential to daily human life, water has been studied over years on macro and microscales. Various phenomena such as hydrodynamics (continuum flow) on the macroscale, capillary, cavitation, and condensation on the microscale have been the subject of thousands of studies. However, investigating the behavior of water on the nanoscale remains challenging. Thanks to the utmost recent advances made in the field of nanotechnology, it is becoming increasingly feasible to build micro or nanosystems which make it possible to access the response, for example, electrical or optical, of isolated nanometric objects interacting with water and to deduce the behavior of water at this scale. Such work has both fundamental and applied benefits and for those reasons recently gained popularity, particularly in the field of nanofluidics. It was in this context that the objectives of this thesis were set. Considering the expertise and the long-term research projects developed in the team I joined, this work was defined around two axes:

- (i) to be able to produce a sealed μ -device inside which it should be possible to inject liquid water or control its partial vapor pressure;
- (ii) to study the effects of the presence of liquid or vapor water on a field-effect transistor (FET) whose channel is made of an individual single-walled carbon nanotube.

The first is a technological project, the second a more fundamental research objective. The μ -device developed in axis 1 is the first step toward the fabrication of a sealed Lab-on-Chip whose functioning is based on the nanofluidics properties of SWCNT under a controlled environment. The methodology developed must be versatile enough to be applied to several types of Lab-on-Chips, in particular those that can be used for electrical or electromechanical measurements. The material selected for such duties could thus be employed in different conditions: liquid, partial gas pressures, and vacuum, and at various temperatures, more particularly as low as a few Kelvins. In addition, its bonding process should not require a too high temperature or the use of any chemical or plasma activation. Finally, it is essential that the selected material has sufficiently long durability so that the Lab-on-Chip can be used to carry out as many measurements as possible. Therefore, most of the so-far developed bonding methods cannot meet all these requirements together.

In the second part, we aimed at studying the interaction between water & a single SWCNT based on the CNT's electrical response. As we were especially interested in investigating the impact of the water molecules confined inside the CNT on the electrical behavior of the SWCNT, we needed to find a method to distinguish water adsorbed outside from that confined inside. Even though some work about water adsorbed outside[193, 257] and water confined inside[224] the CNT has already been published, more experimental data are requested. Studying the interaction between water and CNT is quite challenging, and should be explained from different points of view, such as if we have to deal with (i) an individual CNT or ensemble of CNT and (ii) a single-wall (SW), a multi-wall (MW) or a bundle, (iii) CNT with different metallicity, ie. metallic, semi-metallic or semiconductor as well as (iv) the diameter of the CNT which we know from the theoretical work to be a key issue. All these parameters need to be carefully considered .

The main results obtained can be summarized as follows :

In the case of our μ -device, we selected an epoxy-assessed photoresist (SU-8). It allows us to fabricate and assemble a tight device with the smallest possible thickness of 35 μm and to quantify its performance. We show that micrometric walls made of SU-8 resin exhibit liquid water pressure leak tightness from 1.5 bar up to 5.5 bar and no porosity even after 2 months of aging. We also found that the SU-8 wall can operate under a secondary vacuum with neither degradation of the vacuum nor outgassing nor liquid water or gas permeability. Moreover, the fabrication process we propose requires neither aggressive chemical nor high temperature nor high energy plasma pre-treatment. It thus opens a new perspective to seal μ -device when sensitive surfaces or materials such as CNT are used.

In the case of our investigation on the interaction between water and CNT, we observed that the electrical response of a FET in which the channel is a SWCNT is very sensitive to water, and hence that such FETs can be an excellent tool to study all different processes of water adsorption. We show that a clear distinction could be made between CNTFETs made of individual SWCNT to those made of MWCNT or even bundles. We also perceived a clear difference between these two types of CNTFET, since only the ones made of individual SWCNT could yield reproducible and consistent outcomes. Using the breakdown current protocol allowed us to open the tube and compare the response of the FET before and after opening. Thanks to the reproducible data obtained in the case of FET made of an individual SWCNT while it was subjected to various conditions (liquid water, air, vacuum, and current annealing), we were able to clearly distinguish the effect of the water confined inside the nanotube from that adsorbed outside. It can then be concluded:

- 1) water adsorption outside and inside the tube is spontaneous
- 2) there are 3 different water states: (i) chemisorbed on the surface of the substrate, i.e. likely silanol groups, (ii) physisorbed on the external side of the tube wall or the substrate, and (iii) confined inside the channel.
- 3) there is no impact of the CNT metallicity on water adsorption.
- 4) full water desorption under different vacuum at room temperature takes hours
- 5) desorption proceeds homogeneously i.e. as soon as some water molecules leave the channel, they re-organize homogeneously throughout the length.
- 6) our CNTFET made of MWCNT or bundles gave no consistent and reproducible data since, most supposedly, in the case of DWCNT or MWCNT the response of the FET comes from the electrical conductivity of the outermost wall which is not impacted by the water

confined in the central channel. The situation is much more complex if the FET is made of a bundle since some tubes can be open, some others not. This proves that the impact of water on the behavior of our FETs could only be analyzed when they are made of individual SWCNT. In other cases, the diversity of tubes and hence their properties are too large to yield reliable conclusions.

Both assigned objectives have been achieved although, some stays to be reached in both cases. One of the main steps regarding the application of the μ -device can be testing its performance while sealing the nanomaterial and applying it to different conditions specially cryogenics.

In the case of the CNTFET, first and foremost, correlating the behavior of our CNTFETs with the SWCNT diameters should be made possible, as it is well known (Chapter 2) that the structuring of the confined water is highly dependent on it. Checking whether this structure can have a discriminating impact on the FET's electrical behavior could be a major step forward. It could also be envisioned more precise monitoring of desorption kinetics. Likewise, the protocols developed in our work could also be followed by modifying the temperature of the FET and precisely controlling the vapor pressure. Obtaining a whole set of isothermal measurements should provide valuable information on the dynamics of confined water and on phase transitions; and if any whether they have structural or dynamical origins. Whatever they are, the results obtained should be quite useful for the development of the electro-mechanical nano platform project which aims at investigating the dynamics and structure of water confined inside a single-walled carbon nanotube.

CNTFET device fabrication protocols

The CNTFET sample fabrication protocols are explained. These include the creating of the optical marks, catalyst and metal contact deposition.

A.1 CNTFET sample fabrication

Protocol 1: Optical marks

Optical marks on SiO_2/Si substrate: Lithography patterning and ICP etching:

- SiO_2 (300 nm)/ Si 4-inch wafer is cleaved in the dimension of 2 cm x 2 cm
- Cleaning substrates: Sonication in acetone for 5 min, rinsed subsequently with isopropyl alcohol (IPA) and deionized (DI) water, then dried with N_2
- Dehydration of the substrates at 110 °C for 5 min
- Photoresist AZ5214 EU is poured on the hot sample directly placed on the spin coater
- Spin coating: 6000 rpm for 30 sec
- Prebake the substrate at 120 °C for 1 min (then wait for cooling down to room temperature)
- UV exposure: Mask used to expose optical marks patterns. Substrates are exposed for 2 sec to a UV lamp with a power of $8mW/cm^2$ (wavelength 365 nm)
- Post exposure bake (PEB): on the hot plate at 120 °C for 2 min (cool down to room temperature)
- Flood exposure: UV exposed without mask

- Development: sample developed in the beaker filled with AZ726MIF developer for 1 min, then rinse with DI water, N_2 flux drying. Check (with an optical microscope) if optical marks are properly developed (Figure 6.1 first step).

Protocol 2: Catalyst pattern deposition

Catalyst pattern deposition after preparing catalyst solution:

- Each time the catalyst solution is sonicated for 10 min before using
- The catalyst and S1818 photoresist mixture is prepared (in the volume ratio of Catalyst (3)/S1818 (20)) and mixed with an agitator at 2000 rpm for 1 min
- Optical marks etched substrates dehydrated for 5 min at 120 °C
- Catalyst mixture poured on the hot sample on the spin coater
- Substrates spin coated at 2000 rpm for 20 sec
- Substrates prebaked at 120 °C for 1 min
- If needed edges are removed with using acetone on a cotton bud to obtain a better contact during UV exposure
- Substrates are exposed using the catalyst patterned mask for 2 sec to a UV lamp with a power of $8mW/cm^2$ (wavelength 365 nm)
- Substrates are developed in the AZ726MIF photoresist developer for 1 min, followed by DI water rising and N_2 flux drying

Protocol 3: Patterns for metallic contact deposition

After doing the preliminary selection of the CNT and its location, the bilayer lithography process is done to deposit the metal contacts onto the CNT. We deposited six metal contacts with channel length $5\ \mu\text{m}$ and contact length $5\ \mu\text{m}$ to be able to measure the CNT resistance versus channel length dependence and the contact resistance between metal and CNT.

- Substrates dehydrated for 5 min at $120\ ^\circ\text{C}$ on the hotplate
- Lor5A poured on the hot samples on the spin coater
- Samples spin coated at 3500 rpm for 30 sec
- Samples prebaked at $180\ ^\circ\text{C}$ for 1 min (then cooled down to room temperature)
- AZ5214EU poured on the cooled sample and spin-coated at 6000 rpm for 30 sec
- Samples prebaked at $120\ ^\circ\text{C}$ for 1 min
- Samples exposed to UV lamps for 2 sec with a power of $8\text{mW}/\text{cm}^2$ (wavelength 365 nm)
- PEB at $120\ ^\circ\text{C}$ for 2 min
- Flood exposure without a mask for 40 sec
- Development in AZ762MIF for 60 sec (check with optical microscopy if patterns are developed well)

Small diameter CNTs synthesis via CVD

Here, our objective is to optimize the synthesis parameters required to obtain the CNTs with a diameter below 1.4 nm. These dimensions are important in our project in order to study the properties of water confined at the nanoscale.

In order to achieve our goal, we started from a previously developed growth process in the team, the growth of aligned SWCNTs by so-called kite growth on Silicon wafers. This recipe however synthesizes bigger diameter CNTs in the range of [1.5-2.5] nm. We then carried out CVDs with different catalyst mixtures and CVD parameters to synthesize CNTs with the required dimensions .

SEM is used to observe the growth density, length, and orientation of the CNTs grown from the catalyst pattern. Raman and AFM are used to characterize the diameter distribution of CNTs, both in the catalyst pattern and outside when possible.

B.1 Sample fabrication

The CNTs are synthesized on 90 nm SiO_2 on top of Si substrate. We choose this material because it facilitates the characterization of the CNT by Raman scattering[258].

Firstly, optical marks are created on the substrate using photolithography and ICP etching (as explained in Protocol 1 Appendix A). Their role is to facilitate the characterization of CNT by locating them on the surface. After etching the optical marks, the substrates are strongly cleaned with sonication in an acetone bath, followed by dipping in RPG solution at 80 °C for 1 h. This step is important in order to clean the substrate surface from resist residue, thus preventing the growth from contamination and improving reliability.

Different catalyst solutions are prepared by mixing Fe, Ru, SiO_2 in methanol. Methanol is selected to dissolve the metallic salts to prepare a catalyst solution because of its polarity. The methanol is selected in a controlled amount also because of its compatibility with the photoresist without changing its properties such as viscosity. The catalyst solutions are later mixed with S1818 photoresist and patterned by photolithography on the substrate (as explained in Protocol 2 (Appendix A)).

The Chemical Vapor Deposition (CVD) method is used to synthesize of CNTs. The CVD process starts with a decomposition of the ethanol (carbonaceous precursor) on the catalyst particles. Ethanol is a widely used precursor because it employs different growth conditions and controls water moisture in the furnace. Meanwhile, the water formed in the ethanol decomposition process is in controlled amount which is necessary for encapsulating the catalyst particle by carbon atoms to form the CNT. Compared to other precursors it is more reproducible in the way of controlling water moisture in the CVD furnace. Then it is transformed into the furnace by an inert gas (Argon) at a temperature of around 900 °C. The CNTs then grow on the silicon substrate. The growth process is called "kite" growth[259]. This process happens in two steps: (i) based on the temperature gradient on the substrate surface and inside the quartz tube in the furnace, which enhances the CNTs to grow vertically and (ii) controlled gas flow is applied to keep laminar flow over the quartz tube to direct CNTs horizontally onto the substrate.

CVD is a complex synthesis process with numerous input parameters and elements.

The components of the CVD equipment are:

- A three zones tubular furnace to ensure temperature homogeneity during synthesis. This homogeneity is achieved by means of three resistors arranged around the furnace.
- A quartz tube to deposit our substrate.
- A magnetic arm for positioning of the sample in one of the zones of the furnace.
- A steam of ethanol gas, the carbon source for the synthesis.
- A flow of argon gas, which has two functions: it allows the ethanol to pass into the gas phase in one of the valves, and it also decreases the flow of Carbonaceous gas while keeping the total flux equal.
- A steam of hydrogen, which acts as a reductant for the catalyst oxidized during resin calcination.
- O_2 and H_2O sensors are used to monitor the contents of the chamber prior to and during the synthesis. The H_2O sensor monitors the synthesis itself through the reaction:

$$C_2H_5OH \rightarrow 2C + H_2O + 2H_2$$

The main CVD parameters which are decisive for the synthesis of CNTs, in particular, their diameters are temperature in the furnace, the gas flux, and humidity.

Before starting the synthesis the substrates are calcinated in the air at 700 °C for 5 min starting from room temperature with a heating rate of 15 °C/min. This step burns the photoresist, which is used to pattern the catalyst and removed as much as water possible from the CVD furnace. The synthesis parameters are then entered, including gas flows, carbon precursor, temperature, and synthesis time. Once the sample has been placed in the right position, the oven is ramped up at 15 °C/min up to 900 °C and kept at 900 °C for 30 min. Finally, once synthesis is complete, the furnace is left to cool down and gradually reduce the gas flow to gently deposit the CNTs on the substrate, with an orientation perpendicular to the catalyst patterns.

B.2 Characterization of as-grown nanotubes

SEM and Raman are the two main tools used to characterize the CNTs. SEM is used to observe the length, density, and orientation of the CNTs grown from the catalyst pattern and the zone in which the CNTs have been grown. Raman spectroscopy is used to characterize the diameter distribution, mainly in the catalyst pattern. AFM is also used to correlate the diameter of the CNTs grown from the catalyst pattern with the diameter measured with Raman in the catalyst pattern.

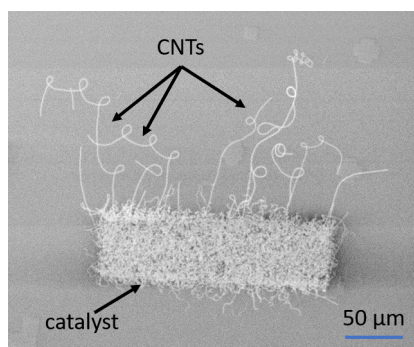


Figure B.1: SEM image of the CNTs grown on the substrate from the catalyst pattern

SEM is used to characterize materials with high resolution and efficiency. The electron beam emitted from the cathode tip is accelerated and focused by the anode and magnetic lens. The beam scans the sample and the secondary electrons are produced by the electron bombardment and collected by the secondary detector (SE)[260]. The grayscale image is produced by collecting SE signals. SEM images contain the surface topography of the material and local surface charges. The acceleration voltage, dwell time, and magnification are the main factors that significantly affect SE emission. It was observed based on the contrast arising from different conductivity or band-gaps of the SWCNT placed on the substrate, it can be observed in SEM. The substrate plays a role in evaluating the physical properties of CNT such as metallic or semi-conducting[261, 262]. It is challenging to image the smaller diameter CNTs below 1 nm, owing to the finite size of the beam. This technique does not reveal if the CNT is SW, MW, or even if bundle.

AFM is a widely used technique to measure the surface morphology of nanomaterials with subnanometer accuracy[263]. It has been used to measure CNT and to approximate their diameter[264]. It can give information about the vertical dimension of the object, however, the measured height is often different from the actual height due to the interaction of the AFM tip with the sample. This method does not as well allow us to identify if the CNT is SW, MW, or bundle. Figure B.2 presents the AFM image of the CNT grown from the Fe & Ru catalyst and its diameter is extracted from the measured height.

When a sample is illuminated with intense monochromatic incoming photons are either transmitted, adsorbed, or scattered. Raman spectroscopy focuses on the scattering of photons. Raman scattering is an inelastic scattering, which means the energy of the scattered photons differs from that of the incident photons. Due to the vibrational mode of the probed material. The frequency modification is called the Raman shift:

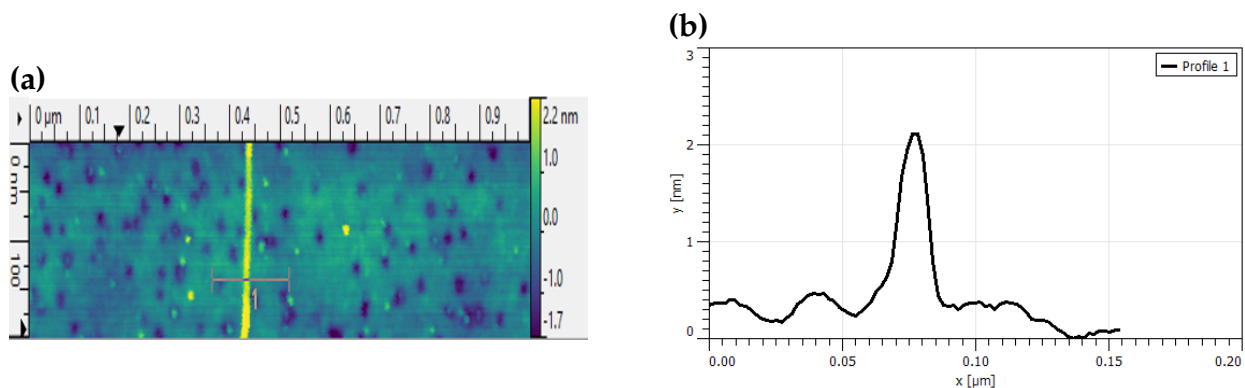


Figure B.2: Diameter approximation of CNT grown from catalyst pattern: (a) the AFM observation of the CNT grown from Fe & Ru catalyst, (b) the extracted diameter of the CNT from AFM picture

$$\nu_s = \nu_0 - \nu_{vib}$$

$$\nu_{as} = \nu_0 + \nu_{vib}$$

Here, ν_s and ν_{as} are frequency corresponding for Stokes and anti-Stokes scattering, ν_0 frequency of photons, and ν_{vib} is the frequency related to vibrational mode.

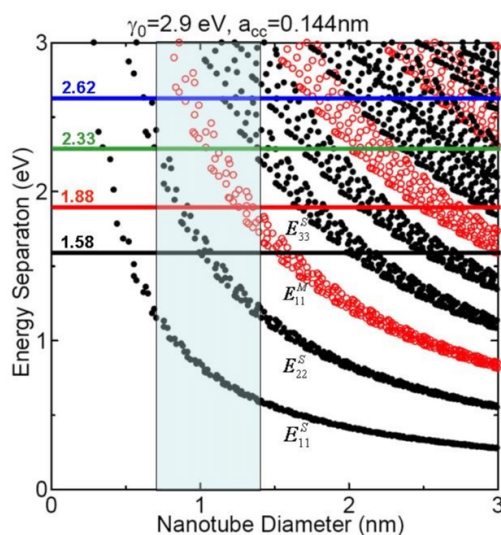


Figure B.3: Kataura plot (From [265])

In this study, we will be using resonant Raman scattering, which is a special case that occurs when the wavelength of the exciting radiation is close to that of an electronic transition in the material under study. The resonance condition greatly enhances the measured signal, which is necessary for the study of material with low cross-section such as CNT.

Each nanotube structure (e.g. chirality) has a given set of electronic (thus excitonic) transitions, allowing to link optical resonance to a nanotube diameter. This is the basic of the so-called Kataura plot (Figure B.3). Regarding the conductive or semi-conductive nature of CNTs, the Kataura diagram illustrates the usefulness of using lasers with different wavelengths to excite them. The diagram shows each laser has energy that can observe a limited portion of the CNT, depending on its diameter. This explains the use of three different lasers (532 nm, 633 nm, 785 nm) each with different energy, to observe CNTs of different diameters. As a result, this spectroscopy can observe a sufficiently wide range of CNTs with different

diameters without discontinuity.

In the Raman spectra measure experimentally, we can identify the following vibrational modes of SWCNTs. RBM mode, G and D band. Radial breathing mode (RBM) is the most characteristic band for SWCNT, this band corresponds to a vibration mode similar to a CNT “breathes”. From the frequency of this band, the diameter distribution can be calculated[246, 247].

G band is the vibrational mode of $C - C sp_2$ bonds. It is used to determine nanotube purity[246, 247]. D band comes from the mode of vibration of the hexagon. This band is associated with the defects in the structure of a CNT[246, 247].

- The peak between 100 and 300 cm^{-1} : corresponding to Radial breathing mode or RBM peak. This peak is used to determine the diameter of the CNT (in this work we mainly focused on this peak)
- Peak at 520 cm^{-1} corresponds to the SiO_2 Raman peak, presents because of the substrate.
- Peak at approximation 1300 cm^{-1} corresponds to peak D, a $C - C sp_3$ Raman band corresponding to defects in the CNT.
- Peak at around 1600 cm^{-1} corresponds to the G peak, the Raman band of graphene and therefore of the $C - C sp_2$ bond[266].
- Peak at around 2650 cm^{-1} corresponds to the G' band, also known as the 2D band.

Raman analysis is carried out with Renishaw via a confocal Raman microscope. The spectrometer is used with a confocal microscope and spectrum analysis software, WIRE4.1. We used three different laser wavelengths: 532 nm , 633 nm , and 785 nm . These three lasers enable us to observe all CNTs within an analysis perimeter of around 1 nm diameters.

Table B.1: Raman spectroscopy parameters for each laser type

Wavelength (nm)	532	633	785
Analysis frequency range (cm^{-1})	100-1750	100-1750	100-1750
Diffraction grating (ligne/mm)	2400	1200	1200
Exposure time (s)	0.2	1	1
Laser power (%)	100	100	100
Accumulation	2	2	2

After calibration of all of the lasers corresponding to the Si peak with a frequency of 520.4 cm^{-1} , we moved to our sample and choose the area pre-observed in SEM, using optical marks. We carried out line measurements on the center of the catalyst pattern with the highest magnification ($\times 100$) yielding a beam size of $\sim 1\text{ }\mu\text{m}$. The starting point was selected and set then all three lasers run exactly on the same path over the catalyst pattern. The parameters used for different lasers are shown in Table B.1. The baseline is subtracted from the measurement spectra to see the peaks corresponding to the CNT. The spectra show various peaks of varying interest for our study (Figure B.4). Here we mainly focused on the

RBM peak and its corresponding frequency to calculate the diameter of the CNT using the following equation[267, 246] this is an empirical law for CNT on quartz.

$$d = \frac{217.8}{\omega - 15.7} \quad (\text{B.1})$$

Here d is the diameter of the CNT in nm, ω is frequency in cm^{-1} .

The D and G peaks confirm the presence of CNT, where the G/D ratio shows the purity and the presence or absence of defects in our CNT. The higher this ratio the fewer defects in our CNT.

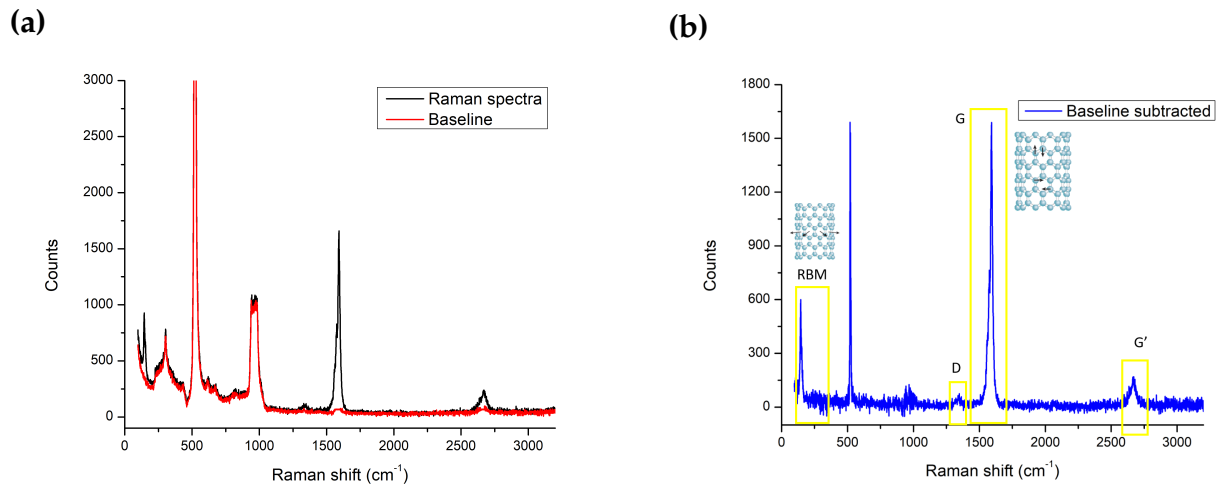


Figure B.4: Raman spectra of CNT: (a) Subtraction of the spectra corresponding to CNT, (b) CNTs Raman spectra

B.3 Results

We tested the impact of catalyst compositions, the concentration of the nanoparticles in the catalyst mixture, CVD flux, and initial moisture concentration in the CVD furnace on the CNTs synthesis

B.3.1 The impact of different catalysts compositions

The catalyst is the most important element in the synthesis of CNTs, and strongly controlling their diameters. We compared the catalyst mixture of Iron (Fe) and Ruthenium (Ru)[268] with Cobalt (Co) and Molybdenum (Mo)[269], which are the most commonly used mixtures to synthesis small diameter CNTs. Figure B.5 shows the diameter distribution of the CNTs growing from two different catalyst mixtures as measured thanks to Raman spectroscopy. It is obvious that the diameter of the CNTs growing from Co & Mo is bigger than the CNTs synthesized from Fe & Ru with an average diameter of 1.5 nm and 1.2 nm, respectively.

The number of RBM peaks are nearly 5 times higher in the case of Fe & Ru which can be related to CNT density. For the same dimension catalyst patterns and with the same measurement steps we observed 164 RBM peaks for Fe & Ru, however 33 peaks for Co &

Mo.

It is also useful to evaluate the percentage of CNTs with a diameter less than or equal to 1.4 nm. In the case of Fe & Ru catalyst the value (77%) is higher than Co & Mo (30%).

Thus, we observed that in the case of using Fe & Ru mixture as a catalyst, the density of the CNTs is higher and the average diameter is smaller compared to Co & Mo.

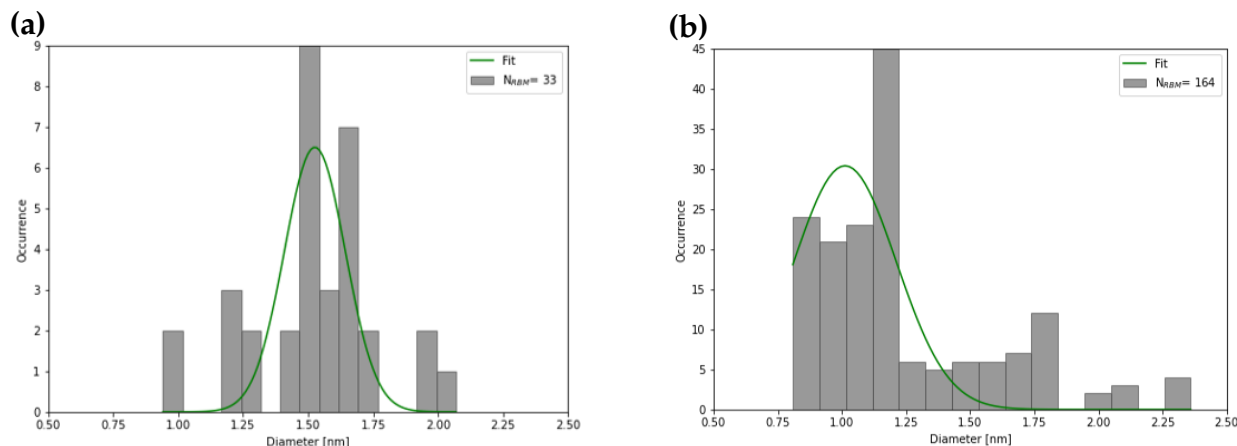


Figure B.5: The diameter distribution of the CNTs synthesized from the different catalysts measured with Raman spectroscopy on the pattern: (a) the diameter distribution of CNTs grown from Co & Mo, (b) the distribution of CNTs grown from Fe & Ru

The observed difference in the CNTs synthesis while using these two catalyst mixtures is unpredictable. Probably by optimizing the growth one can synthesize CNTs with the same dimensions as Fe & Ru from Co & Mo mixture. However, this test allows us to select our direction. Therefore, we selected Fe & Ru catalyst mixture and in the next step, we tested different concentrations of nanoparticles in this catalyst mixture.

B.3.2 The impact of iron concentration on CNT synthesis

The impact of the nanoparticles concentration in the catalyst mixture such as Iron (Fe), Ruthenium (Ru), and also the concentration ratio of Fe to Ru in the mixture is reported. The mixture is prepared from $FeCl_3$ (15 mM), Ru 15 mM, and SiO_2 whose role is to act as chemically inert support to enhance the dilution and to provide a large specific surface area for the catalyst particles. This can provide stability to the particles and prevent their agglomeration during the growth process. However, the concentration of Fe and Ru is modified several times in order to observe their impact on the size of the CNTs' diameters obtained.

We tested different concentrations of Fe in the catalyst on the CNT synthesis. The catalyst solutions are prepared with Fe concentrations of 1.66 mM, 2.5 mM, 5 mM, and 15mM while keeping Ru concentration 15 mM.

In Figure B.6a, we observed that the higher the iron concentration, the greater the average diameters of the synthesized CNT. This trend is confirmed when we look at the occurrence of the CNTs with diameters less than or equal to 1.4 nm for different Fe concentrations. It shows that the diameters tend to be larger as [Fe] increases. However, we also observed that the number of RBMs in the case of very small Fe concentration is lower than once the Fe concentration is more than 5 mM (tested for 16 samples). In other words, the density of

growing CNTs is increasing with increasing Fe concentration in the catalyst solution.

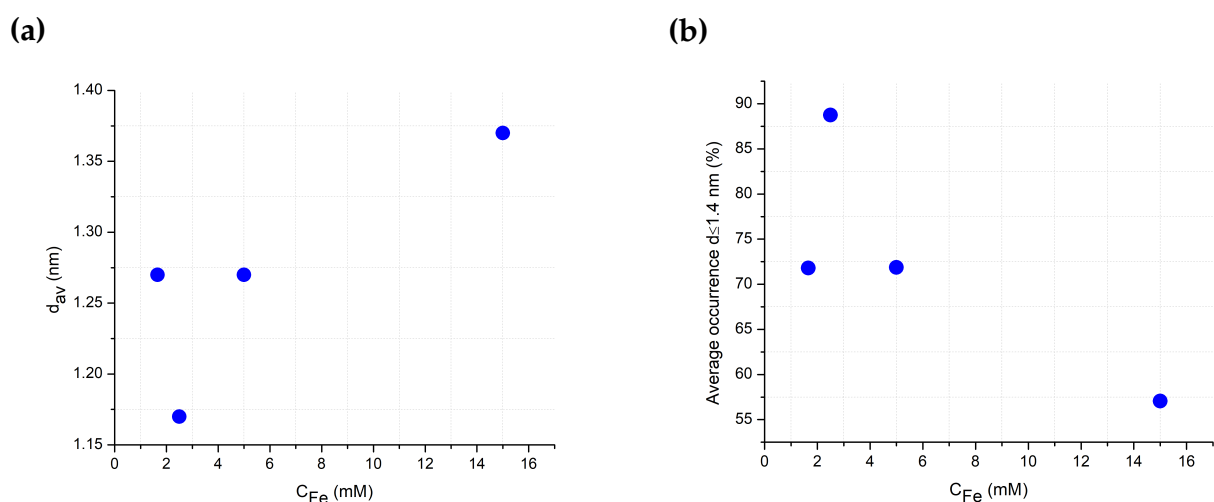


Figure B.6: The impact of iron concentration in the catalyst on the CNTs synthesis: (a) the average diameter of the CNTs for different Fe concentrations, (b) the percentage of the CNTs with diameter less than or equal to 1.4 nm dependence versus Fe concentration in the catalyst

Fe is the main element in the CNT growth, and the increase of the diameter with increasing [Fe] can be related to the process of coalescence of nanoparticles which leads to synthesis bigger diameter CNTs. The increased CNT density means the number of RBM with increasing Fe concentration is related to having more metal particles forming CNT.

B.3.3 The impact of ruthenium concentration on CNT synthesis

The impact of the presence of Ruthenium (Ru) and its concentration on CNT synthesis is tested.

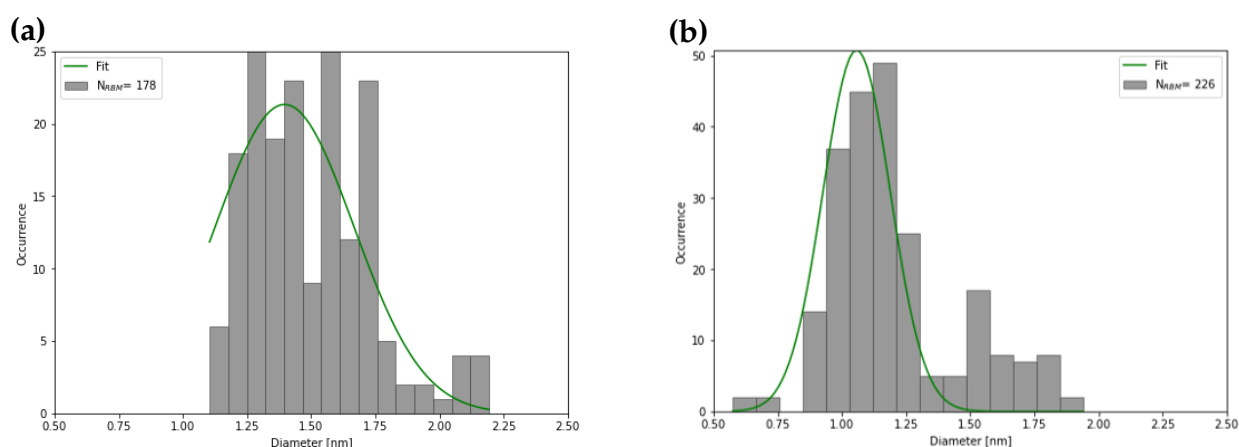


Figure B.7: The impact of the Ru on the CNT diameter distribution: (a) the catalyst without Ru, (b) the catalyst with Ru (15 mM)

Figure B.7 shows the diameter distribution of the CNTs calculated from the RBM band for the case of catalyst without Ru (Figure B.7a) and the catalyst with 15 mM Ru (Figure B.7b). It

appears that the introduction of Ru yields smaller diameter CNTs. The average tube diameter drops from 1.43 nm to 1.26 nm. Similarly, when we look at the occurrence of a diameter less than or equal to 1.4 nm the presence of Ru significantly increases the proportion from nearly 49% up to 75%.

This observation with the presence of Ru and SiO_2 can be explained as follows: (i) Both, Ru and SiO_2 enhance catalyst dilution and prevent Fe nanoparticles agglomeration or (ii) SiO_2 enhance dilution while Ru can be more active chemically and form on the surface of Fe which leads to getting smaller diameter CNTs.

B.3.4 The impact of the concentration ratio of Fe to Ru on the CNT synthesis

The impact of the different Fe to Ru concentration ratios can be also tested to find if there is any possible correlation. The average diameter distribution of the CNT synthesis from catalyst solution with a different concentration ratio of Fe to Ru is presented in Figure B.8a. The percentage of the CNTs with diameters less than or equal to 1.4 nm is also presented in Figure B.8b.

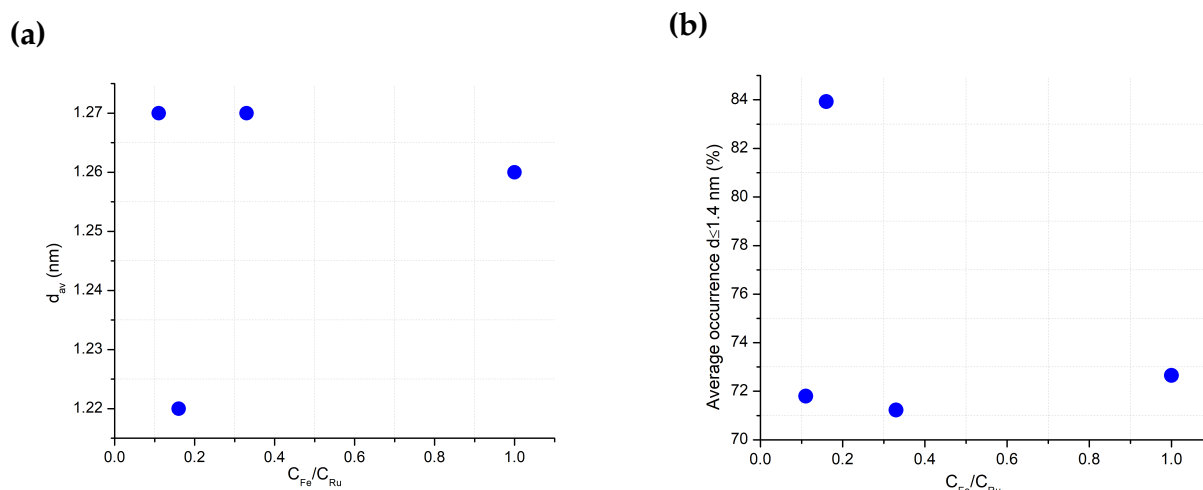


Figure B.8: The impact of Fe to Ru concentration ratio on the CNT synthesis: (a) the average diameter of the CNTs, (b) the percentage of the CNTs with diameter less than or equal to 1.4 nm

In this test, our aim was to observe if it is possible to find the [Fe] to [Ru] ratio, where we can get small diameter CNTs (thanks Ru) while increasing the density of the CNT (thanks Fe). We do not observe any clear trend while increasing [Fe]/[Ru] from 0.15 to 1. Summarizing the impact of the nanoparticles concentration in the catalyst mixture on the CNT synthesis, we conclude that $FeCl_3 - Ru - SiO_2$ with the concentration of Fe 5 mM, the concentration of Ru 15 mM is the best catalyst mixture to synthesize CNT with a smaller diameter.

B.3.5 Flow NF or HF

We also tested the impact of some CVD parameters on the CNT synthesis, the first one being the flux of gases such as H_2 , Ar/EtOH, and Ar are used in the CNT synthesis in the CVD furnace. We deposited the selected catalyst and CVD is done in two different flux conditions,

which are called "Normal flow (NF)" and "High flow (HF)".

In the case of NF (tested for 4 samples) the flux of gases are H₂ 190 sccm, Ar/EtOH 33.33 sccm, Ar 890 sccm. The flux is three times higher in the case of HF. Thus, the gases flow values in the case of HF (tested for 11 samples) are H₂ 570 sccm, Ar/EtOH 99.99 sccm, and Ar 2670 sccm.

Even though we have very similar results for both of the flux rates, we can see that in the case of HF, we have a bit smaller diameter CNTs (1.27 nm) compared to NF (1.25 nm), and the density of the CNTs with a diameter below 1.4 nm was higher in the case of high flow, 75.7% compare to 71.5%.

The flow in the CVD furnace is intended to align CNTs onto the substrate. Even in both flow conditions, we synthesized CNTs with the same dimensions, it can possible that the flow can increase the concentration of the carbon atoms on the nanoparticle's surface and lead to the synthesis of different amorphous structures.

B.3.6 The impact of moisture volume concentration in the furnace on the CNTs synthesis

Finally, we also tested the effect of the moisture volume concentration in the CVD furnace on the CNT synthesis. Moisture is formed by water adsorption on the lines in the CVD setup when the sample is loading. It is necessary to control the amount of moisture at the beginning of the CV process, thus it is removed by heating the lines and purging with Ar to get a controlled amount of moisture in the furnace. We selected a low moisture concentration of 5 ppm and high moisture concentration of 50 ppm. We observed that increasing the moisture concentration results in decreasing the average diameter of the CNTs from 1.28 nm down to 1.18 nm and increasing the percentage of the CNTs with a diameter lower than 1.4 nm, from 73% up to 81%.

B.4 Conclusion

The CVD method is one of the most popular CNT synthesis methods. However, controlling the diameter of the CNTs synthesized with this method is challenging. Here, we tested different catalyst concentrations and CVD parameters to obtain the CNT with the required dimensions to study the confinement of molecules, e.g. less than or equal to 1.4nm. We observed that Iron (Fe) is one of the main elements to synthesize CNTs, and mixing the Iron with Ruthenium decreases the diameter of the CNT. From CVD parameters the gas flux and moisture volume concentration in the furnace play also an important role to get smaller diameter CNTs.

The list of the samples used in this CVD optimization process are presented in the table B.2.

Table B.2: The list of samples used for CVD optimization to get small diameter CNTs

Samples	Catalyst	CVD flux	Moisture concentration (ppm)	Average diameter of CNTs (nm)	Percentage (%) with $d \leq 1.4$ nm
#1	Co 5mM; Mo 5mM	HF	5	1.52	33.3
#2	Fe 5 mM; Ru 15 mM	HF	5	1.27	70.9
#3	Co 5mM; Mo 5mM	HF	5	1.52	27.8
#4	Fe 5 mM; Ru 15 mM	HF	5	1.27	75
#5	Co 5mM; Mo 5mM	HF	50	1.45	40
#6	Fe 5 mM; Ru 15 mM	HF	50	1.13	87.2
#7	Co 5mM; Mo 5mM	HF	50	1.53	21.2
#8	Fe 5 mM; Ru 15 mM	HF	50	1.24	75
#9	Fe 5 mM; Ru 15 mM	NF	5	1.3	66.3
#10	Fe 1.66 mM; Ru 15 mM	NF	5	1.27	69.7
#11	Fe 5 mM; Ru 15 mM	NF	5	1.21	82.97
#12	Fe 5 mM; Ru 15 mM	NF	5	1.21	79.2
#13	Fe 5 mM; Ru 15 mM	NF	5	1.39	58.5
#14	Fe 5 mM; Ru 15 mM	HF	5	1.14	87.5
#15	Fe 2.5 mM; Ru 15 mM	HF	5	1.29	78.9
#16	Fe 5 mM; Ru 15 mM	HF	5	1.19	85.7
#17	Fe 2.5 mM; Ru 15 mM	HF	5	1.12	93.7
#18	Fe 15 mM	HF	5	1.5	38.2
#19	Fe 5 mM; Ru 15 mM	HF	5	1.48	45.3
#20	Fe 15 mM; Ru 15mM	HF	5	1.31	75.6
#21	Fe 15 mM	HF	5	1.36	60.3
#22	Fe 5 mM; Ru 15 mM	HF	5	1.23	73.5
#23	Fe 3 mM; Ru 15 mM	HF	5	1.15	75
#24	Fe 5 mM; Ru 15 mM	HF	5	1.27	70.4
#25	Fe 5 mM; Ru 30 mM	HF	5	1.24	79.2
#26	Fe 5 mM; Ru 15 mM	HF	5	1.49	37.5
#27	Fe 3 mM; Ru 15 mM	HF	5	1.54	30.2

Bibliography

- [1] Laura Martinez Maestro, Manuel Marques, Enrique Camarillo, Daniel Jaque, J. Solé, Julio Gonzalo, Francisco Jaque, Juan-Carlos del Valle, Francesco Mallamace, and H. Stanley. On the existence of two states in liquid water: Impact on biological and nanoscopic systems. *International Journal of Nanotechnology*, 13:667, 01 2016.
- [2] Kyung Hwan Kim, Alexander Späh, Harshad Pathak, Fivos Perakis, Daniel Mariedahl, Katrin Amann-Winkel, Jonas A. Sellberg, Jae Hyuk Lee, Sangsoo Kim, Jaehyun Park, Ki Hyun Nam, Tetsuo Katayama, and Anders Nilsson. Maxima in the thermodynamic response and correlation functions of deeply supercooled water. *Science*, 358(6370):1589–1593, 2017.
- [3] Nikita Kavokine, Roland R. Netz, and Lydéric Bocquet. Fluids at the nanoscale: From continuum to subcontinuum transport. *Annual Review of Fluid Mechanics*, 53(1):377–410, 2021.
- [4] F. G. Alabarse, J. Haines, O. Cambon, C. Levelut, D. Bourgogne, A. Haidoux, D. Granier, and B. Coasne. Freezing of water confined at the nanoscale. *Phys. Rev. Lett.*, 109:035701, Jul 2012.
- [5] Nicolas Giovambattista, Peter J. Rossky, and Pablo G. Debenedetti. Phase transitions induced by nanoconfinement in liquid water. *Phys. Rev. Lett.*, 102:050603, Feb 2009.
- [6] Hu Qiu and Wanlin Guo. Phase diagram of nanoscale water on solid surfaces with various wettabilities. *The Journal of Physical Chemistry Letters*, 10(20):6316–6323, 2019. PMID: 31566984.
- [7] Lydéric Bocquet and Elisabeth Charlaix. Nanofluidics, from bulk to interfaces. *Chem. Soc. Rev.*, 39:1073–1095, 2010.
- [8] Peter Agre, Landon S King, Masato Yasui, Wm B Guggino, Ole Petter Ottersen, Yoshinori Fujiyoshi, Andreas Engel, and Søren Nielsen. Aquaporin water channels—from atomic structure to clinical medicine. *Journal of Physiology*, 542(Pt 1):3–16, 2002.

- [9] Alessandro Siria, Marie-Laure Bocquet, and Lydéric Bocquet. New avenues for the large-scale harvesting of blue energy. *Nature Reviews Chemistry*, 1:0091, 2017.
- [10] Bruce E Logan and Menachem Elimelech. Membrane-based processes for sustainable power generation using water. *Nature*, 488(7411):313–319, 2012.
- [11] B. Hasted. Water a comprehensive treatise. 1 (ed. F. Franks):255–309, 1972.
- [12] M.F. Chaplin. Anomalous properties of water, 2003.
- [13] Martin F. Chaplin. *Structure and Properties of Water in its Various States*, pages 1–19. John Wiley Sons, Ltd, 2019.
- [14] Pier Luigi Silvestrelli and Michele Parrinello. Water molecule dipole in the gas and in the liquid phase. *Phys. Rev. Lett.*, 82:3308–3311, Apr 1999.
- [15] Charles Alfred Coulson and D. Eisenberg. Interactions of H_2O molecules in ice ii. interaction energies of H_2O molecules in ice. *Proceedings of the Royal Society of London. Series A. Mathematical and Physical Sciences*, 291(1427):454–459, 1966.
- [16] Jay R. Werber, Chinedum O. Osuji, and Menachem Elimelech. Materials for next-generation desalination and water purification membranes. *Nature Reviews Materials*, 1:16018, 2016.
- [17] Vladimir Torchilin. Multifunctional, stimuli-sensitive nanoparticulate systems for drug delivery. *Nature Reviews Drug Discovery*, 13:813–827, 2014.
- [18] Mohammad Darvishi Ganji, Saeid Mirzaei, and Zeinab Dalirandeh. Molecular origin of drug release by water boiling inside carbon nanotubes from reactive molecular dynamics simulation and dft perspectives. *Scientific Reports*, 7:4669, 2017.
- [19] Yun-Chiao Yao. *Ionic Transport through Carbon Nanotube Porins*. PhD thesis, University of California, Merced, 2021.
- [20] G. K. Batchelor. *An Introduction to Fluid Dynamics*. Cambridge Mathematical Library. Cambridge University Press, 2000.
- [21] Sony Joseph and N. R. Aluru. Why are carbon nanotubes fast transporters of water? *Nano Letters*, 8:452–458, 2008.
- [22] Eric Lauga, Michael Brenner, and Howard Stone. *Microfluidics: The No-Slip Boundary Condition*, pages 1219–1240. Springer Berlin Heidelberg, Berlin, Heidelberg, 2007.
- [23] Bing-Yang Cao, Jun Sun Sun, Min Chen, and Zeng-Yuan Guo. Molecular momentum transport at fluid-solid interfaces in mems/nems: a review. *International journal of molecular sciences*, 2009.
- [24] Christian Sendner, Dominik Horinek, Lydéric Bocquet, and Roland R. Netz. Interfacial water at hydrophobic and hydrophilic surfaces: Slip, viscosity, and diffusion. *Langmuir*, 25(18):10768–10781, 2009. PMID: 19591481.

- [25] Noriyuki Yoshii, Shinichi Miura, and Susumu Okazaki. A molecular dynamics study of dielectric constant of water from ambient to sub- and supercritical conditions using a fluctuating-charge potential model. *Chemical Physics Letters*, 345(1-2):195–200, 2001.
- [26] Alexander Schlaich, Ernst W. Knapp, and Roland R. Netz. Water dielectric effects in planar confinement. *Phys. Rev. Lett.*, 117:048001, Jul 2016.
- [27] Cui Zhang, François Gygi, and Giulia Galli. Strongly anisotropic dielectric relaxation of water at the nanoscale. *The Journal of Physical Chemistry Letters*, 4(15):2477–2481, 2013.
- [28] Jean-François Olivieri, James T. Hynes, and Damien Laage. Confined water’s dielectric constant reduction is due to the surrounding low dielectric media and not to interfacial molecular ordering. *The Journal of Physical Chemistry Letters*, 12(17):4319–4326, 2021. PMID: 33914550.
- [29] Tod A. Pascal, William A. Goddard, and Yousung Jung. Entropy and the driving force for the filling of carbon nanotubes with water. *Proceedings of the National Academy of Sciences*, 108(29):11794–11798, 2011.
- [30] François-Xavier Coudert, Anne Boutin, and Alain H. Fuchs. Open questions on water confined in nanoporous materials. *Communications Chemistry*, 4:106, 2021.
- [31] Michael D. Fayer and Nancy E. Levinger. Analysis of water in confined geometries and at interfaces. *Proceedings of the National Academy of Sciences*, 103:12271–12272, 2006.
- [32] Nikita S. Lazarenko, Valerii V. Golovakhin, Artem A. Shestakov, Nikita I. Lapekin, and Alexander G. Bannov. Recent advances on membranes for water purification based on carbon nanomaterials. *Nanomaterials*, 12(1):179, 2022.
- [33] Haixin Sui and Bong-Gyoon Han. Structural basis of water-specific transport through the aqp1 water channel. *Nature*, 414(6866):872–878, 2001.
- [34] Marcelo Ozu, Luciano Galizia, Cynthia Acuña, and Gabriela Amodeo. Aquaporins: More than functional monomers in a tetrameric arrangement. *International Journal of Molecular Sciences*, 20(8):1954, 2019.
- [35] Kazuyoshi Murata, Koji Mitsuoka, Teruhisa Hirai, and et al. Structural determinants of water permeation through aquaporin-1. *Nature*, 407(6804):599–605, 2000.
- [36] Régis Pomès and Benoît Roux. Structure and dynamics of a proton wire: a theoretical study of h⁺ translocation along the single-file water chain in the gramicidin a channel. *Biophysical journal*, 71(1):19–39, 1996.
- [37] Andreas Horner, Florian Zocher, Johannes Preiner, Nicole Ollinger, Christine Siligan, Sergey A. Akimov, and Peter Pohl. The mobility of single-file water molecules is governed by the number of h-bonds they may form with channel-lining residues. *Nature Communications*, 6:7714, 2015.

- [38] Andreas Horner, Christine Siligan, Alex Cornean, and Peter Pohl. Positively charged residues at the channel mouth boost single-file water flow. *Proceedings of the National Academy of Sciences*, 118(15):e2025793118, 2021.
- [39] Srilok Adapa and Ankit Malani. Cation hydration by confined water and framework-atoms have crucial role on thermodynamics of clay swelling. *Scientific Reports*, 12(1):17810, 2022.
- [40] Fátima González Sánchez, Fanni Jurányi, Thomas Gimmi, Luc Van Loon, Tobias Unruh, and Larryn W. Diamond. Translational diffusion of water and its dependence on temperature in charged and uncharged clays: A neutron scattering study. *The Journal of Chemical Physics*, 129(17), 11 2008. 174706.
- [41] Yuzi He, Ken-ichi Nomura, Rajiv K. Kalia, Aiichiro Nakano, and Priya Vashishta. Structure and dynamics of water confined in nanoporous carbon. *Phys. Rev. Mater.*, 2:115605, Nov 2018.
- [42] Toshio Yamaguchi, Hitoshi Hashi, and Shigeharu Kittaka. X-ray diffraction study of water confined in activated carbon pores over a temperature range of 228–298 k. *Journal of Molecular Liquids*, 129(1):57–62, 2006. New Highlights of Solution Chemistry: Diffraction, Simulation and Theoretical Studies.
- [43] Carlos Cuadrado-Collados, Ahmad A.A. Majid, Manuel Martínez-Escandell, Luke L. Daemen, Aleksandr Missyul, Carolyn Koh, and Joaquin Silvestre-Albero. Freezing/melting of water in the confined nanospace of carbon materials: Effect of an external stimulus. *Carbon*, 158:346–355, 2020.
- [44] Scott M. Auerbach, Kathleen A. Carrado, and Prabir K. Dutta. *Handbook of Zeolite Science and Technology*. Marcel Dekker, 2003.
- [45] Nathan W Ockwig, Randall T Cygan, Louise J Criscenti, and Tina M Nenoff. Molecular dynamics studies of nanoconfined water in clinoptilolite and heulandite zeolites. *The Journal of Physical Chemistry C*, 111(10):4048–4055, 2007.
- [46] Yilun Liu and Xi Chen. High permeability and salt rejection reverse osmosis by a zeolite nano-membrane. *Journal of Membrane Science*, 598:117698, 2020.
- [47] Thomas Humplik, Jongho Lee, Sean O’Hern, Tahar Laoui, Rohit Karnik, and Evelyn N Wang. Enhanced water transport and salt rejection through hydrophobic zeolite pores. *Nature nanotechnology*, 8(3):193–198, 2012.
- [48] Adam J. Rieth, Bryan M. Hunter, Mircea Dincă, and et al. Hydrogen bonding structure of confined water templated by a metal-organic framework with open metal sites. *Nature Communications*, 10(1):4771, 2019.
- [49] Eleonora Secchi, Sophie Marbach, Antoine Niguès, Derek Stein, Alessandro Siria, and Lydéric Bocquet. Massive radius-dependent flow slippage in carbon nanotubes. *Nature*, 537(7619):210–213, 2016.

- [50] Chang Y Won and N R Aluru. Water permeation through a subnanometer boron nitride nanotube. *Journal of the American Chemical Society*, 129(10):2748–2749, 2007.
- [51] Etienne Mangaud, Marie-Laure Bocquet, Lydéric Bocquet, and Benjamin Rotenberg. Chemisorbed vs physisorbed surface charge and its impact on electrokinetic transport: Carbon vs boron nitride surface. *The Journal of Chemical Physics*, 156(4):044703, 2022.
- [52] Anwar Hasmy, Luis Rincón, Adrien Noury, François Henn, and Vincent Jourdain. Physical interactions tune the chemisorption of polar anions on carbon nanostructures. *The Journal of Physical Chemistry C*, 126(31):13349–13357, 2022.
- [53] Gerhard Hummer, Jayendran C. Rasaiah, and Jacek P. Noworyta. Water conduction through the hydrophobic channel of a carbon nanotube. *Nature*, 414:188–190, 2001.
- [54] Alexander I Kolesnikov, Jean-Marc Zanotti, Chun-Keung Loong, and Pappannan Thiagarajan. Anomalously soft dynamics of water in a nanotube: a revelation of nanoscale confinement. *Physical Review Letters*, 93(3):035503, 2004.
- [55] Daisuke Takaiwa, Itaru Hatano, Kenichiro Koga, and Hideki Tanaka. Phase diagram of water in carbon nanotubes. *Proceedings of the National Academy of Sciences of the United States of America*, 116(19), 2008.
- [56] Amir Barati Farimani and Narayana R. Aluru. Existence of multiple phases of water at nanotube interfaces. *Journal of Physical Chemistry C*, 120:23763–23771, 2016.
- [57] Aris Chatzichristos and Jamal Hassan. Current understanding of water properties inside carbon nanotubes. *Nanomaterials*, 9(8):1152, 2019.
- [58] John A. Thomas and Alan J. H. McGaughey. Water flow in carbon nanotubes: Transition to subcontinuum transport. *Physical Review Letters*, 100(23):234502, 2008.
- [59] Kerstin Falk, Felix Sedlmeier, Laurent Joly, Roland R. Netz, and Lydéric Bocquet. Molecular origin of fast water transport in carbon nanotube membranes: Superlubricity versus curvature dependent friction. *Nano Letters*, 10(11):4067–4073, 2010.
- [60] Sridhar Kumar Kannam, B. D. Todd, J. S. Hansen, and Peter J. Daivis. How fast does water flow in carbon nanotubes? *The Journal of Chemical Physics*, 134(14):144704, 2011.
- [61] Sofie Cambre', Bob Schoeters, Sten Luyckx, Etienne Goovaerts, and Wim Wenseleers. Experimental observation of single-file water filling of thin single-wall carbon nanotubes down to chiral index (5,3). *Physical review letters*, 2010.
- [62] Erwan Paineau, Pierre-Antoine Albouy, Stéphan Rouzière, Andrea Orecchini, Stéphane Rols, and Pascale Launois. X-ray scattering determination of the structure of water during carbon nanotube filling. *Nano Letters*, 13(4):1751–1756, 2013.
- [63] Yutaka Maniwa, Hiromichi Kataura, Masatoshi Abe, Shinzo Suzuki, Yohji Achiba, Hiroshi Kira, and Kazuyuki Matsuda. Phase transition in confined water inside carbon nanotubes. *Journal of the Physical Society of Japan*, 71:2863–2866, 2002.

- [64] S. Ghosh, K. V. Ramanathan, and A. K. Sood. Water at nanoscale confined in single-walled carbon nanotubes studied by nmr. *Europhysics Letters*, 65(5):678–684, 2004.
- [65] Oleg Byl, Jin-Chen Liu, Yang Wang, Wai-Leung Yim, J. Karl Johnson, and John T. Yates Jr. Unusual hydrogen bonding in water-filled carbon nanotubes. *Journal of the American Chemical Society*, 128(37):12090–12097, 2006.
- [66] Kumar Varoon Agrawal, Steven Shimizu, Lee W. Drahushuk, Daniel Kilcoyne, and Michael S. Strano. Observation of extreme phase transition temperatures of water confined inside isolated carbon nanotubes. *Nature nanotechnology*, 12(3):267–273, 2017.
- [67] Shohei Chiashi, Yuta Saito, Takashi Kato, Satoru Konabe, Susumu Okada, Takahiro Yamamoto, and Yoshikazu Homma. Confinement effect of sub-nanometer difference on melting point of ice-nanotubes measured by photoluminescence spectroscopy. *ACS nano*, 13(2):1177–1182, 2019.
- [68] Jason K Holt, H G Park, Y Wang, M Stadermann, AB Artyukhin, CP Grigoropoulos, Aleksandr Noy, and Olgica Bakajin. Fast mass transport through sub-2-nanometer carbon nanotubes. *Science*, 312(5776):1034–1037, 2006.
- [69] Mark Whitby and Nicholas Quirke. Fluid flow in carbon nanotubes and nanopipes. *Nature Nanotechnology*, 2(2):87–94, 2007.
- [70] Bruce J Hinds, Nitin Chopra, Thomas Rantell, Rodney Andrews, Vasilis Gavalas, and Leonidas G Bachas. Aligned multiwalled carbon nanotube membranes. *Science*, 303(5654):62–65, 2004.
- [71] Mainak Majumder, Nitin Chopra, Rodney Andrews, and Bruce J. Hinds. Enhanced flow in carbon nanotubes. *Nature*, 438(44), 2005.
- [72] M Lokesh, Sung-Kyoung Youn, and Hyung Gyu Park. Osmotic transport across surface functionalized carbon nanotube membrane. *Nano letters*, 18(11):6679–6685, 2018.
- [73] Xiaoyan Qin, Quan Yuan, Yan Zhao, Shunping Xie, and Zheng Liu. Measurement of the rate of water translocation through carbon nanotubes. *Nano Letters*, 11(5):2173–2177, 2011.
- [74] Y. C. Yao, A. Taqieddin, M. A. Alibakhshi, M. Wanunu, N. R. Aluru, and A. Noy. Strong electroosmotic coupling dominates ion conductance of 1.5 nm diameter carbon nanotube porins. *ACS Nano*, 13(11):12851–12859, 2019.
- [75] Y. Li, Z. Li, F. Aydin, J. Quan, X. Chen, Y. C. Yao, C. Zhan, Y. Chen, T. A. Pham, and A. Noy. Water-ion permselectivity of narrow-diameter carbon nanotubes. *Science advances*, 6(38):eaba9966, 2020.
- [76] Thomas P. Burg, Michel Godin, Scott M. Knudsen, Wen Shen, Gary Carlson, Jennifer S. Foster, Ken Babcock, and Scott R. Manalis. Weighing of biomolecules, single cells and single nanoparticles in fluid. *Nature*, 446:1066–1069, apr 2007.

- [77] Alberto Martin-Perez, Daniel Ramos, Javier Tamayo, and Montserrat Calleja. Real-time particle spectrometry in liquid environment using microfluidic-nanomechanical resonators. pages 2146–2149, 06 2019.
- [78] Ulrich Prof. Dr. Gösele and O.-Y. Tong. Semiconductor wafer bonding. *Annual Review of Materials Science*, 28:215–241, 1990.
- [79] A. Berthold, B. Jakoby, and M.J. Vellekoop. Wafer-to-wafer fusion bonding of oxidized silicon to silicon at low temperatures. *Sensors and Actuators A: Physical*, 68(1):410–413, 1998. Eurosensors XI.
- [80] Philip W. Barth. Silicon fusion bonding for fabrication of sensors, actuators and microstructures. *Sensors and Actuators A: Physical*, 23(1):919–926, 1990. Proceedings of the 5th International Conference on Solid-State Sensors and Actuators and Eurosensors III.
- [81] Ali Harkous, Tomasz Jurkowski, Jean-Luc Bailleul, and Steven Le Corre. Influence of the temperature on the composites' fusion bonding quality. *AIP Conference Proceedings*, 1896(1):030007, 2017.
- [82] George Wallis and Daniel I. Pomerantz. Field assisted glass-metal sealing. *Journal of Applied Physics*, 40(10):3946–3949, 1969.
- [83] M J Lopez-Martinez, E M Campo, D Caballero, E Fernandez, A Errachid, J Esteve, and J A Plaza. Versatile micropipette technology based on deep reactive ion etching and anodic bonding for biological applications. *Journal of Micromechanics and Microengineering*, 19(10):105013, sep 2009.
- [84] T.J. Harpster and K. Najafi. Field-assisted bonding of glass to si-au eutectic solder for packaging applications. In *The Sixteenth Annual International Conference on Micro Electro Mechanical Systems, 2003. MEMS-03 Kyoto. IEEE*, pages 630–633, 2003.
- [85] A Berthold, L Nicola, P.M Sarro, and M.J Vellekoop. Glass-to-glass anodic bonding with standard ic technology thin films as intermediate layers. *Sensors and Actuators A: Physical*, 82(1):224–228, 2000.
- [86] J. Wei, Z.P. Wang, H. Xie, and Ng Fern Lan. Role of bonding temperature and voltage in silicon-to-glass anodic bonding. In *4th Electronics Packaging Technology Conference, 2002.*, pages 85–90, 2002.
- [87] Chia-Wen Tsao and Wan-Ci Syu. Bonding of thermoplastic microfluidics by using dry adhesive tape. *RSC Adv.*, 10:30289–30296, 2020.
- [88] Manish Kumar Raj and Suman Chakraborty. Pdms microfluidics: A mini review. *Journal of Applied Polymer Science*, 137(15):48958, 2020.
- [89] Aaron M. Lowe, Byram H. Ozer, Gregory J. Wiepz, Paul J. Bertics, and Nicholas L. Abbott. Engineering of pdms surfaces for use in microsystems for capture and isolation of complex and biomedically important proteins: Epidermal growth factor receptor as a model system. *Lab Chip*, 8(8):1357–1364, 2008.

- [90] Icaro Miranda, Ana Souza, Pedro Sousa, Joana Ribeiro, Elisabete M.S. Castanheira, Rui Lima, and Graça Minas. Properties and applications of pdms for biomedical engineering: A review. *Journal of Functional Biomaterials*, 13(1):2, 2021.
- [91] Younan Xia and George M. Whitesides. Soft lithography. *Angewandte Chemie (International ed. in English)*, 37(5):550–575, 1998.
- [92] Dong Qin, Younan Xia, and George M. Whitesides. Soft lithography for micro- and nanoscale patterning. *Nature Protocols*, 5(3):491–502, 2010.
- [93] Pdms: a review. <https://www.elveflow.com/microfluidic-reviews/general-microfluidics/the-polydimethylsiloxane-pdms-and-microfluidics/>, 2019.
- [94] Ki-Young Song, Hongbo Zhang, Wen jun Zhang, and Ana Paula Teixeira. Enhancement of the surface free energy of pdms for reversible and leakage-free bonding of pdms–ps microfluidic cell-culture systems. *Microfluidics and Nanofluidics*, 22:1–9, 2018.
- [95] Carlos L Gonzalez-Gallardo, Araceli Diaz Diaz, and Jose R Casanova-Moreno. Improving plasma bonding of pdms to gold-patterned glass for electrochemical microfluidic applications. *Microfluidics and Nanofluidics*, 25(2):20, 2021.
- [96] Saber Hammami, Aleksandr Oseev, Sylwester Bargiel, Rabah Zeggari, Céline Elie-Caille, and Thérèse Leblois. Microfluidics for high pressure: Integration on gaas acoustic biosensors with a leakage-free pdms based on bonding technology. *Micro-machines*, 13(5), 2022.
- [97] Sajad Hassanpour-Tamrin, Amir Sanati-Nezhad, and Arindom Sen. A simple and low-cost approach for irreversible bonding of polymethylmethacrylate and polydimethylsiloxane at room temperature for high-pressure hybrid microfluidics. *Scientific reports*, 11(1):4821, 2021.
- [98] S. Bhattacharya, A. Datta, J.M. Berg, and S. Gangopadhyay. Studies on surface wettability of poly(dimethyl) siloxane (pdms) and glass under oxygen-plasma treatment and correlation with bond strength. *Journal of Microelectromechanical Systems*, 14(3):590–597, 2005.
- [99] Liangcai Xiong, Peng Chen, and Quansheng Zhou. Adhesion promotion between pdms and glass by oxygen plasma pre-treatment. *Journal of Adhesion Science and Technology*, 28(11):1046–1054, 2014.
- [100] Jie Wang, Shijie Wang, Peng Zhang, and Yujie Li. Easy-disassembly bonding of pdms used for leak-tight encapsulation of microfluidic devices. In *2017 18th International Conference on Electronic Packaging Technology (ICEPT)*, pages 1051–1055, 2017.
- [101] H. H. Cao, T. H. Dinh, F. S. Hamdi, M. Couty, E. Martincic, M. Woytasik, and E. Dufour-Gergam. Reversible bonding by dimethyl-methylphenylmethoxy siloxane – based stamping technique for reusable poly(dimethylsiloxane) microfluidic chip. *Micronano Letters*, 10:229–232, 2015.

- [102] Abdoullatif Baraket, Nadia Zine, Michael Lee, Joan Bausells, Nicole Jaffrezic-Renault, François Bessueille, Nourdin Yaakoubi, and Abdelhamid Errachid. Development of a flexible microfluidic system based on a simple and reproducible sealing process between polymers and poly(dimethylsiloxane). *Microelectronic Engineering*, 111:332–338, 2013.
- [103] When pdms isn't the best. *Analytical Chemistry*, 79(9):3248–3253, 2007. PMID: 17523228.
- [104] Yisu Wang, Siyu Chen, Han Sun, Wanbo Li, Chong Hu, and Kangning Ren. Recent progresses in microfabricating perfluorinated polymers (teflons) and the associated new applications in microfluidics. *Microphysiological Systems*, 2(0), 2018.
- [105] Kirk J Regehr, Maribella Domenech, Jill T Koepsel, Kyle C Carver, Stephanie J Ellison-Zelski, William L Murphy, Linda A Schuler, Elaine T Alarid, and David J Beebe. Biological implications of polydimethylsiloxane-based microfluidic cell culture. *Lab on a chip*, 9(15):2132–2139, 2009.
- [106] Marcel Mulder. *Basic Principles of Membrane Technology*. Kluwer Academic Publishers, 1996.
- [107] David T. Eddington, John P. Puccinelli, and David J. Beebe. Thermal aging and reduced hydrophobic recovery of polydimethylsiloxane. *Sensors and Actuators B-chemical*, 114:170–172, 2006.
- [108] Jessamine Ng Lee, Cheolmin Park, and George M. Whitesides. Solvent compatibility of poly(dimethylsiloxane)-based microfluidic devices. *Analytical Chemistry*, 75(23):6544–6554, 2003. PMID: 14640726.
- [109] Hubert Lorenz, Michel Despont, Nicolas Fahrni, Nancy C. LaBianca, Philippe Renaud, and Peter Vettiger. Su-8: a low-cost negative resist for mems. *Journal of Micromechanics and Microengineering*, 7:121–124, 1997.
- [110] Joyce W. Kamande, Y. Wang, and A M Taylor. Cloning su8 silicon masters using epoxy resins to increase feature replicability and production for cell culture devices. *Biomicrofluidics*, 9 3:036502, 2015.
- [111] Rodrigo Martinez-Duarte and Marc J. Madou. *SU-8 Photolithography and Its Impact on Microfluidics*, page 38. CRC Press, 1st edition, 2012.
- [112] Michael Shaw, Daniel Nawrocki, Richard Hurditch, et al. Improving the process capability of su-8. *Microsystem Technologies*, 10(1):1–6, 2003.
- [113] Elisa Mitri, Giovanni Birarda, Lisa Vaccari, Saša Kenig, Massimo Tormen, and Gianluca Greci. Su-8 bonding protocol for the fabrication of microfluidic devices dedicated to ftir microspectroscopy of live cells. *Lab Chip*, 14:210–218, 2014.
- [114] F. J. Blanco, M. Agirregabiria, J. Garcia, J. Berganzo, M. Tijero, M. T. Arroyo, J. M. Ruano, I. Aramburu, and K. Mayora. Novel three-dimensional embedded SU-8 microchannels fabricated using a low temperature full wafer adhesive bonding. *Journal of Micromechanics and Microengineering*, 14(7):1047, June 2004.

- [115] S. Serraa, André Schneidera, Kristen Maleckib, S. E. Huqa, and W. Brennerb. A simple bonding process of su-8 to glass to seal a microfluidic device. 2007.
- [116] Ru Feng and Richard J. Farris. Influence of processing conditions on the thermal and mechanical properties of SU8 negative photoresist coatings. *Journal of Micromechanics and Microengineering*, 13(1):80, December 2003.
- [117] Steve Arscott. Su-8 as a material for lab-on-a-chip-based mass spectrometry. *Lab Chip*, 14:3668–3689, 2014.
- [118] P Abgrall and A-M Gué. Lab-on-chip technologies: making a microfluidic network and coupling it into a complete microsystem—a review. *Journal of Micromechanics and Microengineering*, 17(5):R15, apr 2007.
- [119] Dawit Admassu, Taiwo Durowade, Wei Gao, et al. Adhesive wafer bonding of microactuators with su-8 photoresist. *Microsystem Technologies*, 27(6):3293–3297, 2021.
- [120] J Steigert, O Brett, C Müller, M Strasser, N Wangler, H Reinecke, M Daub, and R Zengerle. A versatile and flexible low-temperature full-wafer bonding process of monolithic 3d microfluidic structures in su-8. *Journal of Micromechanics and Microengineering*, 18(9):095013, jul 2008.
- [121] C-T Pan, H Yang, S-C Shen, M-C Chou, and H-P Chou. A low-temperature wafer bonding technique using patternable materials. *Journal of Micromechanics and Microengineering*, 12(5):611, jun 2002.
- [122] Liming Yu, Francis E H Tay, Guolin Xu, Bangtao Chen, Marioara Avram, and Ciprian Iliescu. Adhesive bonding with su-8 at wafer level for microfluidic devices. *Journal of Physics: Conference Series*, 34(1):776, apr 2006.
- [123] Zhihao Zhu, Pengyu Chen, Ke Liu, and Carlos Escobedo. A versatile bonding method for pdms and su-8 and its application towards a multifunctional microfluidic device. *Micromachines*, 7(12):230, 2016.
- [124] Christopher G. Sip and Albert Folch. Irreversible integration of su-8 microstructures into pdms devices. 2010.
- [125] Renato Lima, Paulo Leão, Maria Piazzetta, and et al. Sacrificial adhesive bonding: a powerful method for fabrication of glass microchips. *Scientific Reports*, 5:13276, 2015.
- [126] Renato Sousa Lima, Paulo Augusto Gomes Carneiro Leão, Alessandra Maffei Monteiro, Maria Helena de Oliveira Piazzetta, Angelo Luiz Gobbi, Luiz Henrique Mazo, and Emanuel Carrilho. Glass/su-8 microchip for electrokinetic applications. *ELECTROPHORESIS*, 34(20-21):2996–3002, 2013.
- [127] Suman Narayan, Kraun Bae, Robert Lehn, Sandeep Yadav, Marcus Ott, Tobias Meckel, and Robert W Stark. Low-pressure bonding of monolithic su-8 microfluidic devices. *Journal of Micromechanics and Microengineering*, 28(12):125001, oct 2018.

- [128] Joost Melai, Cora Salm, Rob Wolters, and Jurriaan Schmitz. Qualitative and quantitative characterization of outgassing from su-8. *Microelectronic Engineering*, 86(4):761–764, 2009. MNE '08.
- [129] Mary B. Chan-Park, J. B. Zhang, Yehai Yan, and Chee Yoon Yue. Fabrication of large su-8 mold with high aspect ratio microchannels by uv exposure dose reduction. *Sensors and Actuators B-chemical*, 101:175–182, 2004.
- [130] Tingrui Pan, Antonio Baldi, and Babak Ziaie. Remotely adjustable check-valves with an electrochemical release mechanism for implantable biomedical microsystems. *Biomedical Microdevices*, 9:385–394, 2007.
- [131] Cora Salm, Victor M. Blanco Carballo, Joost Melai, and Jurriaan Schmitz. Reliability aspects of a radiation detector fabricated by post-processing a standard cmos chip. *Microelectron. Reliab.*, 48:1139–1143, 2008.
- [132] Kang Ren, Jianhua Zhou, and Hongkai Wu. Materials for microfluidic chip fabrication. *Accounts of Chemical Research*, 46:2396–2406, 11 2013.
- [133] Pei N. Nge, Casey I. Rogers, and Adam T. Woolley. Advances in microfluidic materials, functions, integration, and applications. *Chemical Reviews*, 113(4):2550–2583, 2013.
- [134] Edmond W.K. Young, Erwin Berthier, David J. Guckenberger, Eric Sackmann, Cornelis Lamers, Ivar Meyvantsson, Anna Huttenlocher, and David J. Beebe. Rapid prototyping of arrayed microfluidic systems in polystyrene for cell-based assays. *Analytical Chemistry*, 83(4):1408–1417, 2011.
- [135] D. Ogończyk, J. Węgrzyn, P. Jankowski, B. Dąbrowski, and P. Garstecki. Bonding of microfluidic devices fabricated in polycarbonate. *Lab Chip*, 10:1324–1327, 2010.
- [136] Wenhua Zhang, Shuichao Lin, Chunming Wang, Jia Hu, Cong Li, Zhixia Zhuang, Yongliang Zhou, Richard A. Mathies, and Chaoyong James Yang. Pmma/pdms valves and pumps for disposable microfluidics. *Lab Chip*, 9:3088–3094, 2009.
- [137] Dhiman Das, Suhanya Duraiswamy, Zhou Yi, Vincent Chan, and Chun Yang. Continuous droplet-based liquid-liquid extraction of phenol from oil. *Separation Science and Technology*, 50(7):1023–1029, 2015.
- [138] Jayson V. Pagaduan, Madison Ramsden, Kim O'Neill, and Adam T. Woolley. Microchip immunoaffinity electrophoresis of antibody–thymidine kinase 1 complex. *ELECTROPHORESIS*, 36(5):813–817, 2015.
- [139] Haotian Duan, Luyan Zhang, and Gang Chen. Plasticizer-assisted bonding of poly(methyl methacrylate) microfluidic chips at low temperature. *Journal of Chromatography A*, 1217(1):160–166, 2010.
- [140] Linling Li, Jiao Chen, Weijia Deng, Chen Zhang, Ye Sha, Zhen Cheng, Gi Xue, and Dongshan Zhou. Glass transitions of poly(methyl methacrylate) confined in

- nanopores: Conversion of three- and two-layer models. *The Journal of Physical Chemistry B*, 119(15):5047–5054, 2015. PMID: 25807007.
- [141] A. Baldan. Adhesion phenomena in bonded joints. *International Journal of Adhesion and Adhesives*, 38:95–116, 2012.
- [142] Y. Chen, L. Zhang, and G. Chen. Fabrication, modification, and application of poly(methyl methacrylate) microfluidic chips. *Electrophoresis*, 29(9):1801–1814, 2008.
- [143] Andris Liga, Jackson A. S. Morton, and Maiwenn Kersaudy-Kerhoas. Safe and cost-effective rapid-prototyping of multilayer pmma microfluidic devices. *Microfluidics and Nanofluidics*, 20(11):164, 2016.
- [144] Kieu The Loan Trinh, Duc Anh Thai, Woo Ri Chae, and Nae Yoon Lee. Rapid fabrication of poly(methyl methacrylate) devices for lab-on-a-chip applications using acetic acid and uv treatment. *ACS Omega*, 5(28):17396–17404, 2020. PMID: 32715224.
- [145] pmma-acrylic-injection-molding-problems-and-solutions. <https://www.cavitymold.com/pmma-acrylic-injection-molding-problems-and-solutions/>, note = Accessed: July 16, 2023.
- [146] Jintae Park, Myung-Jin Baek, Hyun Woo Choi, Hak-Sun Kim, and Dong Woog Lee. Development of poly(methyl methacrylate)-based copolymers with improved heat resistance and reduced moisture absorption. *Langmuir*, 35(48):15880–15886, 2019. PMID: 31419144.
- [147] Britta Weinhausen and Sarah Köster. Microfluidic devices for x-ray studies on hydrated cells. *Lab Chip*, 13:212–215, 2013.
- [148] Isabella T. Neckel, Luciano F. de Castro, Felipe Callefo, and et al. Development of a sticker sealed microfluidic device for in situ analytical measurements using synchrotron radiation. *Scientific Reports*, 11(1):23671, 2021.
- [149] Wurong Ren, Heejin Kim, Hyune-Jea Lee, Jun Wang, Hao Wang, and Dong-Pyo Kim. A pressure-tolerant polymer microfluidic device fabricated by the simultaneous solidification-bonding method and flash chemistry application. *Lab Chip*, 14:4263–4269, 2014.
- [150] Yiqiang Fan, Huawei Li, Ying Yi, and Ian Foulds. Pmma to polystyrene bonding for polymer based microfluidic systems. *Microsystem Technologies*, 20, 01 2014.
- [151] Nimai Nayak, Chee Yue, Y. Lam, and Y. Tan. Thermal bonding of pmma: Effect of polymer molecular weight. *Microsystem Technologies*, 16:487–491, 12 2009.
- [152] M-E Vlachopoulou, A Tserepi, P Pavli, P Argitis, M Sanopoulou, and K Misiakos. A low temperature surface modification assisted method for bonding plastic substrates. *Journal of Micromechanics and Microengineering*, 19(1):015007, nov 2008.
- [153] Lance Kersey, Vincent Ebacher, Vahid Bazargan, Rizhi Wang, and Boris Stoeber. The effect of adhesion promoter on the adhesion of pdms to different substrate materials. *Lab Chip*, 9:1002–1004, 2009.

- [154] Mark A Eddings, Michael A Johnson, and Bruce K Gale. Determining the optimal pdms–pdms bonding technique for microfluidic devices. *Journal of Micromechanics and Microengineering*, 18(6):067001, apr 2008.
- [155] Jae Bem You, Kyoung-Ik Min, Bora Lee, Dong-Pyo Kim, and Sung Gap Im. A doubly cross-linked nano-adhesive for the reliable sealing of flexible microfluidic devices. *Lab Chip*, 13:1266–1272, 2013.
- [156] Saber Hammami, Aleksandr Oseev, Sylwester Bargiel, Rabah Zeggari, Céline Elie-Caille, and Therese Leblois. Microfluidics for high pressure: Integration on gaas acoustic biosensors with a leakage-free pdms based on bonding technology. *Micromachines*, 13(5):755, 2022.
- [157] Pei Liu, Zhicheng Lv, Bin Sun, Yuling Hu, Jie Li, Xianren Zhang, Yuanyuan Sun, and Xuping Zhang. A universal bonding method for preparation of microfluidic biosensor. *Microfluidics and Nanofluidics*, 25:43, 2021.
- [158] Sebastian Schneider, Elisa J. S. Brás, Oliver Schneider, Klaus Schlünder, and Peter Loskill. Facile patterning of thermoplastic elastomers and robust bonding to glass and thermoplastics for microfluidic cell culture and organ-on-chip. *Micromachines*, 12(5):575, 2021.
- [159] Tuan Ngoc Anh Vo and Pin-Chuan Chen. Maximizing interfacial bonding strength between pdms and pmma substrates for manufacturing hybrid microfluidic devices withstanding extremely high flow rate and high operation pressure. *Sensors and Actuators A: Physical*, 334:113330, 2022.
- [160] Jeonghyeon Cheon and Seunghyun Kim. Intermediate layer-based bonding techniques for polydimethylsiloxane/digital light processing 3d-printed microfluidic devices. *Journal of Micromechanics and Microengineering*, 29(9):095005, jul 2019.
- [161] A.L. Kalamkarov, A.V. Georgiades, S.K. Rokkam, V.P. Veedu, and M.N. Ghasemi-Nejhad. Analytical and numerical techniques to predict carbon nanotubes properties. *International Journal of Solids and Structures*, 43(22):6832–6854, 2006.
- [162] Annia Galano. Carbon nanotubes: promising agents against free radicals. *Nanoscale*, 2:373–380, 2010.
- [163] Vladimir Pimonov. *Growth kinetics of individual carbon nanotubes studied by in-situ optical microscopy*. PhD thesis, Université Montpellier, 2021. NNT: 2021MONTS101. tel-03615720.
- [164] Georgy G. Samsonidze, Riichiro Saito, Ado Jorio, Marcos A. Pimenta, Antonio G. Souza Filho, Andreas Grüneis, Gene Dresselhaus, and Mildred S. Dresselhaus. The concept of cutting lines in carbon nanotube science. *Journal of Nanoscience and Nanotechnology*, 3(6):431–458, 2003.
- [165] M.S. Dresselhaus, G. Dresselhaus, and R. Saito. Physics of carbon nanotubes. *Carbon*, 33(7):883–891, 1995. Nanotubes.

- [166] Alper Baydin, Franklin Tay, Jing Fan, Manukumara Manjappa, Weilu Gao, and Junichiro Kono. Carbon nanotube devices for quantum technology. *Materials*, 15(4):1535, 2022.
- [167] Catherine Journet and Patrick Bernier. Production of carbon nanotubes. *Applied Physics A*, 67:1–9, Jul 1998.
- [168] C. Journet, W. K. Maser, P. Bernier, A. Loiseau, M. L. delaChapelle, S. Lefrant, P. Deniard, R. Lee, and J. E. Fischer. Large-scale production of single-walled carbon nanotubes by the electric-arc technique. *Nature*, 388(6644):756–758, 1997.
- [169] Tawfik A. Saleh, Taye Damola Shuaib, Gaddafi I. Danmaliki, and Mohammed A. Al-Daous. Carbon-based nanomaterials for desulfurization: Classification, preparation, and evaluation. In Tawfik A. Saleh, editor, *Applying Nanotechnology to the Desulfurization Process in Petroleum Engineering*, chapter 5. IGI Global, October 2015.
- [170] Dr. Muhammad Ikram, Ali Raza, Atif Shahbaz, Haleema Ijaz, Sarfraz Ali, Ali Haider, Muhammad Hussain, Junaid Haider, Arslan Rafi, and Salamat Ali. *Carbon Nanotubes*, pages 1–18. 12 2020.
- [171] Christian Klinkle. Analysis of the catalytic growth of carbon nanotubes. 03 2003.
- [172] Ning Yang, Xianping Chen, Tianling Ren, Ping Zhang, and Daoguo Yang. Carbon nanotube based biosensors. *Sensors and Actuators B: Chemical*, 207:690–715, 2015.
- [173] F. Kokai, A. Koshio, M. Shiraishi, T. Matsuta, S. Shimoda, M. Ishihara, Y. Koga, and H. Deno. Modification of carbon nanotubes by laser ablation. *Diamond and Related Materials*, 14(3):724–728, 2005. Proceedings of Diamond 2004, the 15th European Conference on Diamond, Diamond-Like Materials, Carbon Nanotubes, Nitrides and Silicon Carbide.
- [174] Erik T Thostenson, Zhifeng Ren, and Tsu-Wei Chou. Advances in the science and technology of carbon nanotubes and their composites: a review. *Composites Science and Technology*, 61(13):1899–1912, 2001.
- [175] Ahmad Ismail, Pei Sean Goh, Jingli Tee, Suhaila Sanip, and Madzlan Aziz. A review of purification techniques for carbon nanotubes. *Nano*, 3(3):101–108, 2008.
- [176] Ali Eatemadi, Hadis Daraee, Hamzeh Karimkhanloo, Mohammad Kouhi, Nosratollah Zarghami, Abolfazl Akbarzadeh, Mozghan Abasi, Younes Hanifehpour, and Sang Woo Joo. Carbon nanotubes: Properties, synthesis, purification, and medical applications. *Nanoscale Research Letters*, 9(1):393, 2014.
- [177] Khalid Saeed and Ibrahim Khan. Carbon nanotubes - properties and applications: A review. *Carbon Letters*, 14(3):131–144, 2013.
- [178] T. W. Ebbesen, H. J. Lezec, H. Hiura, J. W. Bennett, H. F. Ghaemi, and T. Thio. Electrical conductivity of individual carbon nanotubes. *Nature*, 382(6586):54, 1996.

- [179] Ji-Yong Park. *Band Structure and Electron Transport Physics of One-Dimensional SWNTs*, pages 1–42. Springer US, Boston, MA, 2009.
- [180] Hongjie Dai, Eric W. Wong, and Charles M. Lieber. Probing electrical transport in nanomaterials: Conductivity of individual carbon nanotubes. *Science*, 272(5261):523–526, 1996.
- [181] J. W. Mintmire, B. I. Dunlap, and C. T. White. Are fullerene tubules metallic? *Physical Review Letters*, 68(5):631–634, 1992.
- [182] Noriaki Hamada, Shoichi Sawada, and Atsushi Oshiyama. New one-dimensional conductors: Graphitic microtubules. *Physical Review Letters*, 68(10):1579–1581, 1992.
- [183] Kazuyoshi Tanaka, Kenji Okahara, Mayumi Okada, and Tokio Yamabe. Electronic properties of bucky-tube model. *Chemical Physics Letters*, 191(5):469–472, 1992.
- [184] Teri W. Odom, Jin-Lin Huang, and Charles M. Lieber. Single-walled carbon nanotubes: from fundamental studies to new device concepts. *Annals of the New York Academy of Sciences*, 960:203–215, 2002.
- [185] Wei Gao and Junichiro Kono. Science and applications of wafer-scale crystalline carbon nanotube films prepared through controlled vacuum filtration. *Royal Society Open Science*, 6(3):181605, 2019.
- [186] R. Saito, M. Fujita, G. Dresselhaus, and M. S. Dresselhaus. Electronic structure of chiral graphene tubules. *Applied Physics Letters*, 60(18):2204–2206, May 1992.
- [187] Wikipedia. Field-effect transistor. https://en.wikipedia.org/wiki/Field-effect_transistor. Accessed: April 19, 2023.
- [188] Roberto Marani and Anna Perri. The next generation of fets: Cntfets. *IEEE Transactions on Nanotechnology*, 14(6):1087–1094, 2015.
- [189] Sander J. Tans, Alwin R. M. Verschueren, and Cees Dekker. Room-temperature transistor based on a single carbon nanotube. *Nature*, 393(6680):49–52, 1998.
- [190] Joerg Appenzeller, Joachim Knoch, Richard Martel, Vincent Derycke, Shalom J. Wind, and Phaedon Avouris. Carbon nanotube electronics. *IEEE Transactions on Nanotechnology*, 1(4):184–189, 2002.
- [191] Rafael Vargas-Bernal and Gabriel Herrera-Pérez. *Carbon Nanotube- and Graphene Based Devices, Circuits and Sensors for VLSI Design*, pages 41–66. InTech, 01 2012.
- [192] Nicolas Champauzas. *CNTFET-based biosensor technology for kinase activity monitoring*. Phd thesis, Université Montpellier, 2021.
- [193] Woong Kim, Ali Javey, Ophir Vermesh, Qian Wang, Yiming Li, and Hongjie Dai. Hysteresis caused by water molecules in carbon nanotube field-effect transistors. *Nano Letters*, 3(2):193–198, 2003.

- [194] Joon Sung Lee, Sunmin Ryu, Kwonjae Yoo, Insung S. Choi, Wan Soo Yun, and Jinhee Kim. Origin of gate hysteresis in carbon nanotube field-effect transistors. *The Journal of Physical Chemistry C*, 111(34):12504–12507, 2007.
- [195] Steven G. Noyce, John L. Doherty, Zenghui Cheng, Han Han, Sean Bowen, and Aaron D. Franklin. Electronic stability of carbon nanotube transistors under long-term bias stress. *Nano Letters*, 19(3):1460–1466, 2019.
- [196] Yu-Xuan Lu, Chih-Ting Lin, Ming-Hung Tsai, and Kuan-Chang Lin. Review-hysteresis in carbon nano-structure field effect transistor. *Micromachines*, 13(4):509, 2022.
- [197] H G Ong, J W Cheah, X Zou, B Li, X H Cao, H Tantang, L-J Li, H Zhang, G C Han, and J Wang. Origin of hysteresis in the transfer characteristic of carbon nanotube field effect transistor. *Journal of Physics D: Applied Physics*, 44(28):285301, jun 2011.
- [198] Marcus Rinkiö, Marina Timmermans, Päivi Törmä, and Andreas Johansson. Effect of humidity on the hysteresis of single walled carbon nanotube field-effect transistors. *physica status solidi (b)*, 245(10):2315–2318, 2008.
- [199] Changxin Chen and Yafei Zhang. Review on optimization methods of carbon nanotube field-effect transistors. *The Open Nanoscience Journal*, 100, 12 2007.
- [200] J. Appenzeller, J. Knoch, M. Radosavljević, and Ph. Avouris. Multimode transport in schottky-barrier carbon-nanotube field-effect transistors. *Phys. Rev. Lett.*, 92:226802, Jun 2004.
- [201] S. J. Wind, J. Appenzeller, and Ph. Avouris. Lateral scaling in carbon-nanotube field-effect transistors. *Phys. Rev. Lett.*, 91:058301, Jul 2003.
- [202] Dongchul Sung, Suklyun Hong, Yong-Hoon Kim, Noejung Park, Sanghyeob Kim, Sung Lyul Maeng, and Ki-Chul Kim. Ab initio study of the effect of water adsorption on the carbon nanotube field-effect transistor. *Applied Physics Letters*, 89(24):243110, Dec 2006.
- [203] Tal Sharf, Joshua W. Kevek, Tristan DeBorde, Jenna L. Wardini, and Ethan D. Minot. Origins of charge noise in carbon nanotube field-effect transistor biosensors. *Nano Letters*, 12(12):6380–6384, 2012. PMID: 23171196.
- [204] Alina Veligura, Paul J. Zomer, Ivan J. Vera-Marun, Csaba Józsa, Pavlo I. Gordiichuk, and Bart J. van Wees. Relating hysteresis and electrochemistry in graphene field effect transistors. *Journal of Applied Physics*, 110(11):113708, Dec 2011.
- [205] Jiapei Shu, Gongtao Wu, Yao Guo, Bo Liu, Xianlong Wei, and Qing Chen. The intrinsic origin of hysteresis in mos2 field effect transistors. *Nanoscale*, 8:3049–3056, 2016.
- [206] Keith Bradley, Jean-Christophe Gabriel, Alexander Star, and George Gruner. Short-channel effects in contact-passivated nanotube chemical sensors. *Applied Physics Letters*, 83(18):3821–3823, Nov 2003.

- [207] Xiaolei Liu, Zhicheng Luo, Song Han, Tao Tang, Daihua Zhang, and Chongwu Zhou. Band engineering of carbon nanotube field-effect transistors via selected area chemical gating. *Applied Physics Letters*, 86:243501, 2005.
- [208] Iddo Heller, Anne M. Janssens, Jaan Männik, Ethan D. Minot, Serge G. Lemay, and Cees Dekker. Identifying the mechanism of biosensing with carbon nanotube transistors. *Nano Letters*, 8(2):591–595, 2008. PMID: 18162002.
- [209] Amir Foudeh, Raphael Pfattner, Shiheng Lu, Nicola Kubzdelo, Theodore Gao, Ting Lei, and Zhenan Bao. Effects of water and different solutes on carbon-nanotube low-voltage field-effect transistors. *Small*, 16(31):2002875, July 2020.
- [210] Iddo Heller, Sohail Chatoor, Jaan Männik, Marcel A. G. Zevenbergen, Cees Dekker, and Serge G. Lemay. Influence of electrolyte composition on liquid-gated carbon nanotube and graphene transistors. *Journal of the American Chemical Society*, 132(48):17149–17156, December 2010. PMID: 21077655.
- [211] Pil Sun Na, Hyojin Kim, Hye-Mi So, Ki-Jeong Kong, Hyunju Chang, Beyong Hwan Ryu, Youngmin Choi, Jeong-O Lee, Byoung-Kye Kim, Ju-Jin Kim, and Jinhee Kim. Investigation of the humidity effect on the electrical properties of single-walled carbon nanotube transistors. *Applied Physics Letters*, 87(9):093101, Aug 2005.
- [212] Saravanan Arunachalam, Akhil A. Gupta, Ricardo Izquierdo, and Frederic Nabki. Suspended carbon nanotubes for humidity sensing. *Sensors*, 18(5):1655, 2018.
- [213] Naoka Nagamura, Hirokazu Fukidome, Kosuke Nagashio, Koji Horiba, Takayuki Ide, Kazutoshi Funakubo, Keiichiro Tashima, Akira Toriumi, Maki Suemitsu, Karsten Horn, and Masaharu Oshima. Influence of interface dipole layers on the performance of graphene field effect transistors. *Carbon*, 152:680–687, 2019.
- [214] Arun Kathalingam, V. Senthilkumar, and Joo-kee Rhee. Hysteresis i–v nature of mechanically exfoliated graphene fet. *Journal of Materials Science: Materials in Electronics*, 25(3):1303–1308, 2014.
- [215] Zhi-Min Liao, Bing-Hong Han, Yang-Bo Zhou, and Da-Peng Yu. Hysteresis reversion in graphene field-effect transistors. *The Journal of Chemical Physics*, 133(4):044703, 07 2010.
- [216] Ranjit Pati, Yiming Zhang, Saroj K. Nayak, and Pulickel M. Ajayan. Effect of h₂o adsorption on electron transport in a carbon nanotube. *Applied Physics Letters*, 81(14):2638–2640, Sep 2002.
- [217] Takao Someya, Philip Kim, and Colin Nuckolls. Conductance measurement of single-walled carbon nanotubes in aqueous environment. *Applied Physics Letters*, 82(14):2338–2340, 04 2003.
- [218] Mark E. Roberts, Melburne C. LeMieux, and Zhenan Bao. Sorted and aligned single-walled carbon nanotube networks for transistor-based aqueous chemical sensors. *ACS Nano*, 3(10):3287–3293, 2009. PMID: 19856982.

- [219] H. Lin and S. Tiwari. Localized charge trapping due to adsorption in nanotube field-effect transistor and its field-mediated transport. *Applied Physics Letters*, 89(7):073507, 08 2006.
- [220] Prasantha R. Mudimela, Kestutis Grigoras, Ilya Anoshkin, Aapo Varpula, Vladimir Ermolov, Anton Anisimov, Albert Nasibulin, Sergey Novikov, and Esko Kauppinen. Single-walled carbon nanotube network field effect transistor as a humidity sensor. *Journal of Sensors*, 2012, 06 2012.
- [221] Chung Y. Lee and Michael S. Strano. Understanding the dynamics of signal transduction for adsorption of gases and vapors on carbon nanotube sensors. *Langmuir: The ACS Journal of Surfaces and Colloids*, 21(11):5192–5196, 2005.
- [222] Douglas R. Kauffman and Alexander Star. Carbon nanotube gas and vapor sensors. *Angewandte Chemie (International ed. in English)*, 47(35):6550–6570, 2008.
- [223] E. Dujardin, T. W. Ebbesen, H. Hiura, and K. Tanigaki. Capillarity and wetting of carbon nanotubes. *Science*, 265(5180):1850–1852, 1994.
- [224] Di Cao, Pei Pang, Jin He, Tao Luo, Jae Hyun Park, Predrag Krstic, Colin Nuckolls, Jinyao Tang, and Stuart Lindsay. Electronic sensitivity of carbon nanotubes to internal water wetting. *ACS Nano*, 5(4):3113–3119, 2011. PMID: 21452854.
- [225] D Cao, P Pang, H Liu, J He, and S M Lindsay. Electronic sensitivity of a single-walled carbon nanotube to internal electrolyte composition. *Nanotechnology*, 23(8):085203, feb 2012.
- [226] Jingmin Li, Chao Liang, Hao Zhang, and Chong Liu. Reliable and high quality adhesive bonding for microfluidic devices. *Micro & Nano Letters*, 12(2):90–94, 2017.
- [227] Yan Xu, Chenxi Wang, Lixiao Li, Nobuhiro Matsumoto, Kihoon Jang, Yiyang Dong, Kazuma Mawatari, Tadatomo Suga, and Takehiko Kitamori. Bonding of glass nanofluidic chips at room temperature by a one-step surface activation using an o₂/cf₄ plasma treatment. *Lab Chip*, 13:1048–1052, 2013.
- [228] Chia-Wen Tsao and Don DeVoe. Bonding of thermoplastic polymer microfluidics. *Microfluidics and Nanofluidics*, 6:1–16, 11 2009.
- [229] B.L Gray, D Jaeggi, N.J Mourlas, B.P van Drieënhuizen, K.R Williams, N.I Maluf, and G.T.A Kovacs. Novel interconnection technologies for integrated microfluidic systems. *Sensors and Actuators A: Physical*, 77(1):57–65, 1999.
- [230] Yuksel Temiz, Robert D. Lovchik, Govind V. Kaigala, and Emmanuel Delamarche. Lab-on-a-chip devices: How to close and plug the lab? *Microelectronic Engineering*, 132:156–175, 2015. Micro and Nanofabrication Breakthroughs for Electronics, MEMS and Life Sciences.
- [231] George M. Whitesides. When pdms isn't the best. *Analytical Chemistry*, 79(9):3248–3253, 2007. PMID: 17523228.

- [232] Elodie Sollier, Coleman Murray, Pietro Maoddi, and Dino Di Carlo. Rapid prototyping polymers for microfluidic devices and high pressure injections. *Lab on a chip*, 11(21):3752–3765, November 2011.
- [233] Pietro Salvo, Rik Verplancke, Frederick Bossuyt, David Latta, Benoit Vandecasteele, Chang Liu, and Jan Vanfleteren. Adhesive bonding by su-8 transfer for assembling microfluidic devices. *Microfluidics and Nanofluidics*, 13(6):987–991, December 2012.
- [234] MEMScyclopedia. SU-8: Thick photo-resist for MEMS. <http://memscyclopedia.org/su8.html>, 1999. [Online; accessed 8-May-2023].
- [235] Winnie Wing Yin Chow, Kin Fong Lei, Guangyi Shi, Wen Jung Li, and Qiang Huang. Microfluidic channel fabrication by PDMS-interface bonding. *Smart Materials and Structures*, 15(1):S112–S119, Jan 2006.
- [236] Alexandra Borók, Kristóf Laboda, and Attila Bonyár. Pdms bonding technologies for microfluidic applications: A review. *Biosensors*, 11:292, Aug 2021.
- [237] Ummikalsom Abidin, Nurul Ayuni Safra Mat Daud, and Valentin Le Brun. Replication and leakage test of polydimethylsiloxane (pdms) microfluidics channel. *AIP Conference Proceedings*, 2062(1):020064, 01 2019.
- [238] A. Lamberti, A. Sacco, S. Bianco, E. Giuri, M. Quaglio, A. Chiodoni, and E. Tresso. Microfluidic sealing and housing system for innovative dye-sensitized solar cell architecture. *Microelectronic Engineering*, 88(8):2308–2310, 2011. Proceedings of the 36th International Conference on Micro- and Nano-Engineering (MNE).
- [239] Catharine Shea Thompson and Adam R. Abate. Adhesive-based bonding technique for pdms microfluidic devices. *Lab on a chip*, 13(4):632–635, 2013.
- [240] Khadija Yazda, Saïd Tahir, Thierry Michel, Bastien Loubet, Manoel Manghi, Jeremy Bentin, Fabien Picaud, John Palmeri, François Henn, and Vincent Jourdain. Voltage-activated transport of ions through single-walled carbon nanotubes. *Nanoscale*, 9:11976–11986, 2017.
- [241] Laura Bsawmaii, Clement Delacou, Sebastien Meance, Koutayba Saada, Saïd Tahir, Christophe Roblin, Francois Henn, Adrien Noury, and Vincent Jourdain. In preparation, 2023. Unpublished.
- [242] Vincent Silverio, Saptarshi Guha, Adam Keiser, Rahul Natu, Darwin R Reyes, Henk van Heeren, Nicholas Verplanck, and Lauren H Herbertson. Overcoming technological barriers in microfluidics: Leakage testing. *Frontiers in Bioengineering and Biotechnology*, 10:958582, 2022.
- [243] Inc. Agilent Technologies. *Vacuum and Leak Detection Reference Formulas, Properties, and Glossary*. Agilent Technologies, Inc., USA, October 2022. Training Guide, Cat. No. 5994-5366EN.
- [244] Hans Rottländer, Walter Umrath, and Gerhard Voss. *Fundamentals of Leak Detection*. Leybold Vacuum Products Division, Cologne, Germany, 2016. Cat. No. 199 79_VA.02.

- [245] Vera Schroeder, Suchol Savagatrup, Maggie He, Sibbo Lin, and Timothy M. Swager. Carbon nanotube chemical sensors. *Chemical Reviews*, 119(1):599–663, 2019.
- [246] Mildred S. Dresselhaus, Ado Jorio, and Riichiro Saito. Characterizing graphene, graphite, and carbon nanotubes by raman spectroscopy. *Annual Review of Condensed Matter Physics*, 1:89–108, 2010.
- [247] Ado Jorio and Antonio Souza Filho. Raman studies of carbon nanostructures. *Annual Review of Materials Research*, 46:357–382, 07 2016.
- [248] Chengxiang Xiang, Kimberly M. Papadantonakis, and Nathan S. Lewis. Principles and implementations of electrolysis systems for water splitting. *Materials horizons*, 3:169–173, 2016.
- [249] Xiaoxiao Wei, Xiaohua Zhang, Huan Ma, Farihal Islam Farha, Yeqian GE, and Fujun Xu. Incandescent annealing purification of carbon nanotube films with high efficiency and non-destructiveness. *Surfaces and Interfaces*, 40:103037, 2023.
- [250] Svetlana Khasminskaya, Feliks Pyatkov, Benjamin S. Flavel, Wolfram H. Pernice, and Ralph Krupke. Waveguide-integrated light-emitting carbon nanotubes. *Advanced Materials*, 26(21):3465–3472, 2014.
- [251] Michael T. Pettes and Li Shi. Thermal and structural characterizations of individual single-, double-, and multi-walled carbon nanotubes. *Advanced Functional Materials*, 19(24):3918–3925, 2009.
- [252] Yi Yang, Zhongwu Wang, Zeyang Xu, Kunjie Wu, Xiaoqin Yu, Xiaosong Chen, Yancheng Meng, Hongwei Li, Song Qiu, Hehua Jin, Liqiang Li, and Qingwen Li. Low hysteresis carbon nanotube transistors constructed via a general dry-laminating encapsulation method on diverse surfaces. *ACS Applied Materials & Interfaces*, 9(16):14292–14300, 2017. PMID: 28375600.
- [253] P. Barthold, T. Lüdtkke, H. Schmidt, and R. J. Haug. Low-temperature hysteresis in the field effect of bilayer graphene. *New Journal of Physics*, 13(4):043020, apr 2011.
- [254] Aaron D. Franklin, George S. Tulevski, Shu-Jen Han, Davood Shahrjerdi, Qing Cao, Hong-Yu Chen, H.-S. Philip Wong, and Wilfried Haensch. Variability in carbon nanotube transistors: Improving device-to-device consistency. *ACS Nano*, 6(2):1109–1115, 2012. PMID: 22272749.
- [255] Kaihui Liu, Wenlong Wang, Zhi Xu, Xuedong Bai, Enge Wang, Yagang Yao, Jin Zhang, and Zhongfan Liu. Chirality-dependent transport properties of double-walled nanotubes measured in situ on their field-effect transistors. *Journal of the American Chemical Society*, 131(1):62–63, 2009. PMID: 19093842.
- [256] L.T. Zhuravlev. The surface chemistry of amorphous silica. zhuravlev model. *Colloids and Surfaces A: Physicochemical and Engineering Aspects*, 173(1):1–38, 2000.

- [257] B Krishna Bharadwaj, Hareesh Chandrasekar, Digbijoy Nath, Rudra Pratap, and Srinivasan Raghavan. Intrinsic limits of channel transport hysteresis in graphene-sio₂ interface and its dependence on graphene defect density. *Journal of Physics D: Applied Physics*, 49(26):265301, may 2016.
- [258] Duhee Yoon, Hyerim Moon, Young-Woo Son, Jin Sik Choi, Bae Ho Park, Young Hun Cha, Young Dong Kim, and Hyeonsik Cheong. Interference effect on raman spectrum of graphene on sio₂/Si. *Phys. Rev. B*, 80:125422, Sep 2009.
- [259] Shaoming Huang, Mike Woodson, Richard Smalley, and Jie Liu. Growth mechanism of oriented long single walled carbon nanotubes using “fast-heating” chemical vapor deposition process. *Nano Letters*, 4(6):1025–1028, 2004.
- [260] D. Li, J. Zhang, Y. He, and et al. Scanning electron microscopy imaging of single-walled carbon nanotubes on substrates. *Nano Research*, 10:1804–1818, 2017.
- [261] J. Li, Y. He, Y. Han, K. Liu, J. Wang, Q. Li, S. Fan, and K. Jiang. Direct identification of metallic and semiconducting single-walled carbon nanotubes in scanning electron microscopy. *Nano Letters*, 12(8):4095–4101, 2012.
- [262] Y. He, J. Zhang, D. Li, J. Wang, Q. Wu, Y. Wei, L. Zhang, J. Wang, P. Liu, Q. Li, S. Fan, and K. Jiang. Evaluating bandgap distributions of carbon nanotubes via scanning electron microscopy imaging of the schottky barriers. *Nano Letters*, 13(11):5556–5562, 2013.
- [263] Dusan Vobornik, Maohui Chen, Shan Zou, and Gregory P. Lopinski. Measuring the diameter of single-wall carbon nanotubes using afm. *Nanomaterials*, 13(3), 2023.
- [264] J. Chen, X. Xu, L. Zhang, and et al. Controlling the diameter of single-walled carbon nanotubes by improving the dispersion of the uniform catalyst nanoparticles on substrate. *Nano-Micro Letters*, 7:353–359, 2015.
- [265] H. Kataura, Y. Kumazawa, Y. Maniwa, I. Umezu, S. Suzuki, Y. Ohtsuka, and Y. Achiba. Optical properties of single-wall carbon nanotubes. *Synthetic Metals*, 103(1):2555–2558, 1999. International Conference on Science and Technology of Synthetic Metals.
- [266] A Jorio, M A Pimenta, A G Souza Filho, R Saito, G Dresselhaus, and M S Dresselhaus. Characterizing carbon nanotube samples with resonance raman scattering. *New Journal of Physics*, 5(1):139, oct 2003.
- [267] F. Villalpando-Paez, H. Son, D. Nezich, Y. P. Hsieh, J. Kong, Y. A. Kim, D. Shimamoto, H. Muramatsu, T. Hayashi, M. Endo, M. Terrones, and M. S. Dresselhaus. Raman spectroscopy study of isolated double-walled carbon nanotubes with different metallic and semiconducting configurations. *Nano Letters*, 8(11):3879–3886, 2008. PMID: 18937518.
- [268] Xiaolin Li, Xiaomin Tu, Sasa Zaric, Kevin Welsher, Won Seok Seo, Wei Zhao, and Hongjie Dai. Selective synthesis combined with chemical separation of single-walled carbon nanotubes for chirality selection. *Journal of the American Chemical Society*, 129(51):15770–15771, 2007. PMID: 18052285.

- [269] Theerapol Thurakitserree, Erik Einarsson, Rong Xiang, Pei Zhao, Shinya Aikawa, Shohei Chiashi, Junichiro Shiomi, and Shigeo Maruyama. Diameter controlled chemical vapor deposition synthesis of single-walled carbon nanotubes. *Journal of Nanoscience and Nanotechnology*, 12(1):370–376, 2012.

Bien que l'eau soit un des éléments les plus répandus à la surface de la terre et directement impliqué dans un grand nombre de phénomènes, qu'ils soient naturels ou artificiels; et bien que sa molécule ne soit constituée que de 3 atomes, elle recèle encore de nombreux mystères. Toutes ses propriétés physiques et chimiques ne sont pas encore bien comprises, notamment lorsqu'elle se trouve confinée dans des espaces nanométriques. Elle fait donc toujours l'objet d'études fondamentales approfondies. Cependant, les nombreuses difficultés techniques rencontrées lorsque l'on veut travailler à l'échelle nanométrique font qu'aujourd'hui, l'essentiel des études publiées sont théoriques et non expérimentales. Il est donc indispensable de recueillir des données expérimentales sur ce sujet, en étudiant tout particulièrement des systèmes constitués d'un objet nanométrique unique.

C'est dans ce contexte très général que s'inscrivent les recherches expérimentales rapportées dans cette thèse. Les travaux menés sont séparés en deux parties distinctes mais qui visent à apporter, de façons différentes, leur contribution à l'étude de l'eau en milieu confiné. La première partie consiste en la mise au point d'un protocole expérimental destiné à fabriquer des microsystèmes étanches à l'eau liquide, à la vapeur d'eau et au vide. La fabrication de ces microsystèmes repose sur les techniques de micro photolithographie et sur l'utilisation de la résine SU-8. Nous montrons qu'il est possible de réaliser des microsystèmes imperméables à l'eau et étanches au vide dont les parois de SU-8 ne sont pas plus épaisses que 35 μm . Le protocole proposé s'avère donc tout à fait adapté à la réalisation de Lab-on-Chip/microplateformes de nanofluidique dédiées à l'étude de l'eau confinée et circulant dans un nanopore.

La deuxième partie rapporte toute une étude sur l'impact de l'eau sur le comportement électrique de μ -transistors à effet de champ dont le canal est constitué d'un unique nanotube de carbone (CNTFET). La réalisation de cette étude a nécessité de concevoir puis fabriquer par des techniques relevant de la microélectronique un μ -dispositif constitué de plusieurs microélectrodes au contact d'un seul nanotube; ces électrodes permettant soit d'effectuer des mesures électriques, soit par effet joule d'ouvrir le nanotube à des endroits bien précis, ou encore de le porter à des températures suffisamment élevées pour éliminer toute trace d'eau de son environnement. La réponse électrique du CNTFET en fonction de l'environnement autour du nanotube, i.e. eau liquide, air ambiant, vide, est analysée. Une comparaison est faite entre les réponses obtenues lorsque le nanotube est fermé ou ouvert. Il est ainsi possible de proposer un modèle qualitatif simplifié d'interaction avec l'eau et de distinguer l'impact créé par l'eau adsorbée à l'extérieur du tube de celui associé à l'eau confinée dans le tube. Ce travail pionnier ouvre de nombreuses perspectives dans les domaines de la nanofluidique de l'eau et des études fondamentales sur sa structure et la dynamique de ses molécules en milieu confiné. En tout premier lieu, il servira au développement d'une μ -plateforme de mesures fondées sur les caractéristiques électromécaniques d'un nanotube de carbone unique en présence d'eau solide, liquide ou vapeur.

Although water is one of the most widespread material on the earth's surface and the most directly involved in a large number of phenomena, both natural and man-made; and although its molecule is made up of just 3 atoms, it still conceals many mysteries. Not all its physical and chemical properties are yet fully understood, especially when it is confined to nanometric spaces. It is therefore still the subject of in-depth fundamental studies. However, the many technical difficulties encountered when working at the nanometric scale mean that today, most published studies are theoretical rather than experimental. The need to collect experimental data is therefore essential, particularly from systems constituted of individual nano-objects. This is the general framework for the experimental research reported in this thesis. The work carried out can be divided into two distinct parts, each of which aims to contribute to the current and future experimental studies which will be carried out on water confined in a single nanopore.

The first part of the project involves the development of an experimental protocol for fabricating micro-platforms that are impervious to liquid water, water vapor and vacuum. The fabrication of these microsystems is based on micro photolithography techniques and the use of SU-8 resin. We show that it is possible to produce waterproof and vacuum-tight microsystems with SU-8 walls no thicker than 35 μm . The proposed protocol is therefore perfectly suited to the realization of Lab-on-Chip/nanofluidic micro-platforms dedicated to the study of water confined in a nanopore and to water nanofluidic.

The second part reports on a study of the impact of water on the electron transport of μ -field-effect transistors made of an individual single-walled carbon nanotube (SWCNT-FET). Microelectronics techniques to design and manufacture a μ -platform consisting of several microelectrodes in contact with a single nanotube are used. These electrodes made it possible either to carry out electrical measurements or to use the Joule effect to open the nanotube at specific points and also to heat it to temperatures high enough to eliminate all traces of water from its environment. The electron transport response of the SWCNT-FET as a function of the environment around the nanotube, i.e. liquid water, ambient air, and vacuum is analyzed. A comparison is made between the responses obtained when the nanotube is closed or open. It is thus possible to propose a simplified qualitative model of interaction with water and to distinguish the impact created by water adsorbed outside the tube from that associated with water confined within the tube. This pioneering work opens up many new prospects on water in the fields of nanofluidic and fundamental studies about its structure and the dynamics of its molecules in a confined environment. First and foremost, it will be used to develop a μ -measurement platform based on the electromechanical characteristics of a single carbon nanotube in the presence of water either solid, liquid or vapour.